

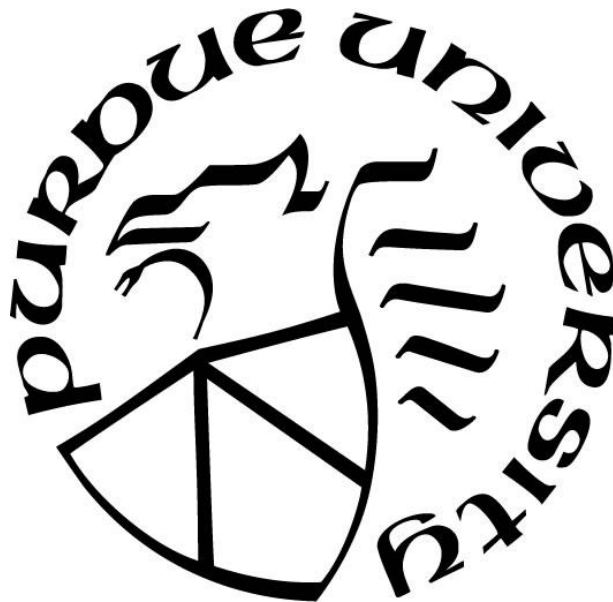
**MODELING AND STABILITY ANALYSIS OF A SERIES SINGLE-PHASE  
POWER ELECTRONIC BASED POWER SYSTEM**

by  
**Yimajian Yan**

**A Dissertation**

*Submitted to the Faculty of Purdue University  
In Partial Fulfillment of the Requirements for the degree of*

**Doctor of Philosophy**



School of Electrical & Computer Engineering

West Lafayette, Indiana

December 2018

**THE PURDUE UNIVERSITY GRADUATE SCHOOL**  
**STATEMENT OF COMMITTEE APPROVAL**

Dr. Scott D. Sudhoff, Chair

Department of Electrical and Computer Engineering

Dr. Jianghai Hu

Department of Electrical and Computer Engineering

Dr. Oleg Wasynczuk

Department of Electrical and Computer Engineering

Dr. Steven D. Pekarek

Department of Electrical and Computer Engineering

**Approved by:**

Pedro Irazoqui

Head of the Graduate Program

*To my wife, Tianqiong Luo and all the brilliant minds I met in West Lafayette and the Bay area. I  
love you.*

## ACKNOWLEDGMENTS

I wish to thank a few key people who made it possible to present this dissertation. First, I thank Dr. Scott. D. Sudhoff, for his patience, caution, and professional spirit. Second, I thank Dr. Jianghai Hu, who discovered my interest in electrical machinery and power systems. I also thank Dr. Oleg Wasynczuk and Dr. Steven D. Pekarek for their brilliant teach and research.

I also want to thank Tianqiong Luo, who is always my strongest mental support.

I also want to thank Di Shi, who is my manager in GEIRINA and an excellent leader for my research in smart grid.

I also want to thank Jingnan Pan and Hanfeng Wang, who are my managers in Google and opened a new world of signal and power integrity to me.

The research in fixture-centric airport runway/taxiway lighting system is sponsored by Federal Aviation Administration (FAA).

## TABLE OF CONTENTS

LIST OF TABLES .....	7
LIST OF FIGURES .....	8
ABSTRACT .....	11
1. INTRODUCTION .....	12
2. SYSTEM DESCRIPTION AND WAVEFORM-LEVEL MODEL .....	16
2.1 Current Source .....	16
2.1.1 Hysteresis modulation of single-phase AC current source .....	17
2.1.2 Current control .....	17
2.1.3 State-space model .....	20
2.1.4 Source-only simulation .....	21
2.2 Load Fixture .....	24
2.2.1 Fixture design motivation and principle .....	25
2.2.2 Fixture control .....	26
2.2.3 Transformer model .....	28
2.2.4 LED and PWM driver model .....	31
2.2.5 Fixture-only simulation .....	33
2.3 System Model and Simulation .....	38
3. AVERAGE-VALUE <i>QD</i> MODEL .....	44
3.1 Reference Frame Transformation .....	44
3.1.1 Introduction .....	44
3.1.2 System transformation .....	46
3.2 Average-Value <i>Qd</i> Modeling Of Linear System Components (Source) .....	48
3.2.1 Average-value modeling .....	48
3.2.2 Source average-value <i>qd</i> model and simulation .....	49
3.3 Average-Value <i>Qd</i> Modeling Of Nonlinear System Components (Load) .....	56
3.3.1 Approximation for fast-switching and rectifiers .....	56
3.3.2 Fixture average-value state-space model .....	59
3.3.3 Fixture-only simulation .....	61
3.4 System Average-value Simulation .....	64

4. STABILITY ANALYSIS .....	67
4.1 Reference Frame Transformation .....	67
4.2 Generalized Nyquist Criterion and Its Application .....	69
4.2.1 Introduction.....	69
4.2.2 Implementation of the generalized Nyquist criterion .....	70
4.3 Stability Analysis Using The Average-Value $Qd$ Models .....	72
5. IMPEDANCE MEASUREMENT.....	83
5.1 Principles of Impedance/Admittance Measurement .....	83
5.1.1 Definition of small-signal injection and response .....	83
5.1.2 Injection assignment .....	85
5.1.3 Phasor extraction from time-domain waveform .....	87
5.1.4 Time-domain considerations .....	88
5.1.5 Single-phase $qd$ impedance measurement algorithm .....	91
5.2 Numerical Validation Study .....	95
5.3 Hardware Validation.....	98
5.3.1 Model modification .....	98
5.3.2 Experiment results .....	102
6. SUMMARY AND FUTURE WORK .....	107
APPENDIX A. LED FIXTURE DESIGN EXAMPLE.....	108
APPENDIX B. INDUCTOR AND TRANSFORMER CHARACTERIZATION.....	111
REFERENCES .....	118
VITA.....	123

## LIST OF TABLES

Table 2.1	Parameter list of the source.....	22
Table 2.2	Fixture parameters .....	35
Table 2.3	Case 1 system parameters .....	40
Table 2.4	Case 2 system parameter modification .....	41
Table 5.1	$Qd$ impedance measurement procedure .....	95
Table 5.2	Fixture parameters .....	104
Table 5.3	Impedance value by three methods.....	106

## LIST OF FIGURES

Figure 1.1 Vault-centric system with CCR and incandescent lights .....	13
Figure 1.2 (a) Vault-centric (b) Fixture-centric architecture .....	13
Figure 2.1 Topology of constant AC current source.....	18
Figure 2.2 Hysteresis state transition diagram.....	18
Figure 2.3 Current waveform from hysteresis modulation.....	18
Figure 2.4 Current control.....	19
Figure 2.5 Source simulation .....	21
Figure 2.6 Source-only simulation waveforms.....	23
Figure 2.7 Load fixture structure [31].....	24
Figure 2.8 Fixture topology .....	25
Figure 2.9 Sine-triangle modulator.....	26
Figure 2.10 Fixture control .....	27
Figure 2.11 $\lambda - i$ curves of isolation transformer .....	30
Figure 2.12 LED I-V curve.....	31
Figure 2.13 LED duty cycle control and PWM driver.....	32
Figure 2.14 Fixture-only simulation diagram .....	33
Figure 2.15 Fixture steady-state waveforms.....	36
Figure 2.16 Fixture step-change waveforms.....	37
Figure 2.17 Transmission line model simplification .....	39
Figure 2.18 Case 1 system waveform-level model simulation result .....	42
Figure 2.19 Case 2 system waveform-level model simulation result .....	43
Figure 3.1 Current source topology .....	49
Figure 3.2 Current source control .....	50
Figure 3.3 Source average-value $qd$ waveforms.....	54
Figure 3.4 Source waveforms comparison.....	55
Figure 3.5 Load fixture topology (repeated from Figure 2.8).....	56
Figure 3.6 Load fixture control (repeated from Figure 2.10) .....	56
Figure 3.7 Fixture AVQDM waveforms.....	62
Figure 3.8 Fixture waveforms comparison .....	63

Figure 3.9 Case 1 System simulation result comparison .....	65
Figure 3.10 Case 2 System simulation result comparison .....	66
Figure 4.1 Equivalent circuit of dc system .....	68
Figure 4.2 MIMO system.....	69
Figure 4.3 Lumped system circuit .....	70
Figure 4.4 MIMO equivalent system of the single-phase ac system .....	71
Figure 4.5 Modified system model for stability analysis.....	72
Figure 4.6 Nyquist plots of Case 1.....	77
Figure 4.7 Nyquist plots of Case 2.....	78
Figure 4.8 Barely unstable situation .....	79
Figure 4.9 Barely stable situation .....	80
Figure 4.10 Nyquist plot of Case 2, $N_f = 1$ .....	81
Figure 4.11 Time-domain waveforms for 38, 39, 40, and 41 load numbers .....	82
Figure 5.1 Load Fixture topology .....	89
Figure 5.2 Load waveforms with $\omega_i = 2\pi \cdot 40$ Hz, first set (5.14).....	90
Figure 5.3 Load waveforms with $\omega_i = 2\pi \cdot 40$ Hz, second set (5.18). .....	91
Figure 5.4 Comparison between impedance measurement and modeling.....	96
Figure 5.5 Comparison between admittance measurement and modeling .....	97
Figure 5.6 Nyquist plot comparison.....	98
Figure 5.7 Modified fixture topology .....	99
Figure 5.8 Modified control diagram.....	99
Figure 5.9 Experiment environment .....	103
Figure 5.10 Hardware experimental result.....	105
Figure A.1 Circuit overview .....	109
Figure A.2 Op-amp based PI control (with filter).....	110
Figure B.1 Four-wire measurement for DC resistance .....	112
Figure B.2 AC measurement for flux linkage.....	113
Figure B.3 $\lambda - i$ curves of 1.0 mH inductor .....	113
Figure B.4 Transformer characterization .....	114
Figure B.5 $\lambda - i$ curves of transformer.....	115
Figure B.6 Transformer $\lambda - i$ curves modeling.....	116

Figure B.7 Leakage inductance measurement .....	117
Figure B.8 Leakage characterization .....	117

## ABSTRACT

Author: Yan, Yimajian. PhD

Institution: Purdue University

Degree Received: December 2018

Title: Modeling And Stability Analysis Of A Series Single-Phase Power Electronic Based Power System

Committee Chair: Scott D. Sudhoff

Tightly regulated power converters behave as constant power loads which may introduce instability in power systems. Prior to this work, the design-oriented stability criteria of DC and three-phase AC systems has been extensively studied, while the stability of single-phase AC power systems has received less attention. In this research, the modeling and stability analysis of single-phase AC power systems is studied. In particular, this research focuses on a system architecture where loads are connected in series and powered by a current source. Based on the proposed current source and load power electronic based topologies, which are typically used in airfield lighting systems, three types of system characterization are developed: waveform-level model, average-value  $qd$  model, and  $qd$  impedance/admittance measurement. Each approach has its own advantages and drawbacks, but the result - a frequency-domain ( $s$ -domain) representation of the system, is identical. Applying the generalized Nyquist stability criterion, the small-signal stability criteria of the system is developed. It is shown that the predictions of the system stability using these three approaches are consistent.

## 1. INTRODUCTION

Recently, the designers of airfield lighting systems began considering LEDs (light emitting diodes) as an alternative to incandescent lights. LEDs are much more efficient than traditional lighting devices, and are increasingly used in various situations. However, in order to meet aviation requirements, LED based lighting fixtures must be carefully designed. In particular, because the LED output wavelength is dependent on LED current [1], a precise current controller is required. Furthermore, in most applications, the LED brightness is adjusted by changing the duty cycle of a PWM current source, so that the current flowing through the LED is switching between zero and a tightly controlled value.

In the past, airfield lighting systems used a vault-centric architecture, where the series connected lighting fixtures were powered and controlled by a current source located in a lighting vault. Typically, a lighting vault is a building with all the lighting power system control equipment which is located near the runways. The lighting fixtures, which consist of isolation transformers and incandescent lights, are distributed on the airport runway and connected in series. All fixtures are simultaneously controlled by a current source known as a CCR (constant current regulator). Figure 1.1 illustrates a vault-centric architecture realized using thyristor control. The brightness of the incandescent lights is adjusted by controlling the conducting angle of the thyristor. Other types of CCR vault-centric systems can be realized by a matrix downconverter [2] or a ferroresonant CCR [3, 4]. Typically, the current transmitted to load lighting fixtures is 60 or 50 Hz, 0 to 6.6A rms, and sinusoidal. Each fixture has a circuit breaker on the secondary winding of the isolation transformer (which is not shown in Figure 1.1). If a fault occurs in the fixture (for example, a burnt lamp), the circuit breaker shorts the secondary winding, so that the rest of the system is not impacted. Alternately, the isolation transformers may be saturated to provide a protection against such faults.

Figure 1.2 (a) illustrates a vault-centric architecture using LEDs instead of incandescent lights. The LED PWM driver (the shaded triangle) is located in the equipment vault and works as a current source; every fixture has a passive full-bridge rectifier. The current waveform produced by the current source and transmitted to the fixture isolation transformers is ideally a square-wave. However, in practice given the transmission line inductance (in Figure 1.2 as the leakage inductance of the transformers), capacitance (shown as the wire-to-ground capacitances in Figure

1.2), and parasitic paths, achieving a high fidelity square wave current is highly problematic. The resulting waveform distortion is acceptable when the pulse width is high (over 25%); however, when the supply pulse width drops to below 2.5%, or even 0.15% (which are standard brightness level steps), the current waveform received by LEDs is far from the desired one, resulting in color distortion.

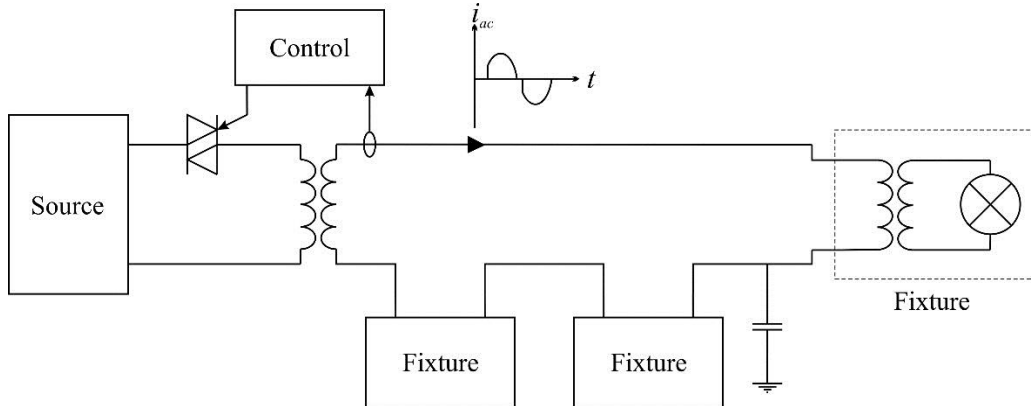


Figure 1.1 Vault-centric system with CCR and incandescent lights

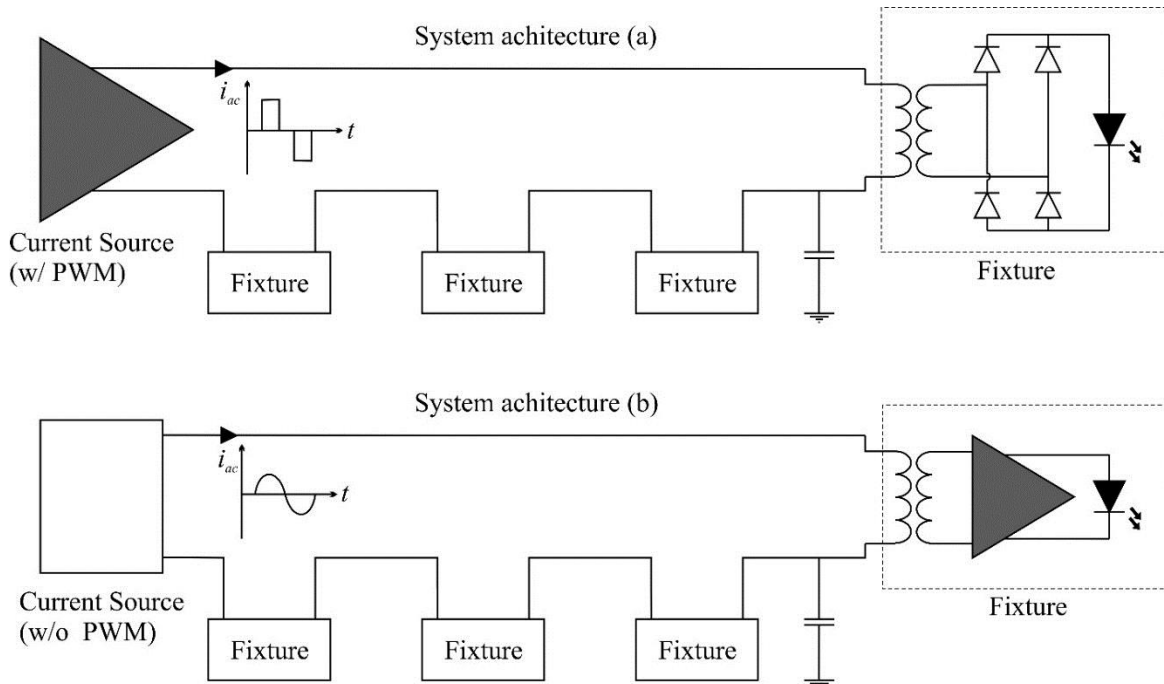


Figure 1.2 (a) Vault-centric (b) Fixture-centric architecture

In order to solve this problem without modification of existing circuit structure and cables, a fixture-centric architecture has been proposed. In the fixture-centric architecture shown in Figure 1.2 (b), each LED fixture has a PWM driver and modulate its LED's square wave current individually. The current source is similar to the AC current source in Figure 1.1, and the transmitted current is ideally sinusoidal. In practice, the transmitted current will not be highly distorted.

Although the fixture-based architecture facilitates brightness control, the existence of multiple control loops makes the system more susceptible to stability problems. The LED fixture including power-electronic based semi-autonomous converter constitute a constant power load [5-10]. Failures such as overheating and component breakdown will occur if the system is unstable.

Previously, the stability of dc systems has been extensively studied in various situations: DC-DC converters [11-16], DC transmission [17, 18] and DC micro-grids and distribution systems [19]. Research involving three-phase AC system stability includes: Lyapunov-based control [20], small-signal stability [21-23], distributed control [24], and stability region analysis [25-29]. However, single-phase AC system analysis has received less attention. The aim of this research is to study the principle and application of single-phase AC system stability using the fixture-centric airport lighting system as an example. In three-phase AC system stability analysis, a  $qd$  transformation can be applied to three-phase ac quantities to obtain dc  $qdo$  quantities, whose stability can be analyzed using Nyquist theory. Herein, this methodology will be applied to single-phase AC systems.

This dissertation is organized as follows. Chapter 1 introduced the basic architecture of the airport runway lighting system and the motivation of performance evaluation and stability analysis for the same. In Chapter 2, the fixture-centric system is analyzed in detail, and the waveform-level models of system components are established. By combining one source model and a number of load fixture models, the system model predicts transient performance of brightness level steps. In Chapter 3, the signal-phase  $qd$  transformation and the average-value modeling method are introduced; accordingly, the system is described by an average-value  $qd$  model (AVQDM), where both the single-phase AC variables (currents, voltages and flux linkages) and DC variables appear as constants under steady-state conditions. In Chapter 4, work on DC system stability is reviewed to illustrate power system stability criteria. The generalized Nyquist Theorem is applied on the linearized AVQDM of the system components. Thus, the system stability criteria is derived.

Finally, the stability analysis based on system component characterization through impedance/admittance measurement is considered. This is set forth in Chapter 5.

## 2. SYSTEM DESCRIPTION AND WAVEFORM-LEVEL MODEL

In time-domain analysis of power systems, two major approaches are widely used: waveform-level modeling (WLM) and average-value modeling (AVM). Waveform-level modeling is a detailed representation of every system component, and it includes representation of the switching of the power electronic devices. Therefore, it is accurate but computationally intensive. Average-value modeling is a simplified representation of power systems that only captures the primary dynamics in a moving-average sense. Therefore, the AVM is computationally less intensive than the WLM. Furthermore, the AVM can be linearized about an operating point to yield a linear time-irrelevant (LTI) multiple-input-multiple-output (MIMO) system model for stability analysis, which will be discussed in Chapter 4. In both modeling methods, the system time-domain behavior can be expressed as

$$p\mathbf{x} = f(\mathbf{x}, \mathbf{u}) \quad (2.1)$$

$$\mathbf{y} = g(\mathbf{x}, \mathbf{u}) \quad (2.2)$$

where  $p\mathbf{x}$  is the time derivative of the state vector  $\mathbf{x}$ . The state vector  $\mathbf{x}$  contains the least number of variables that can determine the status of the entire circuit (currents, voltages, and flux linkages). The symbols  $\mathbf{u}$  and  $\mathbf{y}$  represent the input and output vector, respectively.

In this chapter, a system consisting of a current source and load fixtures is set forth for a notional series AC single-phase power system utilized in airfield lighting. In addition to the system description, the WLM is formulated by finding the system variable dynamics in the form of (2.1) and their relationship with output variables in the form of (2.2).

### 2.1 Current Source

The current source is designed to supply a constant amplitude and constant frequency sinusoidal current to an uncertain load. It is assumed that the current source is supplied from an ideal DC voltage source. As shown in Figure 2.1, in the notional system, the current source consists of an H-bridge AC-DC inverter, a transformer, and an output filter (consisting of the transformer secondary leakage inductance and an output capacitor). The inverter is controlled using hysteresis modulation so that the transformer primary current  $i_p$  tracks the desired primary current  $i_p^*$ . The

desired primary current  $i_p^*$  is obtained from the feedback control as shown in Figure 2.2. The hysteresis modulation and the current control will be described in Subsection 2.1.1 and 2.1.2, respectively. The state space model of the source including the transformer and output filter is set forth in Subsection 2.1.3. For illustration, a load step-change simulation is carried out in Subsection 2.1.4.

### 2.1.1 Hysteresis modulation of single-phase AC current source

Hysteresis modulation is a commonly used current control strategy, and is described in detail in Section 12.8 of [30]. The current is regulated by controlling the four switches  $s_1$  to  $s_4$  as shown in Figure 2.1: when  $s_1$  and  $s_4$  are ‘on’,  $s_2$  and  $s_3$  are ‘off’, the primary voltage across the transformer  $v_p$  is equal to  $v_{dc}$ , and  $i_p$  will increase; when  $s_1$  and  $s_4$  are ‘off’,  $s_2$  and  $s_3$  are ‘on’, the primary voltage across the transformer  $v_p$  is equal to  $-v_{dc}$ , and  $i_p$  will decrease.

The principle of hysteresis modulation applied in this current source as shown in Figure 2.2 is to change the switch state to increase the primary current when it reaches the lower bound of an allowed region, and to decrease the current when it reaches the upper bound, so that the average value of  $i_p$  follows the desired waveform  $i_p^*$  as shown in Figure 2.3. The lower bound is the desired current minus the hysteresis level and the higher bound is the desired current plus the hysteresis level. Through the low-pass filter formed by the secondary leakage inductance of the transformer and the output capacitor  $C_{ac}$ , the output current  $i_{ac}$  will exclude the high-frequency components introduced by switch operations.

Although the hysteresis modulation can be used to control the primary current waveform, because of the transformer and the output filter, the waveform of  $i_{ac}$  will vary with the load characteristics. Herein, the current control is introduced to maintain the output current at the desired frequency and amplitude.

### 2.1.2 Current control

The proposed current control diagram is shown in Figure 2.4. It includes a proportional path with a low-pass filter, a path with a two-pole inverse notch filter, and a DC filter. The low-pass filter eliminates the high-frequency component of the transmission line current. The inverse notch filter is utilized to ensure that the desired fundamental component of the source output

current is exactly obtained. To illustrate the function of the inverse notch filter, assume that the relationship between the output current and the control output is given by

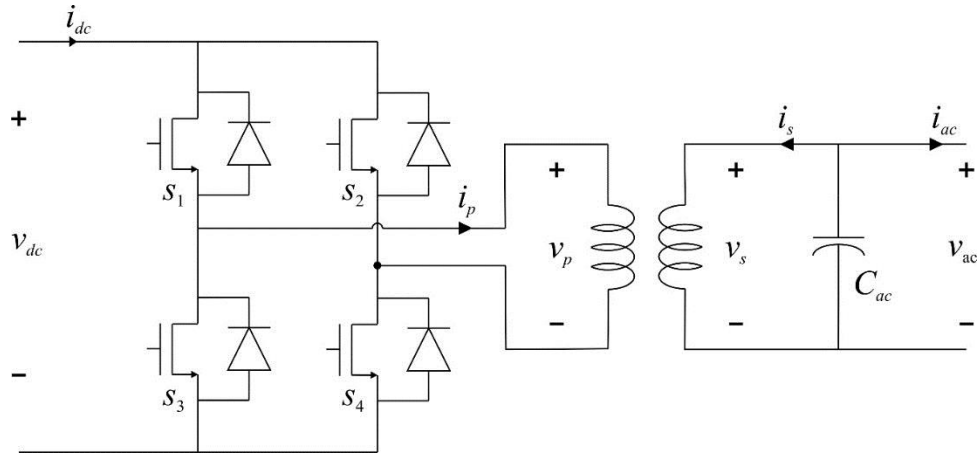


Figure 2.1 Topology of constant AC current source

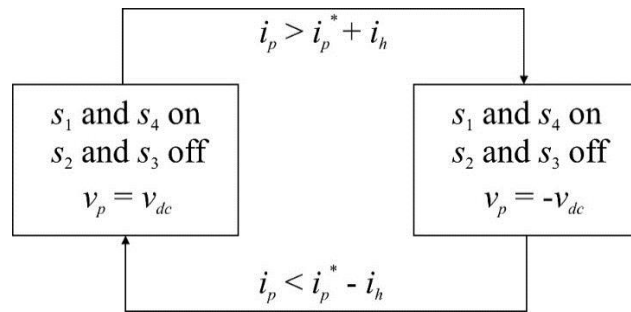


Figure 2.2 Hysteresis state transition diagram

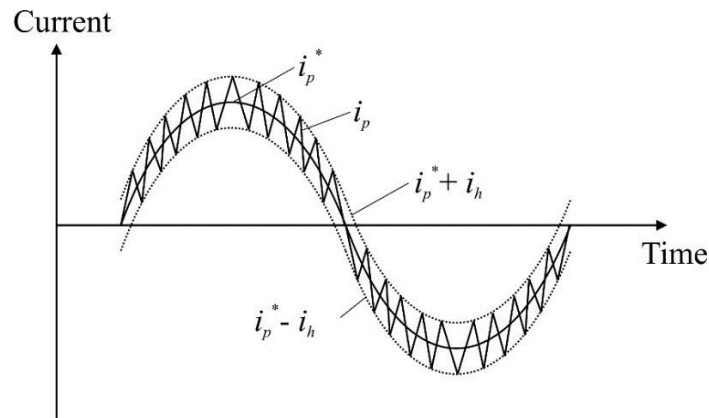


Figure 2.3 Current waveform from hysteresis modulation

$$i_{ac} = T(s) \frac{N_p}{N_s} i_p^* \quad (2.3)$$

where  $T(s)$  is a transfer function dependent upon the transformer, output filter and load characteristics. The DC filter has an extremely low cut-off frequency such that its impact at the fundamental frequency can be neglected. From (2.3) and Figure 2.4,

$$i_{ac} = T(s) \left( \frac{k_p}{\tau s + 1} + \frac{k_i \omega_e^2}{s^2 + \omega_e^2} \right) (i_{ac}^* - i_{ac}) \quad (2.4)$$

Solving (2.4) for  $i_{ac}$  yields

$$i_{ac} = \frac{k_p T(s)(s^2 + \omega_e^2) + k_i \omega_e^2 T(s)(\tau s + 1)}{(\tau s + 1)(s^2 + \omega_e^2) + k_p T(s)(s^2 + \omega_e^2) + k_i \omega_e^2 T(s)(\tau s + 1)} i_{ac}^* \quad (2.5)$$

Since  $i_{ac}^*$  is an impulse function centered at  $s = \pm j\omega_e$ , which can be substituted to (2.5) yielding  $i_{ac} = i_{ac}^*$ . Therefore, the output current waveform will exactly follow the desired sinusoidal waveform in steady-state conditions.

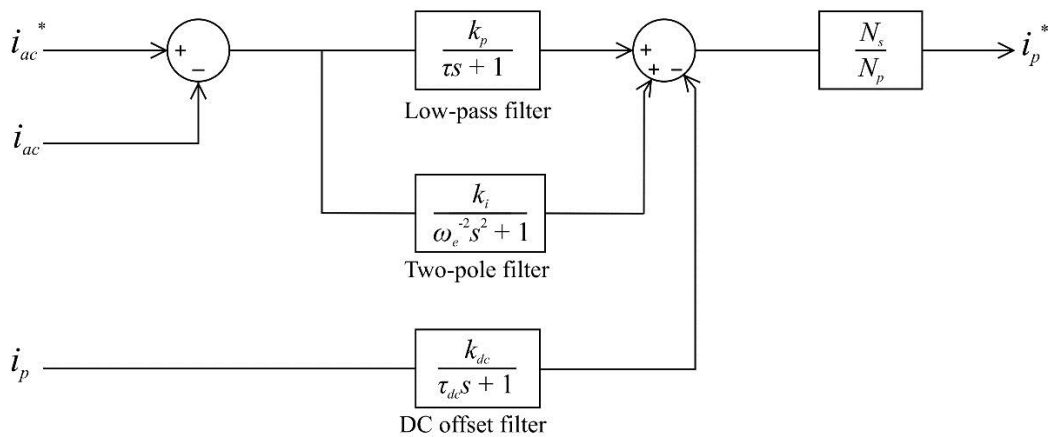


Figure 2.4 Current control

The DC filter shown in Figure 2.4 is designed to attenuate DC offsets in  $i_p$ . Because of the transformer, the DC component of  $i_p$  is not coupled to that of  $i_{ac}$ . Consequently, DC offsets in  $i_p$  do not decay quickly as desired, which increases the system loss. To solve this problem, the DC offset feedback based on low-pass filtering  $i_p$  is used.

### 2.1.3 State-space model

For the topology shown in Figure 2.1, the status of the subsystem consisted with the transformer and the output filter (the passives) can be determined by

$$\mathbf{x}_{sp} = \begin{bmatrix} i_p & i'_s & v_s \end{bmatrix}^T \quad (2.6)$$

which can be shown to be a minimal set of variables. The inputs of the state space model are  $v_p$  and  $i_{ac}$ , and the output of this model is  $v_{ac}$  (or  $v_s$  of the transformer). As described in Chapter 1 of [30], the referred secondary current is defined by

$$i'_s = \frac{N_s}{N_p} i_s \quad (2.7)$$

where  $N_p$  and  $N_s$  are the numbers of turns of the primary and secondary winding of the transformer, respectively. Meanwhile, the referred secondary voltage is defined by

$$v'_s = \frac{N_p}{N_s} v_s \quad (2.8)$$

For simplicity, it is assumed that the transformer is always operating at linear region. Thus, the relationship between the flux linkages and the currents can be expressed as a linear function

$$\begin{bmatrix} \lambda_p \\ \lambda'_s \end{bmatrix} = \begin{bmatrix} L_{lp} + L_m & L_m \\ L_m & L'_{ls} + L_m \end{bmatrix} \begin{bmatrix} i_p \\ i'_s \end{bmatrix} \quad (2.9)$$

where  $L_m$  is the magnetizing inductance,  $L_{lp}$  is the primary leakage inductance, and  $L'_{ls}$  is the referred secondary leakage inductance (the calculation of the referred values can be found in Chapter 1 of [30]). Taking the inverse of (2.9) yields

$$\begin{bmatrix} i_p \\ i'_s \end{bmatrix} = \frac{1}{(L'_{ls} + L_m)(L_{lp} + L_m) - L_m^2} \begin{bmatrix} L'_{ls} + L_m & -L_m \\ -L_m & L_{lp} + L_m \end{bmatrix} \begin{bmatrix} \lambda_p \\ \lambda'_s \end{bmatrix} \quad (2.10)$$

From Ohm's and Faraday's law, the dynamic of the flux linkages can be described by

$$p\lambda_p = v_p - r_p i_p \quad (2.11)$$

$$p\lambda'_s = v'_s - r'_s i'_s \quad (2.12)$$

Substituting (2.11) and (2.12) to (2.10) yields

$$pi_p = \frac{(L'_{ls} + L_m)(v_p - r_p i_p) - L_m(v'_s - r'_s i'_s)}{(L'_{ls} + L_m)(L_{lp} + L_m) - L_m^2} \quad (2.13)$$

$$p i_s' = \frac{(L_p + L_m)(v_s' - r_s' i_s') - L_m(v_p - r_p i_p)}{(L_s + L_m)(L_p + L_m) - L_m^2} \quad (2.14)$$

The dynamics of  $v_s$  is governed by

$$p v_s = \frac{1}{C_s} \left( -\frac{N_p}{N_s} i_s' - i_{ac} \right) \quad (2.15)$$

Thus, the time derivatives of the state variables  $i_p$ ,  $i_s'$ , and  $v_s$  are expressed using only the state variables, inputs, and the system parameters.

#### 2.1.4 Source-only simulation

Based on the source model subsystems described in previous subsections, the simulation can be visualized by the diagram in Figure 2.5. The source adjust its output voltage  $v_{ac}$  for varying load characteristics to maintain a constant sinusoidal output current  $i_{ac}$ .

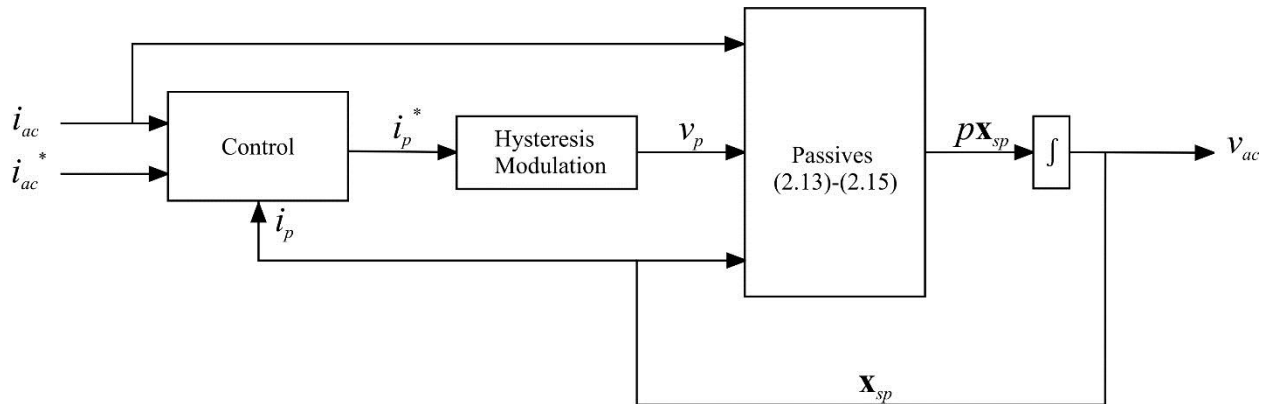


Figure 2.5 Source simulation

The load of this source-only simulation is assumed to be a series L-R circuit. The load inductance is 100 mH, which is a large but reasonable value considering a system with fifty series-connect load fixtures (referring to the proposed fixture schematic shown in 2.2.1). The load resistance steps from  $100\Omega$  to  $200\Omega$  at 0.5s, when the current is at its peak (as the worst case). The load model can be described by a single state variable  $i_{ac}$  using

$$p i_{ac} = \frac{1}{L_{load}} (v_{ac} - r_{load} i_{ac}) \quad (2.16)$$

with input  $v_{ac}$  and output  $i_{ac}$  as a state space model.

Combining the source model and the load model, and using the parameters in Table 2.1, the system performance for this step-change resistance can be simulated and evaluated. The solver used is ODE4 (Runge-Kutta), and the time step is 1  $\mu$ s. As shown in Figure 2.6, the output current becomes distorted at the step change of the load resistance, but recovers within 50 ms. The waveform of  $i_s$  is distorted due to the fast switching of the H-bridge, but with the output filter the waveform of  $i_{ac}$  is nearly ideal. The waveform of  $v_{ac}$  is leading  $i_{ac}$  by a small amount of angle due to the inductive load characteristic. The primary movement of  $i_p$  represent the control output  $i_p^*$ , which eliminates the distortion of  $i_{ac}$  feedback and has no DC offset.

Table 2.1 Parameter list of the source

Component	Value
Turns ratio ( $N_p/N_s$ )	0.8
Primary winding resistance ( $r_p$ )	0.02 $\Omega$
Secondary winding resistance ( $r_s$ )	0.04 $\Omega$
Magnetizing inductance ( $L_m$ )	0.12 H
Primary leakage inductance ( $L_{lp}$ )	0.1 mH
Secondary leakage inductance ( $L_{ls}$ )	0.6 mH
DC supply voltage ( $v_{dc}$ )	500 V
Output capacitance ( $C_{ac}$ )	5 $\mu$ F
Hysteresis level ( $i_h$ )	0.1 A
Output current rms amplitude ( $i_{ac}^*$ )	2 A
Output current frequency ( $\omega_e$ )	377 rad/s
Proportional gain ( $k_p$ )	0.5
Integrational gain ( $k_i$ )	0.8
Low-pass filter time constant $\tau$	1.6 ms
DC filter time constant $\tau_{dc}$	0.265 s
DC filter gain $k_{dc}$	1

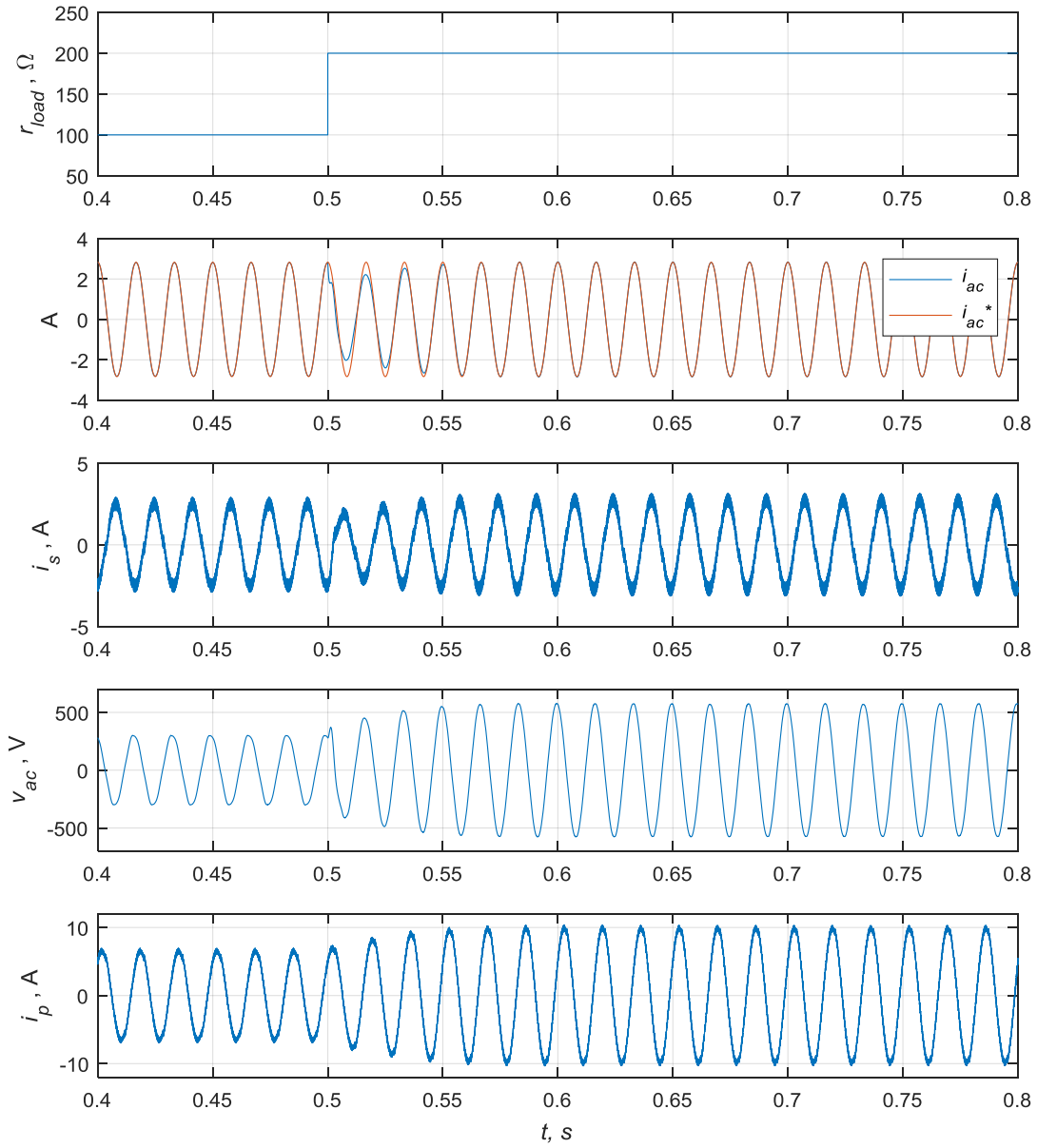


Figure 2.6 Source-only simulation waveforms

## 2.2 Load Fixture

A typical physical structure of a lighting fixture including the isolation transformer is shown in Figure 2.7. The fixture is embedded on the runway or taxiway. The isolation transformer and the transmission lines are buried in the ground. The isolation transformer has three cables: two single conductor ring cables are connected to its primary winding; the other cable has two conductors, which are connected to the secondary winding. The primary windings of all fixtures are connected to the transmission line in series. A fixture waveform-level model should include an isolation transformer model (with saturation), a regulated AC-DC converter, a LED with PWM driver, and input and output filters. In this section, first the design motivation and principle is introduced with a prototype topology in Subsection 2.2.1, with the control method set forth in Subsection 2.2.2. The transformer model is described in Subsection 2.2.3, and the LED and its PWM driver model is described in Subsection 2.2.4. A stand-alone fixture simulation is demonstrated in Subsection 2.2.5.

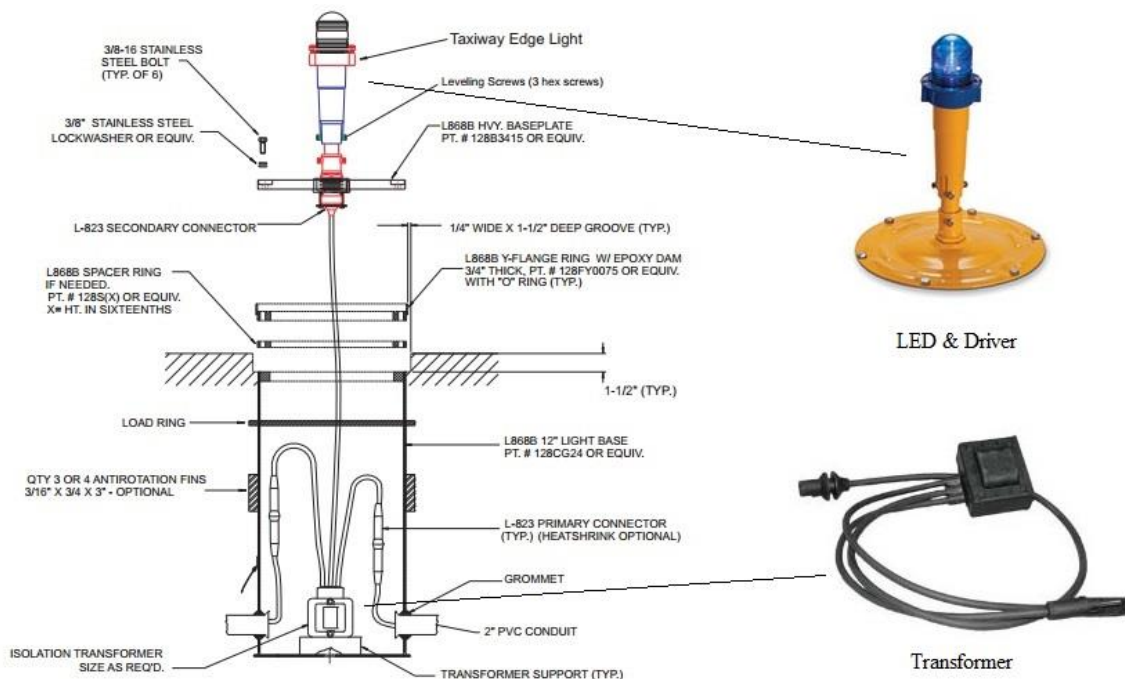


Figure 2.7 Load fixture structure [31]

### 2.2.1 Fixture design motivation and principle

The primary design motivation of the fixture-centric architecture lighting fixture is to control the LED light density by the pulse-width of a square-wave current. The input to the fixture can be assumed a constant sinusoidal current source. To this end, the use of power electronic based regulated rectifier and PWM driver are desired.

As shown in Figure 2.8, the PWM driver is realized with a switch parallel-connected to the LED: when this switch is turned on, the voltage drop across the switch becomes very small, thus the LED is turned off; when the switch is turned off, the current flowing through the switch is zero, and so that  $i_{ld} = i_{LLd}$ , and the LED is turned on. Therefore, the duty cycle of the LED is the logical compliment of the switch duty cycle  $d_s$ . By regulating  $i_{LLd}$  to be a constant, a square-wave LED current can be achieved.

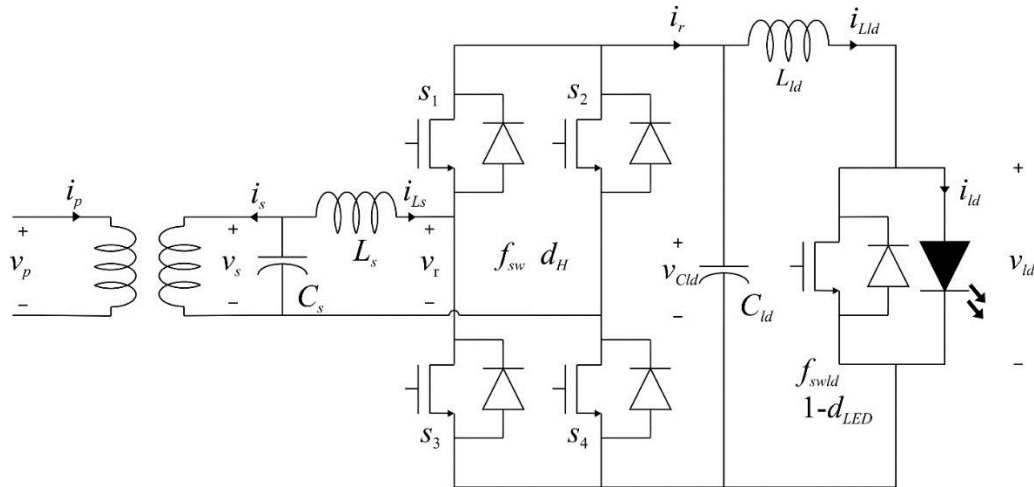


Figure 2.8 Fixture topology

As shown in Figure 2.9, the H-bridge serves as a regulated rectifier to convert the sinusoidal current  $i_{Ls}$  from the input to a DC current  $i_r$  to the output. The H-bridge operation involves two status:

1. Switches  $s_1$  and  $s_4$  are on,  $s_2$  and  $s_3$  are off, so that  $i_r = i_{Ls}$ , and  $v_r = v_{Cld}$ .
2. Switches  $s_2$  and  $s_3$  are on,  $s_1$  and  $s_4$  are off, so that  $i_r = -i_{Ls}$ , and  $v_r = -v_{Cld}$ .

The duty cycle of the H-bridge  $d_H$  represents the percentage of the time when the H-bridge is on status 1 minus the percentage of the time of status 2. Therefore, by controlling  $d_H$ , the output current of the H-bridge  $i_r$  can be regulated.

To generate the switching signal of the H-bridge to control its duty cycle, the sine-triangle

modulator shown in Figure 2.9 is utilized. Similar approaches using sine-triangle modulation can be found in [32-36]. The modulator produces a high-frequency triangular signal  $d_{ref}$ , whose amplitude is 1. This reference waveform is compared to the duty cycle: if  $d_H > d_{ref}$ , the H-bridge is operated in status 1; otherwise, the H-bridge is operated in status 2. Therefore, by configuring  $d_H$  a certain value between -1 and 1, the average-value of the rectified current  $i_r$  can be settled on a corresponding value between  $-i_{L_s}$  and  $i_{L_s}$ . The input filter consisted with  $L_s$  and  $C_s$  prevents the high-frequency switching signal produced by the H-bridge from entering the fixture input.

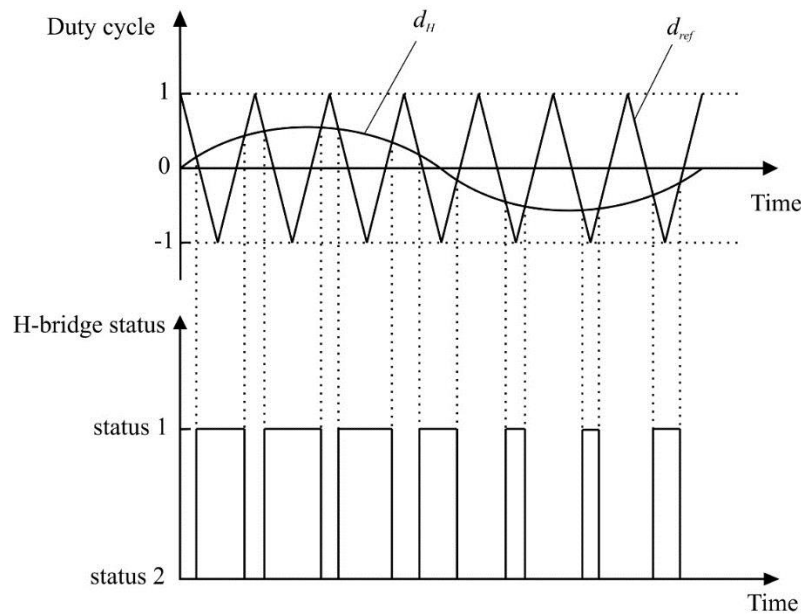


Figure 2.9 Sine-triangle modulator

### 2.2.2 Fixture control

As shown in Figure 2.10, the fixture control employs a PI feedback control and a multiplier. The PI control also includes a provision for anti-windup for back-calculation. In normal operation, the PI control output ( $y$ ) does not saturate so that the anti-windup has no impact. When the feedback signal  $i_{LLd}$  takes a large step, the overshoot of the response will be limited.

The purpose of the multiplier is to generate an H-bridge duty cycle  $d_H$  in-phase with the fundamental frequency component of  $i_{L_s}$ , while the amplitude of  $d_H$  is controlled by  $y$ . The term  $i_{L_s,base}$  is set to be the nominal amplitude of  $i_{L_s}$ . A low-pass filter is applied on  $i_{L_s}$  to eliminate high-

frequency components. To analyze the primary dynamics of the fixture with this control method, it is convenient to define a fast-average so that the impact of the switching of the power electronics may be viewed on a continuous sense. In particular,

$$\hat{f}(t) = \frac{1}{T_{sw}} \int_{t-T_{sw}}^t f(t) d\tau \quad (2.17)$$

where  $T_{sw}$  is the switching period of the power electronics. Using this definition, it can be shown that the steady-state H bridge duty cycle can be expressed as

$$d_H = \frac{y}{i_{Ls,base}} \hat{i}_{Ls} \quad (2.18)$$

and that the rectifier current  $i_r$  can be estimated as

$$\hat{i}_r = d_H i_{Ls} \quad (2.19)$$

Substituting (2.18) to (2.19), the approximate fast average of  $i_r$  can be expressed as

$$\hat{i}_r = \frac{y}{i_{Ls,base}} \hat{i}_{Ls}^2 \quad (2.20)$$

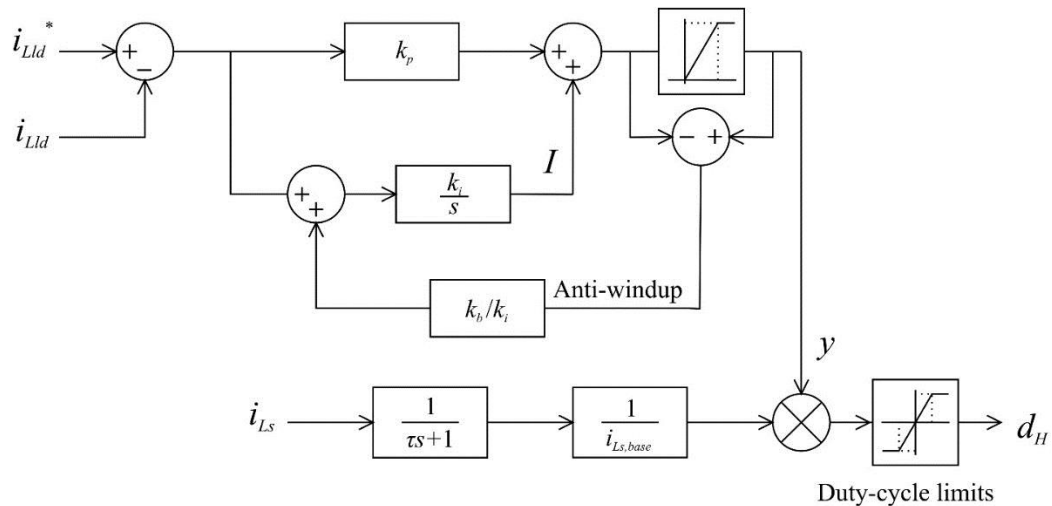


Figure 2.10 Fixture control

On the other hand, the rectified current can be approximated using a half-cycle average defined by

$$\bar{f}(t) = \frac{2}{T_e} \int_{t-T_e/2}^t f(t) d\tau \quad (2.21)$$

where  $T_e$  is the fundamental period of the input sinusoidal signal of the rectifier. Using this definition, and assuming that  $T_e$  is an even multiple of  $T_s$ , the load current  $i_{Lld}$  can be approximated as

$$\bar{i}_{Lld} = \bar{i}_r = \frac{2}{T_e} \int_{t-T_e/2}^t i_r(t) d\tau = \frac{2}{T_e} \int_{t-T_e/2}^t \hat{i}_r(t) d\tau \quad (2.22)$$

Assuming that in steady-state

$$\hat{i}_{Ls} = i_{Ls,base} \cos(\omega_e t + \phi) \quad (2.23)$$

where  $\omega_e = 2\pi/T_e$ ,  $\phi$  is a constant, it can be shown using (2.20) and (2.23) that

$$\bar{i}_{Lld} = \frac{1}{2} y i_{Ls,base} \quad (2.24)$$

Therefore, ideally the load current is a DC current (with a small ripple) proportional to the PI control output.

### 2.2.3 Transformer model

Unlike the source transformer, the saturation of the fixture transformer needs to be considered. This is because that transformer saturation is used to limit the voltage across a fixture when an open-circuit fault occurs inside the fixture. To this end, consider a core with a uniform cross-section area  $A$  and the magnetizing flux density of the cross-section  $B_m$ . When the magnetizing field density  $H_m$  increases,  $B_m$  might be expressed as

$$\lim_{H \rightarrow \infty} B_m = \mu_0 H_m + M_s \quad (2.25)$$

where  $M_s$  is the saturation flux density. Multiplying both sides of (2.25) by the cross-section area of yields

$$\lim_{H \rightarrow \infty} \Phi_m = \mu_0 H_m A + \Phi_s \quad (2.26)$$

where  $\Phi_s = M_s A$ . Suppose that two windings are coupled with this core: the primary winding has  $N_p$  number of turns, and the secondary winding has  $N_s$  number of turns. The positive currents through the two windings magnetize the core in the positive direction. Thus it can be shown that the total field density can be expressed by

$$\lim_{H \rightarrow \infty} \Phi_m = \frac{N_p i_p + N_s i_s}{R_{m0}} + \Phi_s \quad (2.27)$$

where  $R_{m0}$  is mutual leakage reluctance, which is dependent of the geometry as

$$R_{m0} = \frac{l_c}{\mu_0 A} \quad (2.28)$$

where  $l_c$  is the overall material length. If seen from the primary winding, a magnetizing current can be defined as  $i_m = i_p + \frac{N_s}{N_p} i_s$ . Herein, multiplying both left and right side of (2.27) by  $N_p$  yields

$$\lim_{H \rightarrow \infty} \lambda_m = \frac{N_p^2 i_m}{R_{m0}} + \lambda_s \quad (2.29)$$

This suggests that the magnetizing flux linkage can be expressed by

$$\lambda_m = f(i_m) + L_0 i_m \quad (2.30)$$

where  $L_0$  is the mutual leakage inductance,  $f(i_m)$  is a function that saturates at  $\lambda_s$ . A choice of  $f(i_m)$  is the arctangent function

$$f(i_m) = \alpha \cdot \arctan(\beta i_m) \quad (2.31)$$

The advantages of using this function include: (i) this function is differentiable and secondary differentiable, (ii) it is computationally inexpensive, (iii) it is convenient for linearization, and (iv) it has only three parameters  $\alpha$ ,  $\beta$  and  $L_0$  which are readily found from measurement. As shown in Figure 2.11, the approximation of the  $\lambda - i$  characterization using this function is accurate when the magnetizing flux linkage is small or close to saturation. The process of finding these parameters from characterizing a transformer product is attached as Appendix B. The major disadvantage of using this function is that hysteresis and core loss are not included. However, for this research, as the system loss analysis is not a primary objective, it is reasonable to use this function as an approximation.

Using this transformer  $\lambda - i$  magnetizing characteristic modeling, the state space model of transformer described in 2.1.3 can be modified to represent saturation. In addition, the input of the transformer is assumed to be an ideal current source, both  $i_p$  and  $p i_p$  can be set as input variables of the state space model. Therefore, the only state variable assumed with the transformer is  $i_m$ . To this end, start from the relationship between the magnetizing flux linkage and the secondary current as

$$p \lambda_m = v_s' - L_s' p i_s' - r_s' i_s' \quad (2.32)$$

Meanwhile, taking the time derivative of both sides of (2.30) yields

$$p\lambda_m = \left( \frac{\alpha\beta}{\beta^2 i_m^2 + 1} + L_0 \right) pi_m \quad (2.33)$$

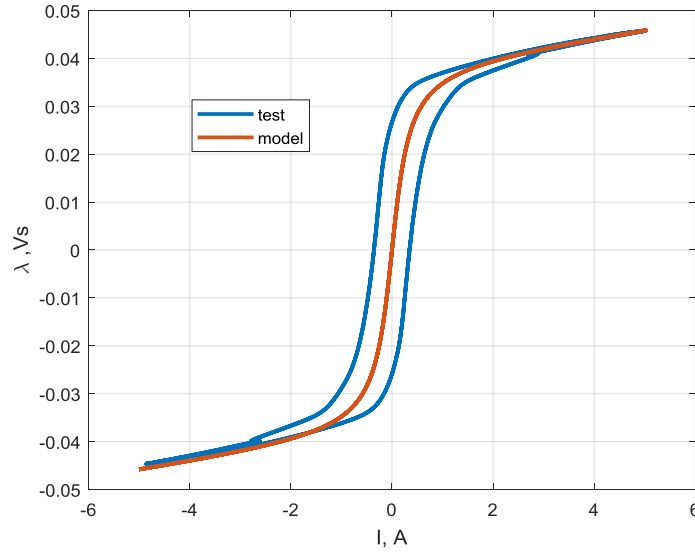


Figure 2.11  $\lambda - i$  curves of isolation transformer

Equating (2.32) and (2.33), and substituting  $i_s' = i_m - i_p$ , the time derivative of  $i_m$  can be expressed as

$$pi_m = \frac{\left[ v_s' + L_{ls}' pi_p - r_s' (i_m - i_p) \right]}{\frac{\alpha\beta}{\beta^2 i_m^2 + 1} + L_{ls}' + L_0} \quad (2.34)$$

At this point, the state space model of the transformer is established. The inputs of the model are  $i_p$  and  $pi_p$ ; its outputs are  $i_s$  and  $v_p$  which can be obtained by

$$i_s = \frac{N_p}{N_s} i_s' = \frac{N_p}{N_s} (i_m - i_p) \quad (2.35)$$

$$v_p = p\lambda_m + r_p i_p + L_{lp}' pi_p \quad (2.36)$$

In the system representation, the inputs of the transformer become  $v_p$  and  $v_s$ , and the outputs are  $i_p$  and  $i_s$ . Therein, the transformer model should be modified. This will be considered in Section 2.3.

### 2.2.4 LED and PWM driver model

From the diode physics, a LED  $I-V$  characteristic can be expressed as

$$i_{ld} = i_0 \left( e^{\frac{v_{ld}}{v_0}} - 1 \right) \quad (2.37)$$

or equivalently

$$v_{ld} = v_0 \ln \left( \frac{i_{ld}}{i_0} + 1 \right) \quad (2.38)$$

As a reference, a set of  $I-V$  measurements and the corresponding least square regression analysis is depicted in Figure 2.12. The regression finds the parameters  $v_0$  and  $i_0$  to minimize the square error of the current between each measurement data point and the ideal exponential function.

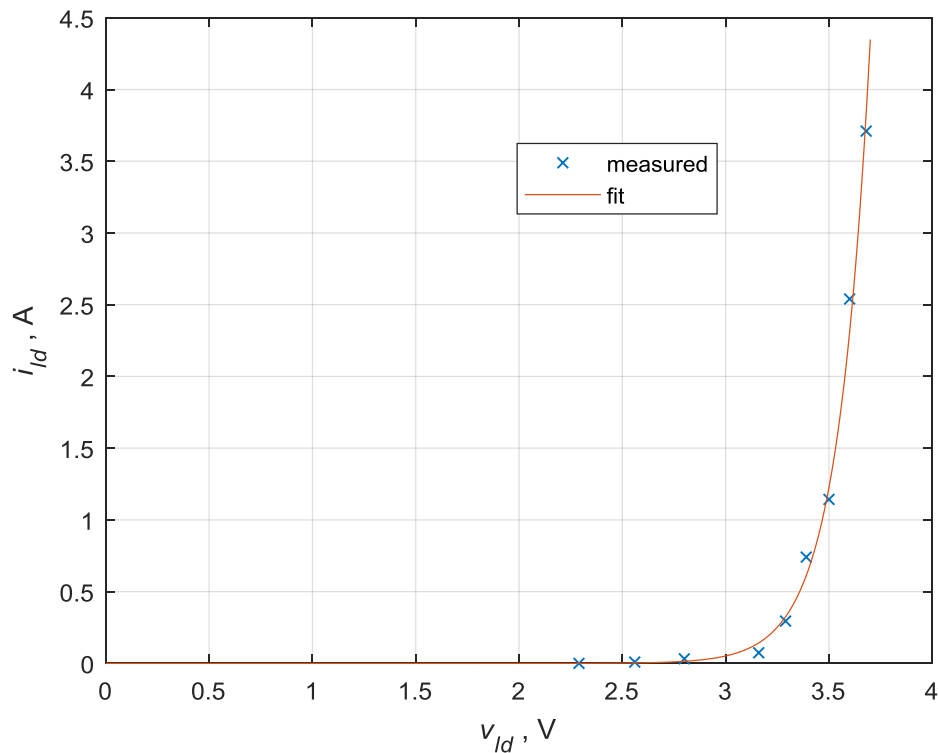


Figure 2.12 LED I-V curve

The PWM driver of the LED controls the light density by regulating the duty cycle of the parallel switch. In the situations where the commanded LED duty cycle decreases rapidly, the LED might be supplied with a load current much higher than the desired value, until the fixture control

responds. In this situation, LED overheating will occur. To prevent this, the slew-rate limited differential duty cycle control is applied as shown in Figure 2.13. The slew rate of the duty cycle is dependent on the difference between the commanded value and actual value, and its absolute value is restricted by the slew rate limit. Therefore, when a step change in the commanded LED duty cycle occurs, the actual duty cycle ‘smoothly’ increases or decreases to the commanded value.

The PWM driver of the switch in parallel with the LED is also shown in Figure 2.13 to illustrate the generation of a switching signal. In terms of modeling, the input of this component (including the LED, the parallel switch, and the associated controls) is  $i_{LLd}$  and  $d_{LED}^*$ , and its output is  $v_{ld}$  and  $i_{ld}$ . A reference signal  $d_{ref}$  is generated and compared with the LED duty cycle  $d_{led}$  to generate  $s$ . Assuming that the voltage drop on the switch is zero, the following strategy is used for the switch control and model output:

- (1) if  $d_{ref} \geq d_{LED}$ ,  $s = 1$  or  $i_{LLd} \leq 0$ , then  $i_{ld} = 0$ ,  $v_{ld} = 0$ .
- (2) Otherwise,  $i_{ld} = i_{LLd}$ ,  $v_{ld}$  is obtained from (2.38)

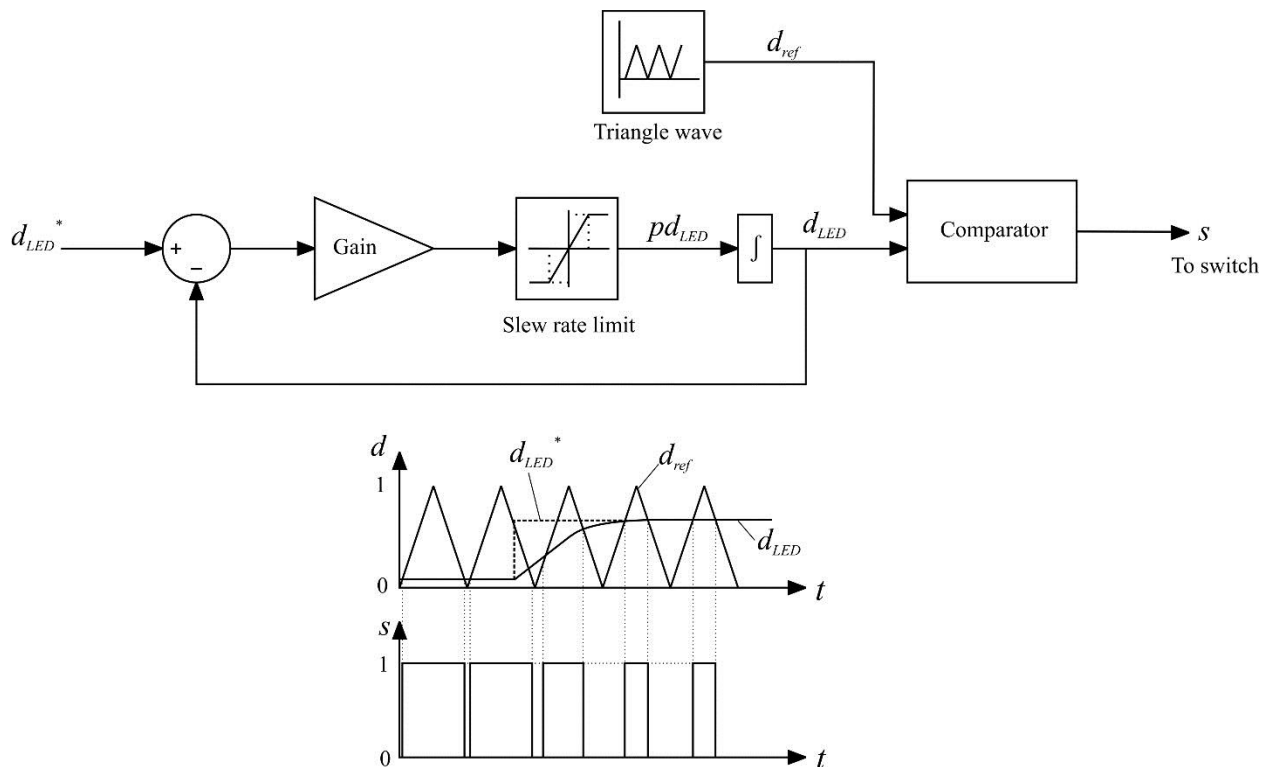


Figure 2.13 LED duty cycle control and PWM driver

### 2.2.5 Fixture-only simulation

In addition to the component described in Subsection 2.2.1-2.2.4, the fixture also includes an input filter and an output filter. They can each be modeled using two state variables,  $[v_s \ i_{Ls}]^T$  for the input filter, and  $[v_{Cld} \ i_{Lld}]^T$  for the output filter. Corresponding to the topology in Figure 2.8, the input of the input filter are  $i_s$  and  $v_r$ , and its output are  $i_{Ls}$  and  $v_s$ ; the input of the output filter are  $i_r$  and  $v_{ld}$ , and its output are  $i_{Lld}$  and  $v_{Cld}$ . The dynamics of these state variables are governed by

$$pv_s = \frac{1}{C_s}(-i_s - i_{Ls}) \quad (2.39)$$

$$pi_{Ls} = \frac{1}{L_s}(v_s - v_r - r_{Ls}i_{Ls}) \quad (2.40)$$

$$pv_{Cld} = \frac{1}{C_{ld}}(i_r - i_{Lld}) \quad (2.41)$$

$$pi_{Lld} = \frac{1}{L_{ld}}(v_{Cld} - v_{ld} - r_{Lld}i_{Lld}) \quad (2.42)$$

where  $r_{Ls}$  and  $r_{Lld}$  are inductor resistances.

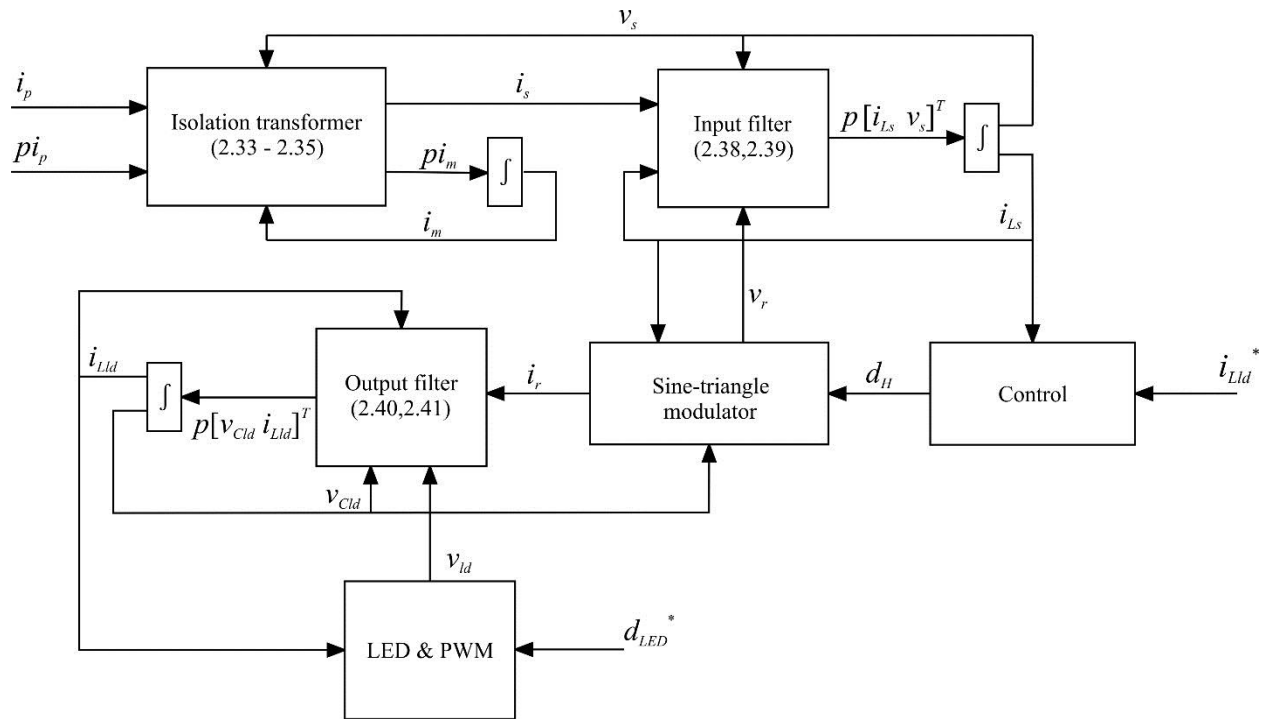


Figure 2.14 Fixture-only simulation diagram

Combining the fixture components, the fixture model block diagram is depicted in Figure 2.14. To study both the steady-state and the transient performance of the fixture, a case study of output level step change is illustrated below, using the parameters listed in Table 2.2. The ODE solver is Runge-Kutta (ODE4), and the time step is  $0.5 \mu\text{s}$ . The LED duty cycle command  $d_{LED}^*$  steps from 50% to 20% at  $t = 0.5 \text{ s}$ . The source of the fixture is assumed to be an ideal current source.

Figure 2.15 shows the steady-state waveforms of  $i_p$ ,  $v_p$ ,  $i_{Lld}$ ,  $i_{Ls}$ ,  $i_r$ ,  $v_r$ , and  $v_{Cld}$  when the LED duty cycle is set to 50%. It can be seen that corresponding to the sinusoidal input current  $i_p$ , the input voltage needed is very close to a sinusoidal waveform, which is desired for achieving good system performance with a current source introduced in 2.1. Meanwhile, the LED load current  $i_{Lld}$  is maintained close to its desired value with a reasonable amount of ripple, so that the primary design objective of producing a ‘square-wave’ LED current is achieved, as shown in the same plot. The high-frequency switching signal of the H-bridge is shown by comparing  $i_{Ls}$  to  $i_r$  and  $v_{Cld}$  to  $v_r$ . The waveforms show that by prudently choosing fixture parameters, the high-frequency switching components can be eliminated from the fixture outputs and the inputs.

The step response study is shown in Figure 2.16. The waveform of  $i_p$  shows an ideal sinusoidal current, while the required input voltage  $v_p$  to maintain this current is shown to shift with the load step change. The LED load current is shown to have 1.2A peak value, which is acceptable for not causing significant over heating issues. Figure 2.16 also shows the instantaneous input power  $P_{in}$ . It can be seen that a large percentage of the total power is reactive power, which is caused by the phase difference between  $v_p$  and  $i_p$  (since the voltage is leading the current, the fixture can be regarded as inductive load). The  $\lambda_m$  trace in Figure 2.16 shows that magnetizing flux linkage of the isolation transformer is very small relative to the  $\lambda - i$  curve in Figure 2.11, therefore it is reasonable to assume that the transformer is working in linear region or normal operation.

Table 2.2 Fixture parameters

Component	Value
Turns ratio ( $N_p/N_s$ )	1.019
Primary winding resistance ( $r_p$ )	0.15 $\Omega$
Secondary winding resistance ( $r_s$ )	0.07 $\Omega$
Transformer coefficient $\alpha$	0.0191
Transformer coefficient $\beta$	23.73
Transformer coefficient $L_0$	0.7 mH
Primary leakage inductance ( $L_{lp}$ )	0.357 mH
Secondary leakage inductance ( $L_{ls}$ )	0.197 mH
Input filter capacitance ( $C_s$ )	150 $\mu$ F
Input filter inductance ( $L_s$ )	1 mH
Input filter inductor resistance ( $r_{Ls}$ )	0.05 $\Omega$
Output filter capacitance ( $C_{ld}$ )	50 mF
Output filter inductance ( $L_{ld}$ )	4 mF
Output filter inductor resistance ( $r_{Lld}$ )	0.05 $\Omega$
Proportional gain ( $k_p$ )	2
Integrational gain ( $k_i$ )	20
Anti-windup gain ( $k_b$ )	3.5
Low-pass filter time constant ( $\tau$ )	2.7 ms
Desired load current ( $i_{LLd}^*$ )	0.8 A
LED parameter $i_0$	0.297 fA
LED parameter $v_0$	0.158 V
H-bridge switching frequency ( $f_{sw}$ )	30 kHz
Load parallel switching frequency ( $f_{swld}$ )	3 kHz
Duty cycle slew rate limit	5 s <sup>-1</sup>

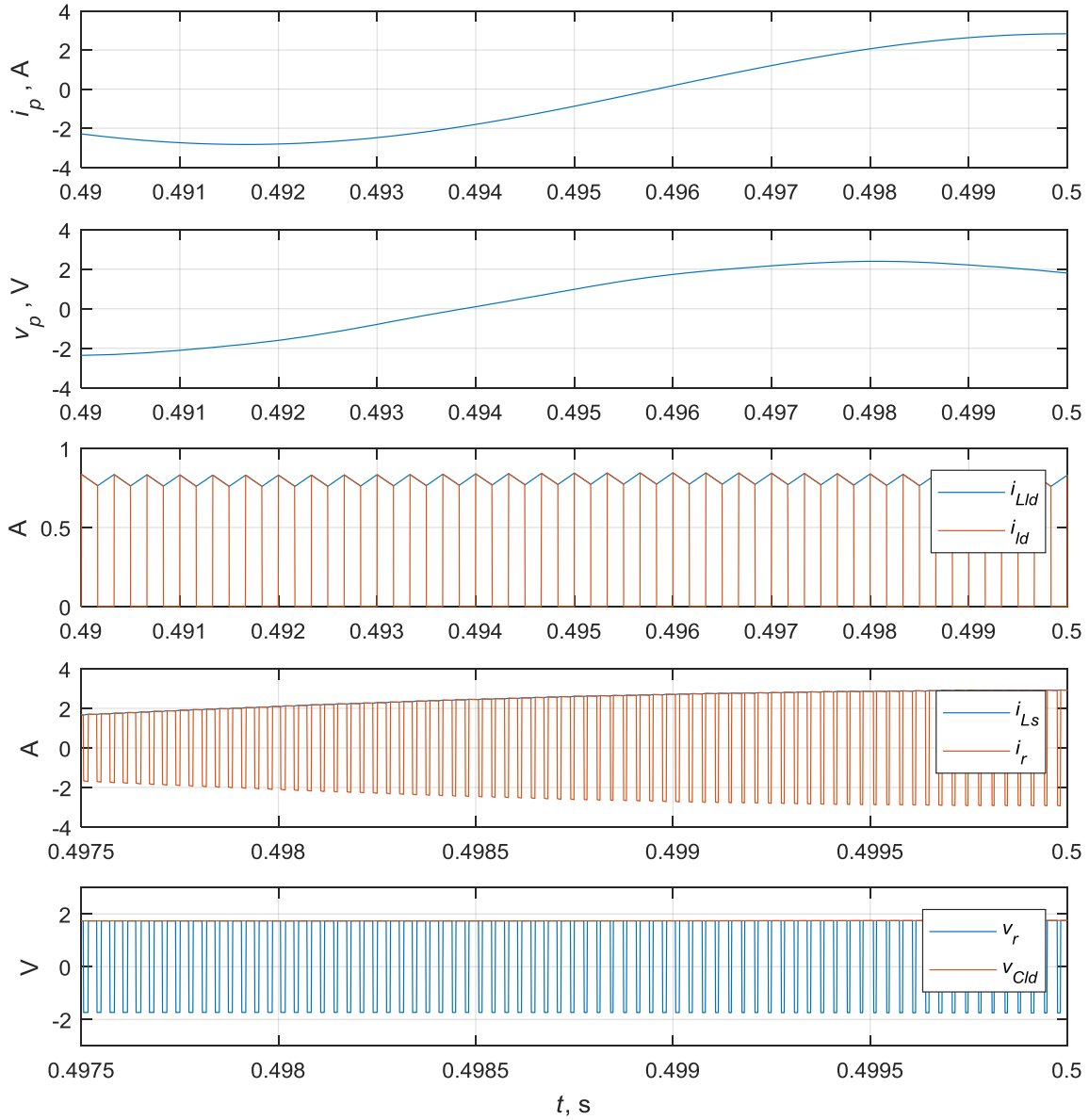


Figure 2.15 Fixture steady-state waveforms

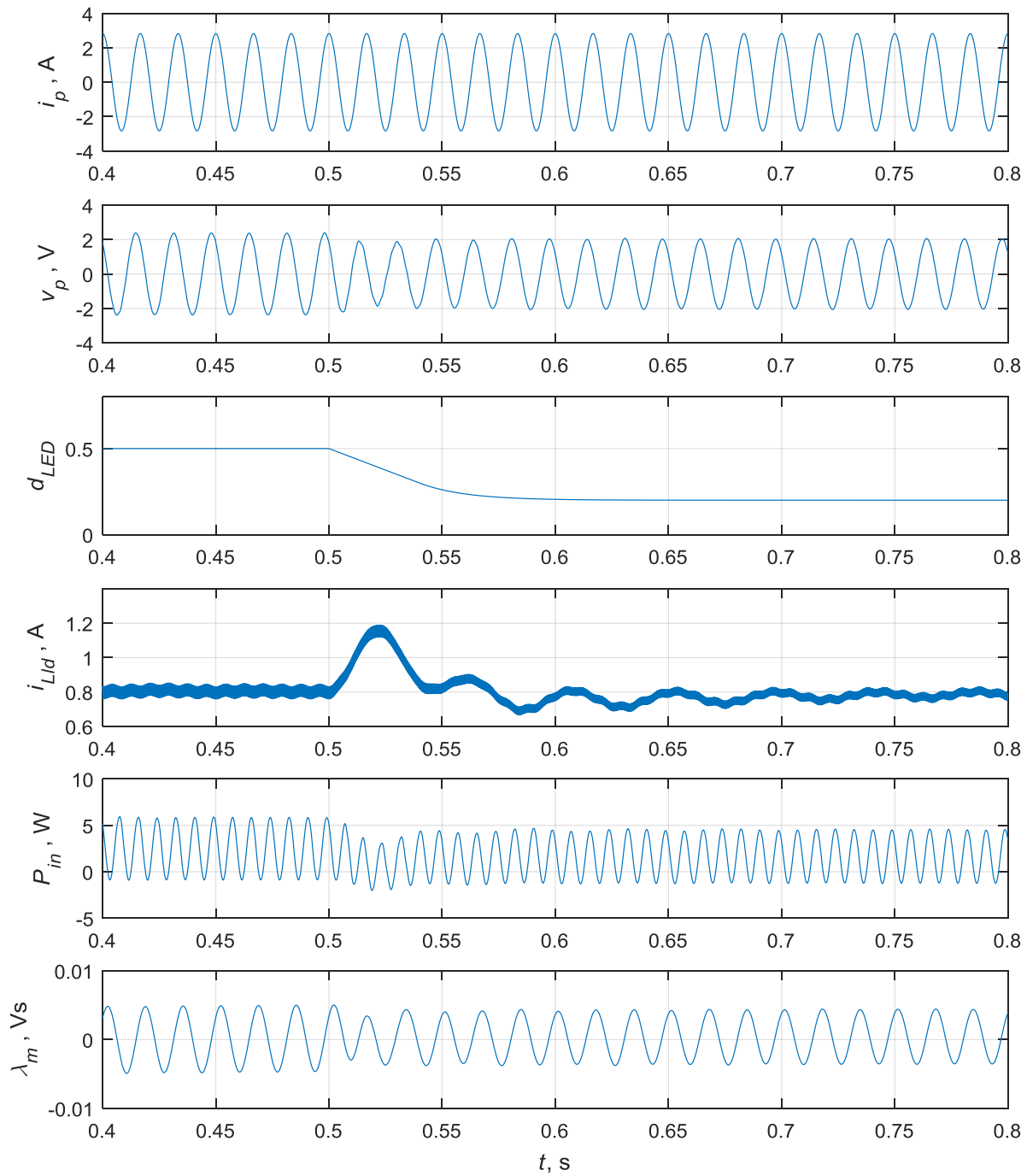


Figure 2.16 Fixture step-change waveforms

### 2.3 System Model and Simulation

In order to illustrate source-fixture interaction, a system consisting of one source and fifty fixtures in series is considered. Assuming that each fixture operates identically, the voltage across and current through each fixture will be equal. This is not true if transmission line effects are not negligible, in which case the system must be described as a distributed system. In practice, two types of transmission cables exist: both of them consist of a single copper conductor and insulation layers, and one of them contains a grounded metal screen. Either type of cable introduces inductances and capacitances to the ground. As an approximation, the transmission line resistance can be included in the primary winding resistance of the isolation transformers. As shown in Figure 2.17, the transmission line inductance can be modeled as a part of leakage inductance of isolation transformers  $L_{lp}$ . The capacitance between the cable conductor and the ground can crudely be modeled as a part of source output capacitance  $C_{ac}$ .

Instead of assuming a current-in voltage-out fixture model as in the stand-alone simulation, the fixture model becomes voltage-in current-out. The isolation transformer model must be modified accordingly. To this end, starting from the time derivative of the fixture transformer primary current (which is the transmission line current)

$$p i_{ac} = p i_p = \frac{1}{L_{lp}} (v_p - r_p i_p - v_m) \quad (2.43)$$

and substituting (2.43) to (2.33) yields

$$p i_m = \frac{v_s' - r_s' (i_m - i_p) + \frac{L_{ls}'}{L_{lp}} (v_p - r_p i_p)}{\left(1 + \frac{L_{ls}'}{L_{lp}}\right) \left(\frac{\alpha\beta}{\beta^2 i_m^2 + 1} + L_0\right) + L_{ls}'} \quad (2.44)$$

By adding (2.43) to the state dynamics and modifying (2.33) to (2.44),  $i_p$  is added to the state space model to the transformer stand-alone model in Subsection 2.2.3. Additionally, the voltage across each fixture is the output voltage of the source divided by the number of fixtures.

To study system transient performance due to different parameter combinations, two cases are studied and presented below. For both cases, the commanded LED duty cycle steps from 0% to 100%, which mimics a situation where the lighting system is working initially with all LEDs turned off, and at a certain time point all the LEDs are turned on simultaneously. Fifty fixtures are

connect in series and powered by one source. The system parameters used in Case 1 is listed in Table 2.3, and the modification to the parameters for Case 2 is listed in Table 2.4. The solver utilized here is the same as separated simulations illustrated in previous subsections, i.e. Runge-Kutta (ODE4), and the time step is  $0.5 \mu\text{s}$ .

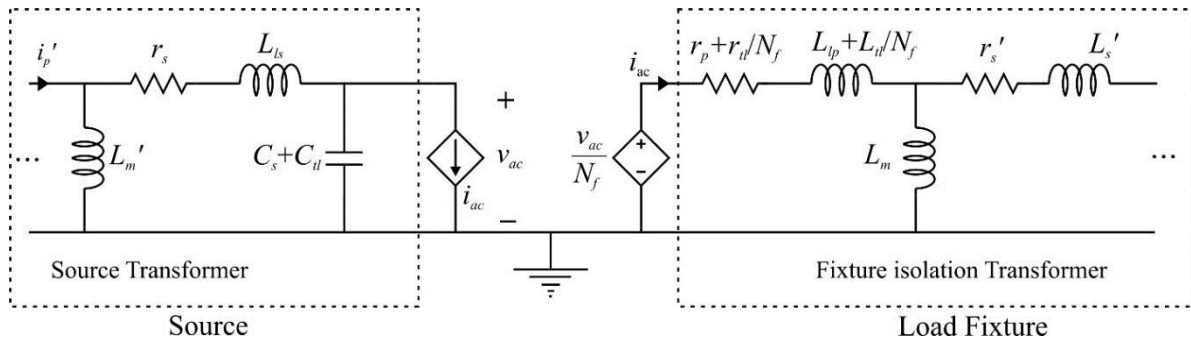


Figure 2.17 Transmission line model simplification

The simulation result for Case 1 is depicted in Figure 2.18. the ac current  $i_{ac}$  and its error with respect to the desired value  $i_{ac}^*$ , the actual LED duty cycle, the load voltage on each fixture  $v_p$ , the magnetizing flux linkage  $\lambda_m$  of fixture transformers, and the LED load current  $i_{LLd}$  are plotted. It can be seen that during the entire shown time interval, the error of  $i_{ac}$  is small. The fixture load voltage and magnetizing flux linkage follows the changing of LED duty cycle. The magnitude of the magnetizing flux linkage is small and can be regarded as within the ‘linear’ region. The LED load current shown in the fifth trace shows that with appropriate choice of system parameters, a good output performance can be achieved even though the current source is not ideal.

As a contrast, the simulation result of Case 2 is depicted in Figure 2.19. In this case, as can be seen, the AC current fails to return to the desired waveform. In this unstable situation, distortions occur in the waveforms of  $v_p$ ,  $\lambda_m$ , and  $i_{LLd}$ . This shows that with inappropriate choices of system parameters, instability will occur. The LED duty cycle also influence the stability, which indicates that a reliable system should be stable for all the useable LED duty cycle values.

Based on the analysis of the above two cases, it can be concluded that system stability is dependent on the system parameter choices. From a design prospective, this indicates that the stability should be considered as a design constrain. In order to obtain the stability of this system directly from the parameters instead of performing the time-domain simulation for all situations, the waveform-model needs to be converted to a LTI system, whose stability can be addressed

using Nyquist techniques. This will be carried out in Chapter 3 and 4.

Table 2.3 Case 1 system parameters

Source component	Value
Turns ratio ( $N_p/N_s$ )	0.7
Primary winding resistance ( $r_p$ )	$0.04 \Omega$
Secondary winding resistance ( $r_s$ )	$0.06 \Omega$
Magnetizing inductance ( $L_m$ )	0.2 H
Primary leakage inductance ( $L_{lp}$ )	0.1 mH
Secondary leakage inductance ( $L_{ls}$ )	0.5 mH
DC supply voltage ( $v_{dc}$ )	500 V
Output capacitance ( $C_{ac}$ )	$7.95 \mu\text{F}$
Hysteresis level ( $i_h$ )	0.1 A
Output current rms amplitude ( $i_{ac}^*$ )	2 A
Output current frequency ( $\omega_e$ )	$120\pi$ rad/s
Proportional gain ( $k_p$ )	0.25
Integrational gain ( $k_i$ )	0.35
Low-pass filter time constant $\tau$	1.6 ms
DC filter time constant $\tau_{dc}$	1.6 s
DC filter gain $k_{dc}$	2
Fixture component	
Turns ratio ( $N_p/N_s$ )	1.019
Primary winding resistance ( $r_p$ )	$0.15 \Omega$
Secondary winding resistance ( $r_s$ )	$0.07 \Omega$
Transformer coefficient $\alpha$	0.0191
Transformer coefficient $\beta$	23.73
Transformer coefficient $L_0$	0.7 mH
Primary leakage inductance ( $L_{lp}$ )	0.357 mH
Secondary leakage inductance ( $L_{ls}$ )	0.197 mH

Table 2.3 continued

Input filter capacitance ( $C_s$ )	150 $\mu$ F
Input filter inductance ( $L_s$ )	1 mH
Input filter inductor resistance ( $r_{Ls}$ )	0.05 $\Omega$
Output filter capacitance ( $C_{ld}$ )	50 mF
Output filter inductance ( $L_{ld}$ )	2 mH
Output filter inductor resistance ( $r_{Lld}$ )	0.05 $\Omega$
Proportional gain ( $k_p$ )	3
Integrational gain ( $k_i$ )	15.5
Anti-windup gain ( $k_b$ )	3.5
Low-pass filter time constant ( $\tau$ )	2.7 ms
Desired load current ( $i_{Lld}^*$ )	0.8 A
LED parameter $i_0$	0.297 fV
LED parameter $v_0$	0.158 A
H-bridge switching frequency ( $f_{sw}$ )	30 kHz
Load parallel switching frequency ( $f_{swld}$ )	3 kHz
Duty cycle slew rate limit	2.5 s <sup>-1</sup>
Transmission line component	
Transmission line resistance	0.05 $\Omega$
Transmission line inductance	0.043 mH
Transmission line capacitance	0.1 $\mu$ F

Table 2.4 Case 2 system parameter modification

Component modified	Case 1	Case2
Source output capacitance ( $C_{ac}$ )	7.95 $\mu$ F	18.95 $\mu$ F
Source proportional gain $k_p$	0.25	0.3
Fixture primary leakage inductance ( $L_{lp}$ )	0.357 mH	0.457 mH
Fixture input filter capacitance ( $C_s$ )	150 $\mu$ F	75 $\mu$ F
Fixture input filter inductance ( $L_s$ )	1 mH	2 mH

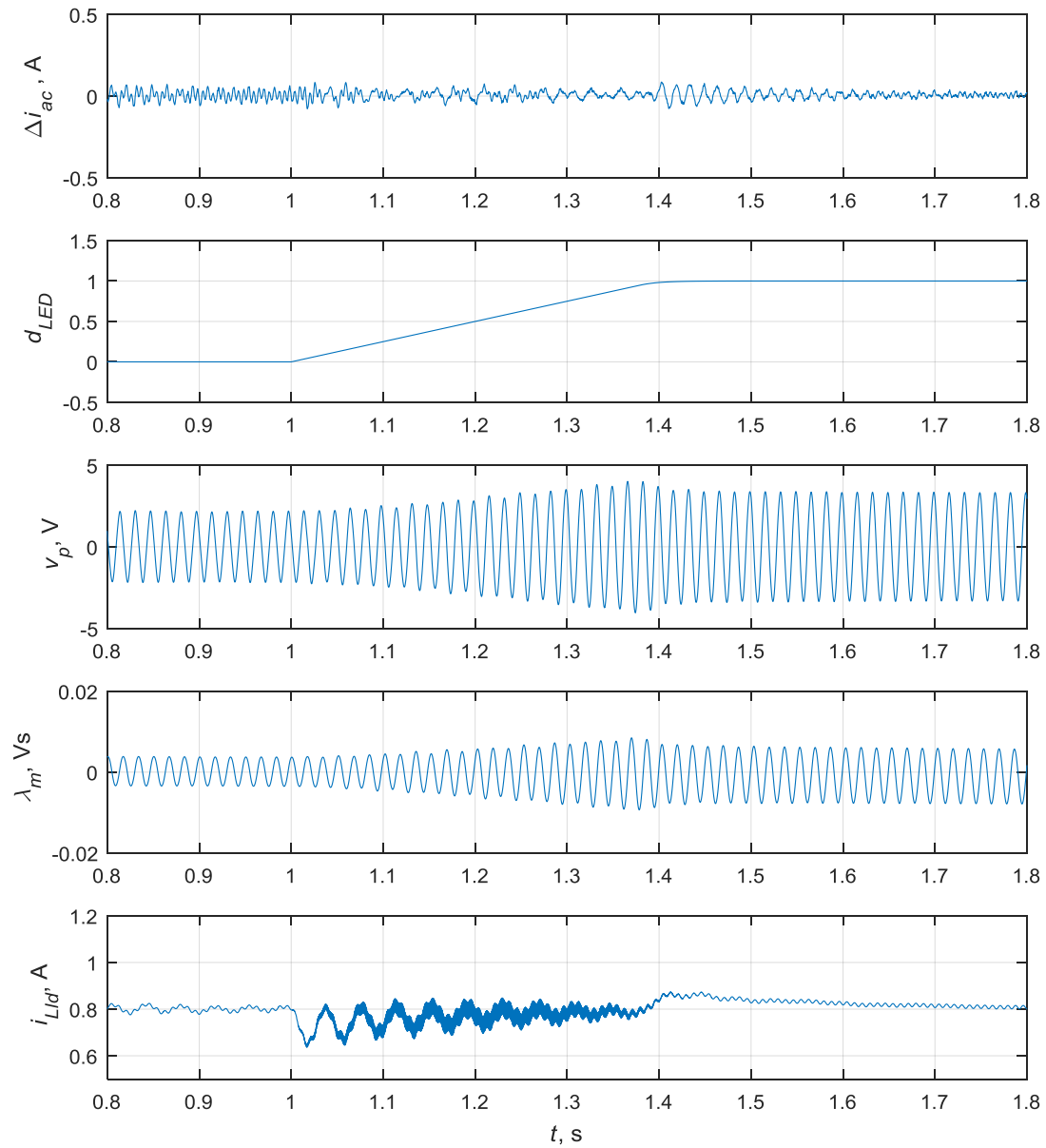


Figure 2.18 Case 1 system waveform-level model simulation result

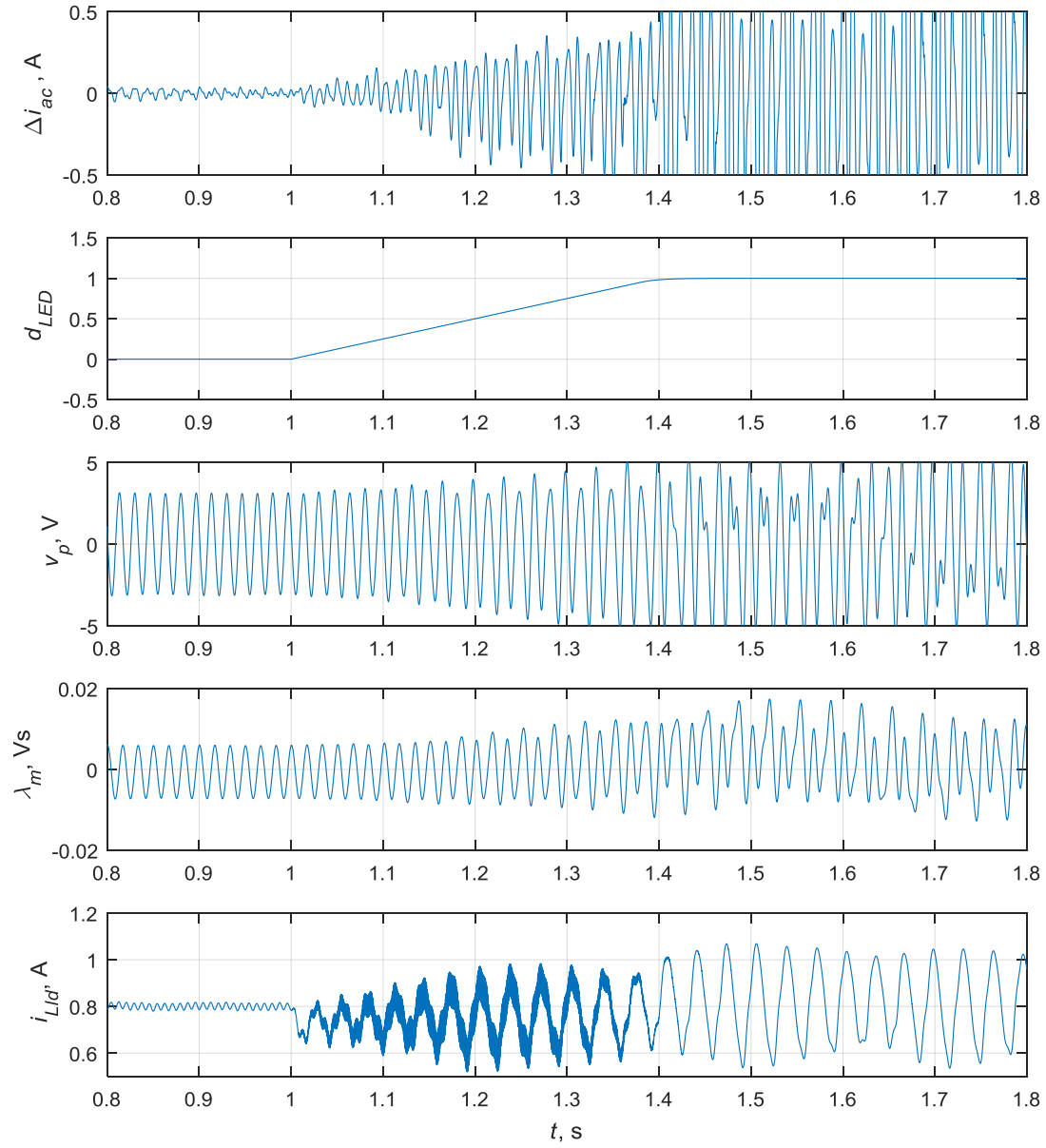


Figure 2.19 Case 2 system waveform-level model simulation result

### 3. AVERAGE-VALUE *qd* MODEL

In this chapter, the waveform-level single-phase AC current source and fixture models are used to derive average-value *qd* models so that the AC currents and voltages appears as constants under steady-state conditions. This property is useful for small-signal stability analysis. To this end, two techniques are employed in this chapter: *qd* reference frame transformation and average-value modeling (AVM). In Section 3.1, the definitions of *qd* variables, *qd* transformation and inverse *qd* transformation for a single-phase AC system are introduced, and their application to a linear state space model are illustrated. In Section 3.2, the average-value modeling method is introduced and two types of averaging method are included: fast-averaging of switching of power electronics and slow-averaging for rectifiers. Section 3.3 sets forth linear average-value *qd* model for the source and a nonlinear average-value *qd* model (AVQDM) for the fixture. The results of the stand-alone simulation of the two models are compared to the corresponding results in Chapter 2. Section 3.4 presents simulation results of the system consisting of the proposed source and fixture models, which are compared to the waveform-level model simulation results in Chapter 2.

#### 3.1 Reference Frame Transformation

##### 3.1.1 Introduction

In AC system modeling and analysis, a reference frame transformation is frequently used to convert three-phase or two-phase sinusoidal voltages and currents to DC quantities [37-42]. In single-phase AC system analysis, an imaginary *b*-phase system might be introduced to facilitate the application of two-phase *qd* transformation, which is discussed in detail in Chapter 5 of [30]. The definitions of *qd* and *ab* quantities are

$$\mathbf{f}_{qd} = \begin{bmatrix} f_q \\ f_d \end{bmatrix} \quad (3.1)$$

$$\mathbf{f}_{ab} = \begin{bmatrix} f_a \\ f_b \end{bmatrix} \quad (3.2)$$

where the variable *f* can be a voltage, current, or flux linkage. The two-phase *qd* transformation of *ab* variables is defined as

$$\mathbf{f}_{qd} = \mathbf{K}\mathbf{f}_{ab} \quad (3.3)$$

where

$$\mathbf{K} = \begin{bmatrix} \cos(\theta_e) & \sin(\theta_e) \\ \sin(\theta_e) & -\cos(\theta_e) \end{bmatrix} \quad (3.4)$$

and where  $\theta_e$  is the angular position of the synchronous reference frame. To recover the  $ab$  quantities from the  $qd$  quantities defined in (3.1), it can be shown that

$$\mathbf{f}_{ab} = \mathbf{K}^{-1}\mathbf{f}_{qd} \quad (3.5)$$

where

$$\mathbf{K}^{-1} = \mathbf{K} \quad (3.6)$$

The position of the synchronous reference frame  $\theta_e$  can be regarded as the angular position of the  $q$ -axis of this reference frame rotating at a constant speed  $\omega_e$  starting from 0 at  $t = 0$ . Suppose that the reference frame is chosen so that its angular frequency  $\omega_e$  is equal to the fundamental angular frequency of the AC system. Namely,  $\omega_e$  is the synchronous frequency of the system. Then, for steady-state conditions, an  $a$ -phase quantity in this system can be expressed in the form

$$f_a = \sqrt{2}F_s \cos(\theta_e + \phi_a) \quad (3.7)$$

where  $\phi_a$  represents the phase of the  $a$ -phase quantity relative to the  $q$ -axis. It is assumed that the  $b$ -phase system has exactly identical characteristics to the  $a$ -phase system for all frequency components, except that the phases of its fundamental component (at  $\omega_e$ ) are lagging the corresponding  $a$ -phase quantities by 90 degrees. Thus,

$$f_b = \sqrt{2}F_s \cos\left(\theta_e + \phi_a - \frac{\pi}{2}\right) = \sqrt{2}F_s \sin(\theta_e + \phi_a) \quad (3.8)$$

Applying the transformation in (3.3) and (3.4) to (3.7) and (3.8) yields

$$\mathbf{f}_{qd} = \begin{bmatrix} \sqrt{2}F_s \cos \phi_a \\ -\sqrt{2}F_s \sin \phi_a \end{bmatrix} \quad (3.9)$$

Therefore, any single-phase AC quantity in the form of (3.7) can be transformed into  $qd$  quantities as in (3.9) which appear as constants in steady-state conditions, and recovered from its  $qd$  quantities using (3.5) and (3.6).

For steady-state analysis, it is useful to convert the phasor representation of a single-phase ac quantity to its corresponding  $qd$  representation. To this end, define the phasor corresponding to the  $a$ -phase quantity in the form as in (3.7) as

$$\tilde{f}_a = F_s \angle \phi_a \quad (3.10)$$

whereupon

$$f_a = \text{Re}\{\sqrt{2}\tilde{f}_a e^{j\theta_e}\} = \sqrt{2}F_s \cos(\theta_e + \phi_a) \quad (3.11)$$

In the steady-state conditions, both  $F_s$  and  $\phi_a$  are constants. The phasor of the  $b$ -phase quantity whose angular position is lagging the  $a$ -phase quantity by 90 degrees becomes

$$\tilde{f}_b = -j\tilde{f}_a \quad (3.12)$$

which corresponds to the expression in (3.8)

$$f_b = \text{Re}\{\sqrt{2}\tilde{f}_b\} = \sqrt{2}F_s \sin(\theta_e + \phi_a) \quad (3.13)$$

It can be shown that the  $qd$  values corresponding to this phasor may be expressed as

$$\mathbf{f}_{qd} = \begin{bmatrix} \sqrt{2}F_s \cos \phi_a \\ -\sqrt{2}F_s \sin \phi_a \end{bmatrix} = \begin{bmatrix} \text{Re}\{\tilde{f}_a\} \\ -\text{Im}\{\tilde{f}_a\} \end{bmatrix} \quad (3.14)$$

Equivalently, the phasor of the  $a$ -phase quantity can be represented by the corresponding  $qd$  values using

$$\tilde{f}_a = f_q - jf_d \quad (3.15)$$

Therefore, if the steady-state phasor quantity of an AC signal is known, its  $qd$  representation can be obtained using (3.14) accordingly; if the steady-state  $qd$  values of an AC signal is known, its phasor quantity can also be obtained. Furthermore, if the steady-state phasors in a single-phase AC circuit can be calculated from system parameters, their corresponding  $qd$  quantities can be obtained. This will be used in calculating steady-state operational points of the system in Chapter 4. It should be noted that depending on the choice of initial position of the synchronous reference frame, the operational points can be different for the same system.

### 3.1.2 System transformation

From 3.1.1, the steady-state quantities in an AC system can be represented in both phasors and in  $qd$  forms equivalently. However, the dynamics of the  $qd$  quantities of single-phase AC systems remain uncertain. To illustrate the dynamics of the  $qd$  quantities of an AC system, it is

desirable to derive a new state space model where the states are the  $qd$  variables. Consider a linear system with  $n$  states in the  $a$ -phase and governed by the ODE

$$p\mathbf{x}_a = \mathbf{A}\mathbf{x}_a + \mathbf{B}\mathbf{u}_a \quad (3.16)$$

where  $\mathbf{A}$  is a  $n$ -by- $n$  matrix. Assume a  $b$ -phase system having identical characteristics to the  $a$ -phase system

$$p\mathbf{x}_b = \mathbf{A}\mathbf{x}_b + \mathbf{B}\mathbf{u}_b \quad (3.17)$$

Define the combined  $ab$  states and  $ab$  inputs as

$$\mathbf{x}_{ab} = \begin{bmatrix} \mathbf{x}_a \\ \mathbf{x}_b \end{bmatrix} \quad (3.18)$$

$$\mathbf{u}_{ab} = \begin{bmatrix} \mathbf{u}_a \\ \mathbf{u}_b \end{bmatrix} \quad (3.19)$$

The combined state vector is then governed by the ODE

$$p\mathbf{x}_{ab} = \begin{bmatrix} \mathbf{A} & \mathbf{0} \\ \mathbf{0} & \mathbf{A} \end{bmatrix} \mathbf{x}_{ab} + \begin{bmatrix} \mathbf{B} & \mathbf{0} \\ \mathbf{0} & \mathbf{B} \end{bmatrix} \mathbf{u}_{ab} \quad (3.20)$$

The combined  $qd$  states and  $qd$  inputs are defined as

$$\mathbf{x}_{qd} = \begin{bmatrix} \mathbf{x}_q \\ \mathbf{x}_d \end{bmatrix} \quad (3.21)$$

$$\mathbf{u}_{qd} = \begin{bmatrix} \mathbf{u}_q \\ \mathbf{u}_d \end{bmatrix} \quad (3.22)$$

It is convenient to define the  $qd$  transformation matrix for a system with  $n$  states in one phase as

$$\mathbf{K}^n = \begin{bmatrix} \cos(\theta_e)\mathbf{I}_n & \sin(\theta_e)\mathbf{I}_n \\ \sin(\theta_e)\mathbf{I}_n & -\cos(\theta_e)\mathbf{I}_n \end{bmatrix} \quad (3.23)$$

where  $\mathbf{I}_n$  is the identity matrix of the  $n$ 'th order. Defining

$$\mathbf{x}_{qd} = \mathbf{K}^n \mathbf{x}_{ab} \quad (3.24)$$

$$\mathbf{u}_{qd} = \mathbf{K}^n \mathbf{u}_{ab} \quad (3.25)$$

and substituting (3.24) and (3.25) into (3.20) yields

$$p\mathbf{x}_{qd} = \begin{bmatrix} \mathbf{A} & -\omega_e \mathbf{I}_n \\ \omega_e \mathbf{I}_n & \mathbf{A} \end{bmatrix} \mathbf{x}_{qd} + \begin{bmatrix} \mathbf{B} & \mathbf{0} \\ \mathbf{0} & \mathbf{B} \end{bmatrix} \mathbf{u}_{qd} = \mathbf{A}_{qd} \mathbf{x}_{qd} + \mathbf{B}_{qd} \mathbf{u}_{qd} \quad (3.26)$$

In conclusion, if an  $n$ -state LTI system can be modeled by a linear state space described as in (3.20), its  $qd$  transformed states are governed by (3.26). The two state space models are mathematically equivalent for arbitrary initial position of the synchronous reference frame.

## 3.2 Average-Value $Qd$ Modeling Of Linear System Components (Source)

### 3.2.1 Average-value modeling

Average-value modeling (AVM) has been used to reduce computational intensity in simulations of synchronous machine-rectifier systems [43], converter-machine systems [44-47] brushless DC machines [48], machine-load systems [49], PWM DC-DC converters [50-53] and many other applications. In a system where fast switching signal component with switching period  $T_{sw}$  is introduced, the fast average-value of a signal  $x(t)$  can be defined as

$$\hat{x}(t) = \frac{1}{T_{sw}} \int_{t-T_{sw}}^t x(\tau) d\tau \quad (3.27)$$

so that the fast switching behavior is neglected. Since  $T_{sw}$  is much smaller than the period of the fundamental components of the AC system (i.e. the synchronous frequency), the primary dynamics of the system are conserved in average-value modeling.

On the other hand, to address the relationship between the AC part and the DC part in the fixture so that in the steady state both the AC and DC signals are constant, a ‘slow’ averaging is also desired. The ‘slow’ averaging eliminates the ripple at harmonics of the fundamental frequency from a DC quantity, most notably the double fundamental frequency term. This half-cycle averaging is defined as

$$\bar{x}(t) = \frac{2}{T_e} \int_{t-T_e/2}^t x(\tau) d\tau \quad (3.28)$$

As also shown in Subsection 2.2.2, applying this half-cycle averaging to the output current of the rectifier yields a representation in which the DC current is constant in the steady-state.

The dynamics of the average-value signals are much less computationally intensive than in waveform-level modeling. Moreover, the ‘averaged’ signal is constant in the steady-state. This makes it straight forward to linearize the system description about a desired operating point, which in turn facilitates small-signal stability analysis.

### 3.2.2 Source average-value $qd$ model and simulation

The average-value  $qd$  model (AVQDM) for the source can be developed by first deriving its average-value model in state space form: all the time derivatives of the states are expressed in terms of states and inputs; then, applying (3.25) the  $qd$  state space model is determined.

Consider the source model shown in Figure 3.1, a switching signal is generated by the H-bridge inverter. The fundamental (synchronous) frequency of the current generated by this inverter is equal to the frequency of the commanded current  $i_p^*$  from the control shown in Figure 2.2. The switching frequency due to this inverter depends on dc supply voltage, system impedance and the hysteresis level, and is usually much larger than the fundamental frequency. Therefore, the average-value model of the source can be obtained by assuming that the fast average of the transformer primary current is equal to the commanded current  $i_p^*$ .

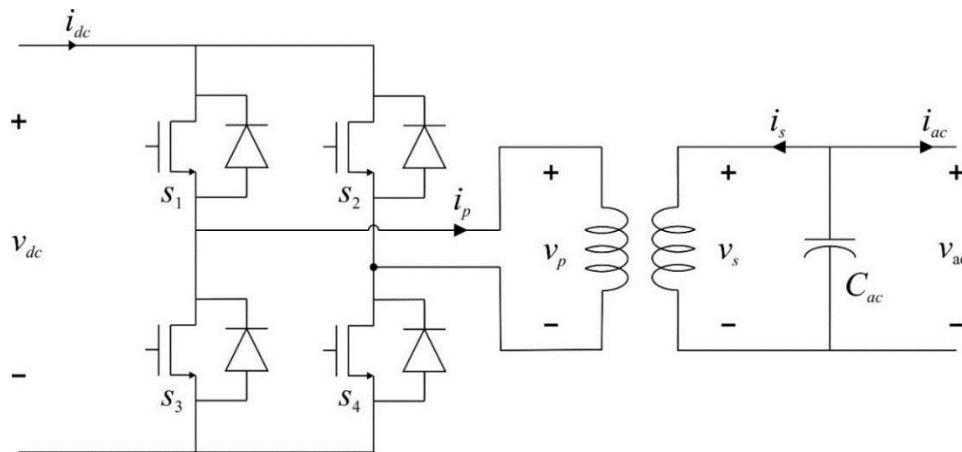


Figure 3.1 Current source topology

Considering the control diagram in Figure 3.2, the AC output current  $i_{ac}$  is the feedback signal to the source control. The AC output voltage  $v_{ac}$  is controlled so that  $i_{ac}$  follows the desired current  $i_{ac}^*$ . As the source consists of linear components and a linear control law, the source average-value model becomes a linear system.

Combining all the essential states in the source schematic and the control to describe the system status of the source, five state variables and two input variables are needed. In particular,

$$\mathbf{x} = [v_{ac} \ i_s \ x_{c1} \ x_{c2} \ x_{c3}]^T \quad (3.29)$$

$$\mathbf{u} = \begin{bmatrix} i_{ac} & i_{ac}^* \end{bmatrix}^T \quad (3.30)$$

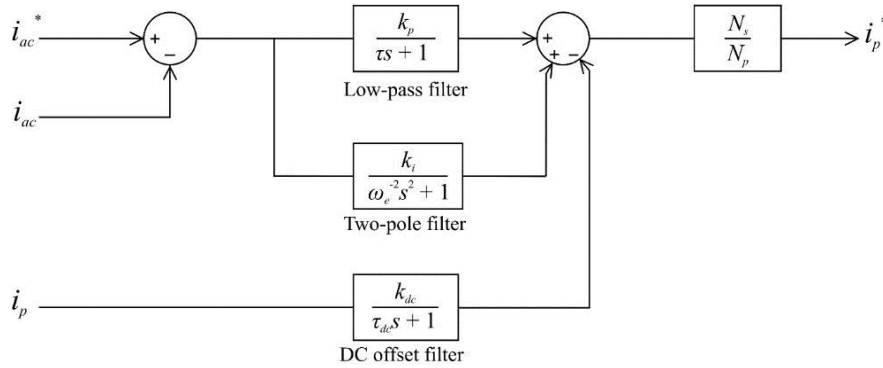


Figure 3.2 Current source control

Considering the circuit shown in Figure 3.1, the dynamics of  $v_{ac}$  is governed by

$$p v_{ac} = \frac{1}{C_{ac}} (-i_s - i_{ac}) \quad (3.31)$$

Next, time derivative of the secondary current may be expressed by

$$p i_s = \frac{1}{L_{ts}} (v_{ac} - v_m' - r_s i_s) \quad (3.32)$$

where  $v_m'$  is the magnetizing voltage referred to the secondary winding, which can be shown as

$$v_m' = L_m' (p i_s + p i_p') \quad (3.33)$$

and where  $i_p'$  and  $L_m$  are the primary current and transformer mutual inductance referred to the secondary winding, respectively. Substituting (3.33) to (3.32) yields

$$p i_s = \frac{1}{L_{ts} + L_m'} (v_{ac} - L_m' p i_p' - r_s i_s) \quad (3.34)$$

The remaining three states,  $x_{c1}$ ,  $x_{c2}$  and  $x_{c3}$  are the control state variables, which are governed by the control transfer function as presented in Figure 2.2 as

$$i_p = \frac{N_s}{N_p} \left( \frac{k_i}{\omega_e^{-2} s^2} + \frac{k_p}{\tau_p s + 1} \right) (i_{ac}^* - i_{ac}) \quad (3.35)$$

Thus, the referred primary current may be written as

$$i_p' = \left( \frac{k_i}{\omega_e^{-2} s^2} + \frac{k_p}{\tau_p s + 1} \right) (i_{ac}^* - i_{ac}) \quad (3.36)$$

In order to incorporate (3.36) into (3.34) so that the dynamics of  $i_s$  can be expressed in terms of state variables and input variables, it is desirable to convert (3.36) to a state space form where the output is  $pi_p'$ . To achieve this, first express (3.36) as

$$si_p' = \left( \frac{(k_i \omega_e^2 - k_p \tau_p^{-2})s^2 + k_i \tau_p^{-1} \omega_e^2 s - k_p \tau_p^{-2} \omega_e^2}{s^3 + \tau_p^{-1} s^2 + \omega_e^2 s + \tau_p^{-1} \omega_e^2} + \frac{k_p}{\tau_p} \right) (i_{ac}^* - i_{ac}) \quad (3.37)$$

To convert (3.37) to state space form, define

$$Y(s) = \left[ (k_i \omega_e^2 - k_p \tau_p^{-2})s^2 + k_i \tau_p^{-1} \omega_e^2 s - k_p \tau_p^{-2} \omega_e^2 \right] Z(s) \quad (3.38)$$

$$U(s) = \left[ s^3 + \tau_p^{-1} s^2 + \omega_e^2 s + \tau_p^{-1} \omega_e^2 \right] Z(s) \quad (3.39)$$

where  $Y(s) = si_p' - k_p(i_{ac}^* - i_{ac})$ , and  $U(s) = i_{ac}^* - i_{ac}$ . Converting (3.38) and (3.39) to time-domain,

$$y(t) = (k_i \omega_e^2 - k_p \tau_p^{-2}) \ddot{z}(t) + k_i \tau_p^{-1} \omega_e^2 \dot{z}(t) - k_p \tau_p^{-2} \omega_e^2 z(t) \quad (3.40)$$

$$u(t) = \ddot{z}(t) + \tau_p^{-1} \dot{z}(t) + \omega_e^2 z(t) \quad (3.41)$$

Defining  $[x_{c1} \ x_{c2} \ x_{c3}]^T = [\ddot{z} \ \dot{z} \ z]^T$ , (3.40) and (3.41) yields

$$p \begin{bmatrix} x_{c1} \\ x_{c2} \\ x_{c3} \end{bmatrix} = \begin{bmatrix} -\tau_p^{-1} & -\omega_e^2 & -\omega_e^2 \tau_p^{-1} \\ 1 & 0 & 0 \\ 0 & 1 & 0 \end{bmatrix} \begin{bmatrix} x_{c1} \\ x_{c2} \\ x_{c3} \end{bmatrix} + \begin{bmatrix} -1 & 1 \\ 0 & 0 \\ 0 & 0 \end{bmatrix} \begin{bmatrix} i_{ac}^* \\ i_{ac} \end{bmatrix} \quad (3.42)$$

$$pi_p' = \begin{bmatrix} k_i \omega_e^2 - k_p \tau_p^{-2} & k_i \tau_p^{-1} \omega_e^2 & -k_p \tau_p^{-2} \omega_e^2 \end{bmatrix} \begin{bmatrix} x_{c1} \\ x_{c2} \\ x_{c3} \end{bmatrix} + \begin{bmatrix} -\frac{k_p}{\tau_p} & \frac{k_p}{\tau_p} \end{bmatrix} \begin{bmatrix} i_{ac}^* \\ i_{ac} \end{bmatrix} \quad (3.43)$$

Substituting (3.41) to (3.33) yields

$$pi_s = \frac{1}{L_{ls} + L_m} (v_{ac} - r_s i_s) - \frac{L_m}{L_{ls} + L_m} \left[ (k_i \omega_e^2 - k_p \tau_p^{-2}) x_{c1} + (k_i \tau_p^{-1} \omega_e^2) x_{c2} + (-k_p \tau_p^{-2} \omega_e^2) x_{c3} + \frac{k_p}{\tau_p} (i_{ac}^* - i_{ac}) \right] \quad (3.44)$$

Using the state variable and input definitions in (3.27) and (3.38), the ODEs (3.29), (3.40) and (3.42) can be rearranged in the form of  $px = \mathbf{Ax} + \mathbf{Bu}$  where

$$\mathbf{A} = \begin{bmatrix} 0 & -\frac{1}{C_s} & 0 & 0 & 0 \\ \frac{1}{L_{ls}+L'_m} & -\frac{r_s}{L_{ls}+L'_m} & -\frac{L'_m}{L_{ls}+L'_m}(k_i\omega_e^2-k_p\tau_p^{-2}) & -\frac{L'_m}{L_{ls}+L'_m}k_i\tau_p^{-1}\omega_e^2 & \frac{L'_m}{L_{ls}+L'_m}k_p\tau_p^{-2}\omega_e^2 \\ 0 & 0 & -\tau_p^{-1} & -\omega_e^2 & -\omega_e^2\tau_p^{-1} \\ 0 & 0 & 1 & 0 & 0 \\ 0 & 0 & 0 & 1 & 0 \end{bmatrix} \quad (3.45)$$

$$\mathbf{B} = \begin{bmatrix} -\frac{1}{C_{ac}} & 0 \\ \frac{L'_m}{L_{ls}+L'_m}\frac{k_p}{\tau_p} & -\frac{L'_m}{L_{ls}+L'_m}\frac{k_p}{\tau_p} \\ -1 & 1 \\ 0 & 0 \\ 0 & 0 \end{bmatrix} \quad (3.46)$$

Finally, the source average-value  $qd$  model can be derived by substituting the  $\mathbf{A}$  and  $\mathbf{B}$  matrices in (3.41) and (3.42) to (3.27), which yields the form of  $p\mathbf{x}_{qds} = \mathbf{A}_{qds}\mathbf{x}_{qds} + \mathbf{B}_{qds}\mathbf{u}_{qds}$  with

$$\mathbf{x}_{qds} = [v_{acq} \quad i_{sq} \quad x_{c1q} \quad x_{c2q} \quad x_{c3q} \quad v_{acd} \quad i_{sd} \quad x_{c1d} \quad x_{c2d} \quad x_{c3d}]^T \quad (3.47)$$

$$\mathbf{u}_{qds} = [i_{acq} \quad i_{acq}^* \quad i_{acd} \quad i_{acd}^*]^T \quad (3.48)$$

$$\mathbf{A}_{qds} = \begin{bmatrix} \mathbf{A} & -\omega_e \mathbf{I}_5 \\ \omega_e \mathbf{I}_5 & \mathbf{A} \end{bmatrix} \quad (3.49)$$

$$\mathbf{B}_{qds} = \begin{bmatrix} \mathbf{B} & \mathbf{0} \\ \mathbf{0} & \mathbf{B} \end{bmatrix} \quad (3.50)$$

The output of the source model is the ac output voltage  $v_{ac}$  as shown in Figure 2.1. Accordingly, the output of the  $qd$  model is  $[v_{acq} \quad v_{acd}]^T$ , which can be obtained from the (3.43) as

$$\begin{bmatrix} v_{acq} \\ v_{acd} \end{bmatrix} = \mathbf{C}_s \mathbf{x}_{qds} = \begin{bmatrix} 1 & 0 & 0 & 0 & 0 & 0 & 0 & 0 & 0 & 0 \\ 0 & 0 & 0 & 0 & 0 & 1 & 0 & 0 & 0 & 0 \end{bmatrix} \begin{bmatrix} \mathbf{x}_q \\ \mathbf{x}_d \end{bmatrix} \quad (3.51)$$

In conclusion, the source average-value  $qd$  model in a state space form is established by (3.43)-(3.49). It is a current-in voltage-out LTI system. To verify this AVQDM, the case study in subsection 2.1.4 is repeated. In this case study, the source is connected to a series L-R load, and the load resistance changes step at 0.5 second. As shown in Figure 3.3, the steady-state values of the  $qd$  quantities of  $i_{ac}$ ,  $v_{ac}$ , and  $i_p$  appear as constants in steady-states, and their step-responses are consistent with DC signals.

Figure 3.4 illustrates the comparison of waveforms of the WLM and AVQDM for the same step response as in subsection 2.1.4. The recovered single-phase ac signals are obtained using (3.5). In this case study, the solver used is variable-step ODE23 (Bogacki-Shampine), which greatly decrease the runtime of the model comparing the WLM. It can be seen that the high-frequency components of  $i_p$  and  $i_s$  waveforms are neglected in the AVQDM, while their dominant components are preserved. The filtered output signals,  $i_{ac}$  and  $v_{ac}$  are identical in both modeling methods. In conclusion, the source average-value  $qd$  model well represents both the steady-state and dynamic waveforms.

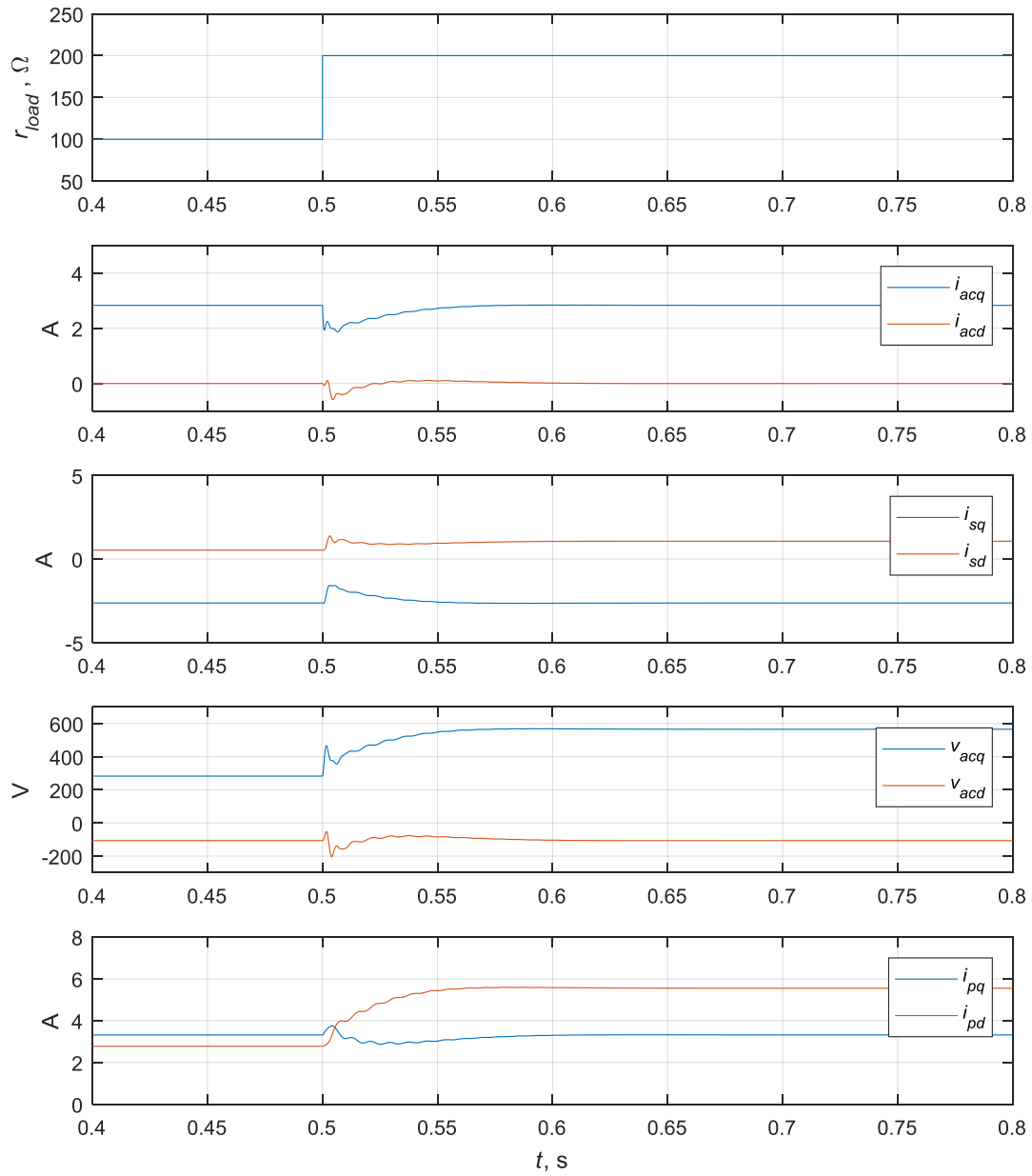


Figure 3.3 Source average-value  $qd$  waveforms

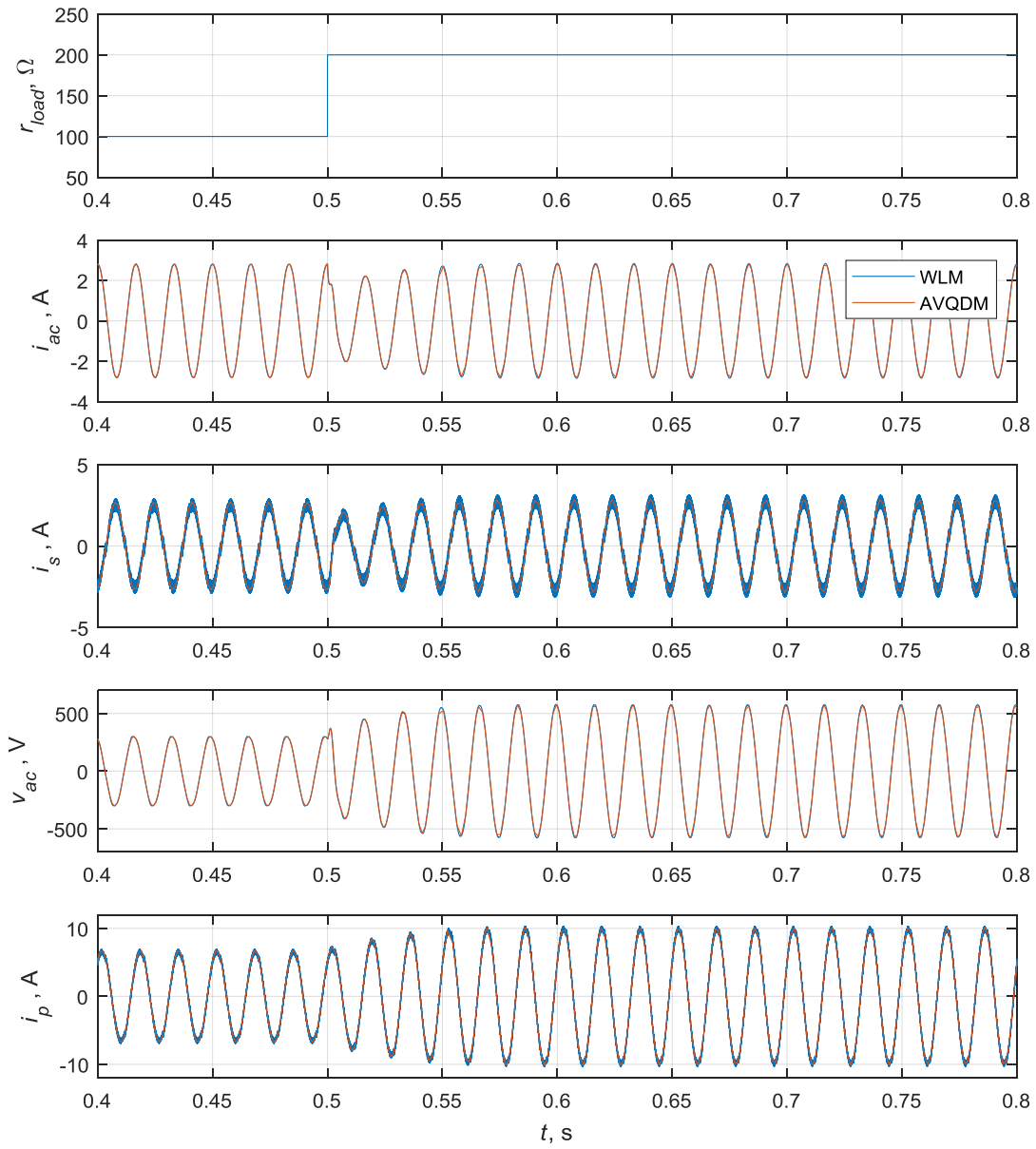


Figure 3.4 Source waveforms comparison

### 3.3 Average-Value $Qd$ Modeling Of Nonlinear System Components (Load)

#### 3.3.1 Approximation for fast-switching and rectifiers

Corresponding to the source AVQDM, the load fixture model will be designed to be voltage-in current-out. Consider the topology shown in Figure 3.5. This system can be divided into an AC part to the left side of the H-bridge and a DC part to the right side of the H-bridge. The main difficulty of developing an AVQDM for the load fixture is to establish the current and voltage relationship between the two parts.

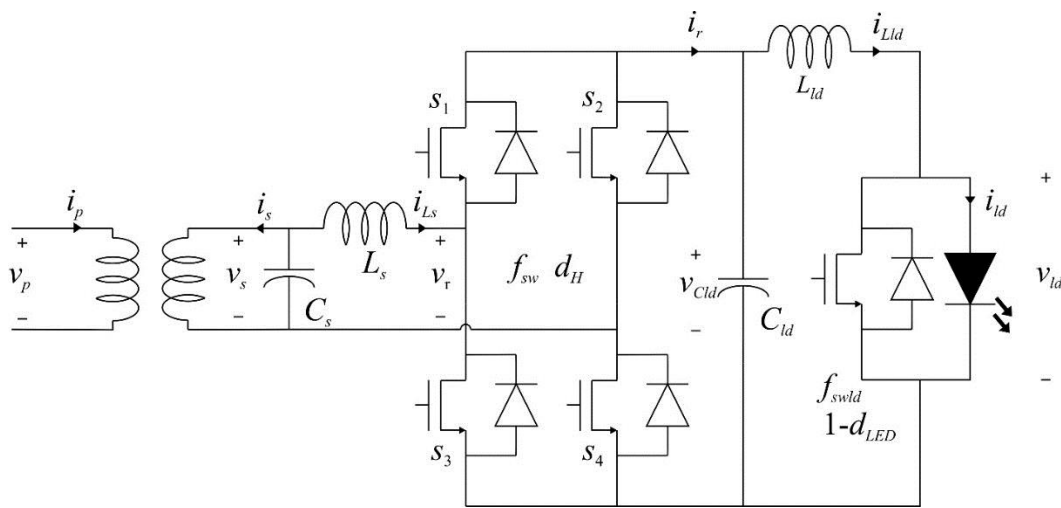


Figure 3.5 Load fixture topology (repeated from Figure 2.8)

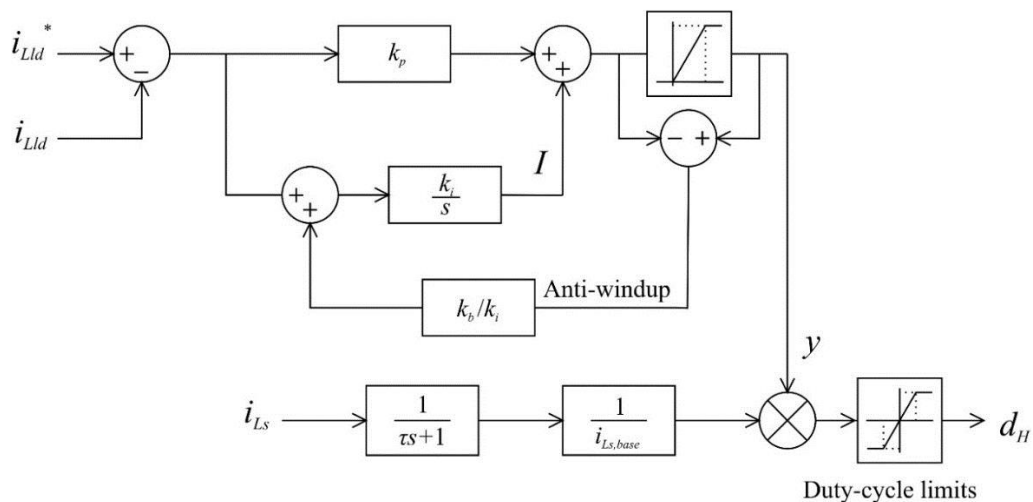


Figure 3.6 Load fixture control (repeated from Figure 2.10)

A fast switching signal is generated by the H-bridge which works as an active rectifier. In AVM, this fast switching is ‘averaged’ so that the rectified current can be expressed as in (2.19) where

$$\hat{i}_r = d_H i_{Ls} \quad (3.52)$$

In (3.52),  $d_H$  is the duty cycle of the H-bridge. In Figure 3.6, the  $i_{Ls}$  filter with time constant  $\tau$  is neglected, because the purpose of the filter is to eliminate the fast switching components, which has little influence. Therefore,

$$d_H = \frac{y}{i_{Ls,base}} i_{Ls} \quad (3.53)$$

Substituting (3.53) to (3.52) yields

$$\hat{i}_r = \frac{y}{i_{Ls,base}} i_{Ls}^2 \quad (3.54)$$

Thus the waveform of  $i_r$  will have a dc part and a low frequency AC part at double the fundamental frequency of  $i_{Ls}$ . Given the large time-constant of the output filter consisted with  $C_{ld}$  and  $L_{ld}$ ,  $i_r$  can be approximated with the ‘slow’ average defined in subsection 3.2.1 as

$$\bar{i}_r = \frac{1}{\pi} \int_{\theta_e - \pi}^{\theta_e} i_r d\theta_e = \frac{1}{i_{Ls,base}} \frac{1}{\pi} \int_{\theta_e - \pi}^{\theta_e} y i_{Ls}^2 d\theta_e \quad (3.55)$$

To simplify (3.55), it is assumed that the PI control output  $y$  is independent of  $\theta_e$ . This is true in steady-state, and during transient it provides a reasonable approximation. Applying this approximation on (3.55) yields

$$\bar{i}_r = \frac{y}{i_{Ls,base}} \frac{1}{\pi} \int_{\theta_e - \pi}^{\theta_e} i_{Ls}^2 d\theta_e \quad (3.56)$$

As shown in Subsection 3.1.1, an imaginary  $b$ -phase can be introduced corresponding to the DC part in order to perform the two-phase  $qd$  transformation. The  $a$ -phase (the original phase) and the  $b$ -phase (the imaginary phase whose fundamental frequency component is lagging the  $a$ -phase by 90 degrees)  $i_r$  can be expressed using

$$\bar{\mathbf{i}}_{rab} = \frac{1}{i_{Ls,base}} \frac{1}{\pi} \begin{bmatrix} y_a \int_{\theta_e - \pi}^{\theta_e} i_{Lsa}^2 d\theta_e \\ y_b \int_{\theta_e - \pi}^{\theta_e} i_{Lsb}^2 d\theta_e \end{bmatrix} \quad (3.57)$$

The  $a$ - and  $b$ - phase  $i_{Ls}$  may be represented in form of  $qd$  values as

$$\mathbf{i}_{Lsab} = \mathbf{K}^{-1} \mathbf{i}_{Lsqd} = \begin{bmatrix} i_{Lsq} \cos \theta_e + i_{Lsd} \sin \theta_e \\ i_{Lsq} \sin \theta_e - i_{Lsd} \cos \theta_e \end{bmatrix} \quad (3.58)$$

Substituting (3.58) to (3.57) yields

$$\bar{\mathbf{i}}_{rab} = \frac{1}{2i_{Ls,base}} (i_{Lsq}^2 + i_{Lsd}^2) \mathbf{y}_{ab} \quad (3.59)$$

Therefore, (3.59) establishes the relationship between the DC current and the  $qd$  values of the AC part currents.

Another difficulty remains in finding the relationship between  $v_r$  and  $v_{Cld}$ . It can be shown that for the assumed two-phase system

$$\mathbf{v}_{rab} = \begin{bmatrix} v_{ra} \\ v_{rb} \end{bmatrix} = \begin{bmatrix} d_{Ha} v_{Clda} \\ d_{Hb} v_{Cldb} \end{bmatrix} = \frac{1}{i_{Ls,base}} \begin{bmatrix} y_a v_{Clda} & 0 \\ 0 & y_b v_{Cldb} \end{bmatrix} \begin{bmatrix} i_{Lsa} \\ i_{Lsb} \end{bmatrix} \quad (3.60)$$

Therefore the  $qd$  representation of  $v_r$  can be derived by

$$\begin{aligned} \mathbf{v}_{rqd} &= \frac{1}{i_{Ls,base}} \mathbf{K} \begin{bmatrix} y_a v_{Clda} & 0 \\ 0 & y_b v_{Cldb} \end{bmatrix} \mathbf{K}^{-1} \mathbf{i}_{Lsqd} \\ &= \frac{1}{i_{Ls,base}} \begin{bmatrix} y_a v_{Clda} \cos^2(\theta_e) + y_b v_{Cldb} \sin^2(\theta_e) & (y_a v_{Clda} - y_b v_{Cldb}) \sin(\theta_e) \cos(\theta_e) \\ (y_a v_{Clda} - y_b v_{Cldb}) \sin(\theta_e) \cos(\theta_e) & y_a v_{Clda} \sin^2(\theta_e) + y_b v_{Cldb} \cos^2(\theta_e) \end{bmatrix} \mathbf{i}_{Lsqd} \end{aligned} \quad (3.61)$$

In steady state,  $\mathbf{i}_{Lsqd}$  appears constant; it is therefore assumed that  $\mathbf{i}_{Lsqd}$  is independent of  $\theta_e$ . As an approximation,  $\mathbf{v}_{rqd}$  can be represented by taking the half-cycle average of the matrix components in (3.61) as done in (3.55). This yields

$$\bar{\mathbf{v}}_{rqd} = \frac{1}{2i_{Ls,base}} \begin{bmatrix} y_a v_{Clda} + y_b v_{Cldb} & 0 \\ 0 & y_a v_{Clda} + y_b v_{Cldb} \end{bmatrix} \mathbf{i}_{Lsqd} \quad (3.62)$$

Since  $i_r$  is a DC current, it should be identical in  $a$  and  $b$  phase. Therefore, it is reasonable to model the DC part as an actual DC subsystem rather than a two-phase AC system. The input ( $i_r$ ) and the output ( $\mathbf{v}_{rqd}$ ) of this DC subsystem can be expressed as

$$i_r = i_{ra} = i_{rb} = \frac{1}{2i_{Ls,base}} (i_{Lsq}^2 + i_{Lsd}^2) y \quad (3.63)$$

$$\mathbf{v}_{rqd} = \frac{y v_{Cld}}{i_{Ls,base}} \mathbf{i}_{Lsqd} \quad (3.64)$$

At this point, the current and voltage relationships between the AC and DC parts are established using (3.63) and (3.64); the AC part is modeled as a two-phase ( $qd$ ) subsystem and the DC part is modeled as a DC subsystem.

### 3.3.2 Fixture average-value state-space model

Having the current and voltage relationship between the AC and DC parts, and assuming that the DC part is a single-phase subsystem, the fixture state space model ODEs can be derived as follows. Consider the DC part, which contains the output filter and the LED driver as shown in Figure 3.5, two state variables  $v_{Cld}$  and  $i_{Lld}$  are used to describe the dynamics of this part. Using the LED characteristic from subsection 2.2.4, it can be shown that

$$pv_{Cld} = \frac{1}{C_{ld}} \left[ \frac{1}{2i_{Ls,base}} (i_{Lsq}^2 + i_{Lsd}^2) y - i_{Lld} \right] \quad (3.65)$$

$$pi_{Lld} = \frac{1}{L_{ld}} \left[ v_{Cld} - r_{Lld} i_{Lld} - d_{LED} v_0 \ln \left( \frac{i_{Lld}}{i_0} + 1 \right) \right] \quad (3.66)$$

The PI control output  $y$  in the above equations is governed by

$$y = k_i I + k_p (i_{Lld}^* - i_{Lld}) \quad (3.67)$$

where the integrator variable  $I$  is governed by

$$pI = i_{Lld}^* - i_{Lld} \quad (3.68)$$

Now consider the AC part of the load fixture. A linear model of the isolation transformer will be used (which is identical to the source transformer model in Subsection 2.1.3) in steady of the nonlinear model described in Subsection 2.2.3, where the arctangent function is utilized to demonstrate saturation. As can be seen in the WLM simulation results in Figure 2.16 and 2.19, the magnetizing flux linkage usually does not exceed 0.01 Vs during steady state. According to the transformer characterize as shown in Figure 2.11, this value is relatively small so that the linear approximation is adequate.

The linearized transformer model can be expressed as in (2.7-2.14) and the primary and referred secondary currents are used as states. The input filter and output filter is described in (2.38-2.41). The input of the whole fixture model is  $v_p$  and the output of this model is the primary current  $i_p$ .

Combining the equations above, the fixture average-value  $qd$  model can be formulated by the state vector and input vector

$$\mathbf{x} = [i_{pq}' \quad i_{sq}' \quad v_{sq} \quad i_{Lsq} \quad i_{pd}' \quad i_{sd}' \quad v_{sd} \quad i_{Lsd} \quad v_{Cld} \quad i_{Lld} \quad I]^T \quad (3.69)$$

$$\mathbf{u} = [v_{pq} \quad v_{pd} \quad i_{Lld}^* \quad d_2]^T \quad (3.70)$$

where the single-phase states are governed by (3.63-3.66). Expanding the matrix form system ODE as in (3.29), the ODEs describing the AC part become

$$p i_{pq}' = \frac{(L_{ls}' + L_m)(v_{acq} - r_p i_{pq}') - L_m \left( \frac{N_p}{N_s} v_{sq} - r_s' i_{sq}' \right)}{(L_{ls}' + L_m)(L_{lp} + L_m) - L_m^2} - \omega_e i_{pd}' \quad (3.71)$$

$$p i_{pd}' = \frac{(L_{ls}' + L_m)(v_{acd} - r_p i_{pd}') - L_m \left( \frac{N_p}{N_s} v_{sd} - r_s' i_{sd}' \right)}{(L_{ls}' + L_m)(L_{lp} + L_m) - L_m^2} + \omega_e i_{pq}' \quad (3.72)$$

$$p i_{sq}' = \frac{(L_{lp} + L_m) \left( \frac{N_p}{N_s} v_{sq} - r_s' i_{sq}' \right) - L_m (v_{pq} - r_p i_{pq}')}{(L_{ls}' + L_m)(L_{lp} + L_m) - L_m^2} - \omega_e i_{sd}' \quad (3.73)$$

$$p i_{sd}' = \frac{(L_{lp} + L_m) \left( \frac{N_p}{N_s} v_{sd} - r_s' i_{sd}' \right) - L_m (v_{pd} - r_p i_{pd}')}{(L_{ls}' + L_m)(L_{lp} + L_m) - L_m^2} + \omega_e i_{sq}' \quad (3.74)$$

$$p v_{sq}' = \frac{1}{C_s} \left( -\frac{N_p}{N_s} i_{sq}' - i_{Lsq} \right) - \omega_e v_{sd} \quad (3.75)$$

$$p v_{sd}' = \frac{1}{C_s} \left( -\frac{N_p}{N_s} i_{sd}' - i_{Lsd} \right) + \omega_e v_{sq} \quad (3.76)$$

$$p i_{Lsq}' = \frac{1}{L_s} \left[ v_{sq} - \left( \frac{y v_{Cld}}{i_{Ls,base}} + r_{Ls} \right) i_{Lsq} \right] - \omega_e i_{Lsd} \quad (3.77)$$

$$p i_{Lsd}' = \frac{1}{L_s} \left[ v_{sd} - \left( \frac{y v_{Cld}}{i_{Ls,base}} + r_{Ls} \right) i_{Lsd} \right] + \omega_e i_{Lsq} \quad (3.78)$$

Combining above equations, the approximate average-value  $qd$  model for the load fixture is established. Note that (3.65), (3.66), (3.77) and (3.78) includes multiplication of states, thus the result model is nonlinear. On the other hand, the anti-windup and the limitation of the H-bridge

duty cycle shown in the control diagram in Figure 3.6 should also be included in the average-value  $qd$  model for time-domain simulation.

### 3.3.3 Fixture-only simulation

For validation, the AVQDM waveforms of the case study in Section 2.2 are plotted in Figure 3.7. The fixture is assumed to be connected to an ideal current source, and the transformer model modification for current source can be referred to Subsection 3.2.2. In this case study, the solver used is variable-step ODE 23 (Bogacki-Shampine), which greatly decrease the runtime of the model comparing the WLM. As shown in Figure 3.7, the steady-state waveforms of the AC quantities  $i_p$ ,  $v_p$ ,  $i_{Ls}$ , and  $v_r$  appear as different constants in different steady state conditions, as the duty cycle of the LED decreases from 50% to 20%. The reconstructed actual waveforms are compared to the waveform-level modeling result in Figure 3.8. It can be seen from the output current  $i_{Lld}$  waveforms that the high-frequency current ripple is neglected in the AVQDM. The other AC signals predicted by this model are almost identical to those predicted using WLM.

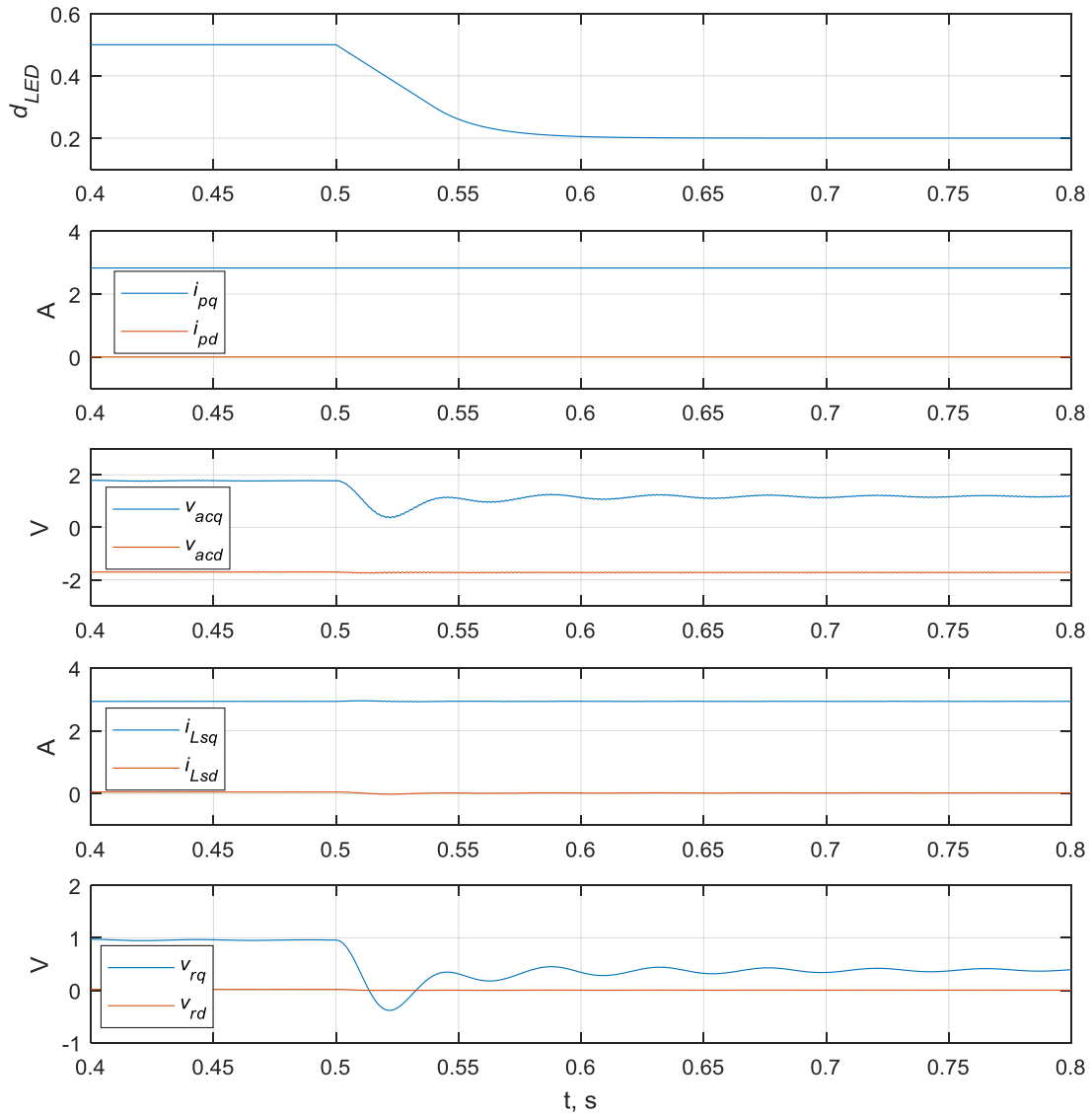


Figure 3.7 Fixture AVQDM waveforms

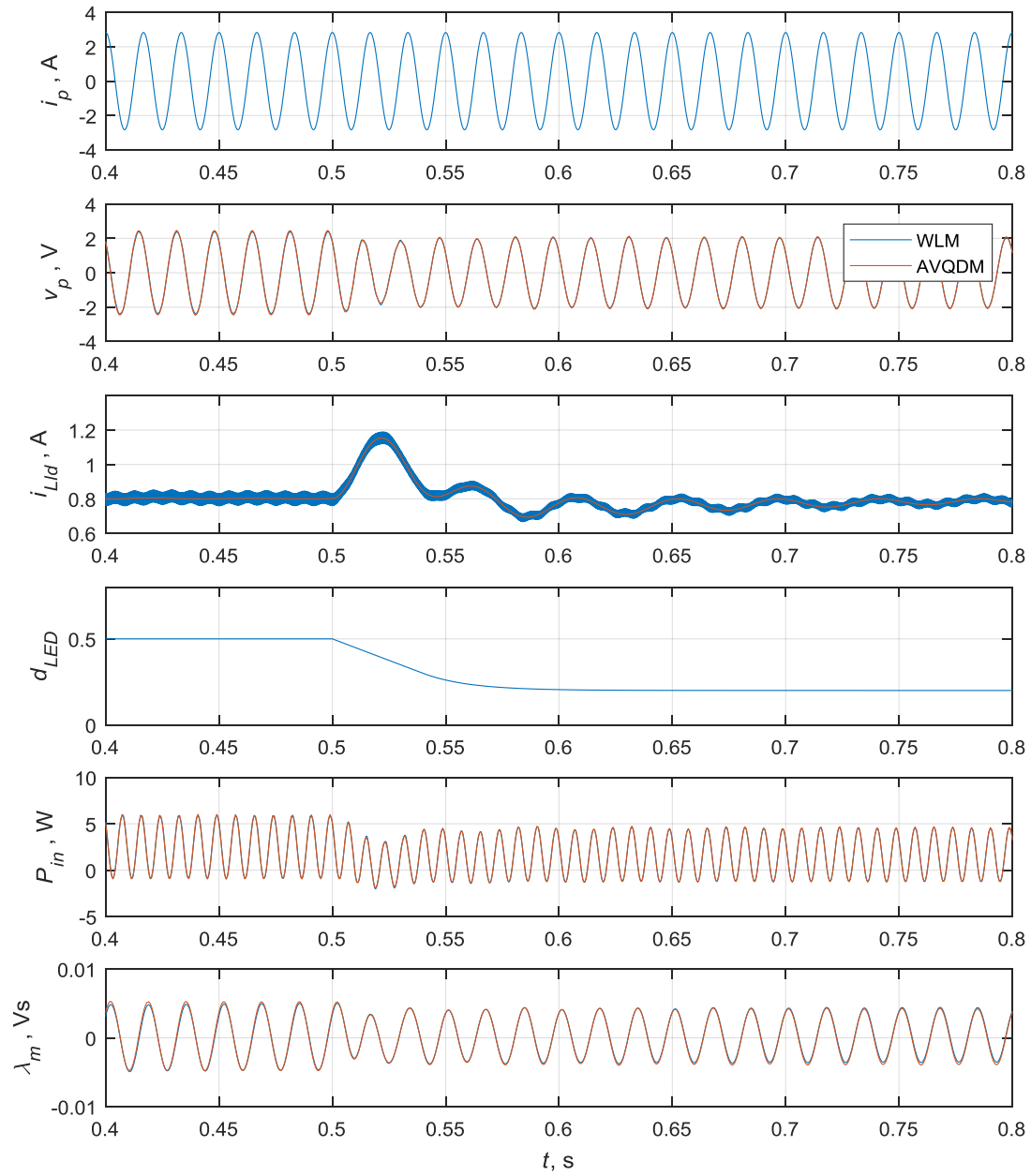


Figure 3.8 Fixture waveforms comparison

### 3.4 System Average-value Simulation

By combining the source and the fixture, the system AVQDM is established. By assigning the same parameter sets as in Section 2.3, the waveforms of WLM and AVQDM can be compared. Instead of using fixed-step ODE45 with  $1\mu\text{s}$  step size to incorporate the fast-switching of converters, the AVQDM can use variable-step ODE23 (Bogacki-Shampine), which greatly decreases the runtime.

Corresponding to the results in Figure 2.18 and 2.19, the new results are depicted in Figure 3.9 and 3.10. As can be seen, when the system is stable, the proposed AVQDM accurately reproduces the waveforms of  $i_{ac}$ , the transmission line current,  $v_p$ , the voltage across each fixture, and  $\lambda_m$ , the magnetizing flux linkage of the fixture isolation transformers. The primary dynamics of the LED load current  $i_{LLd}$  is also well preserved. When the instability occurs, errors between the WLM and AVQDM waveforms can be seen. However, from a design prospective, having the errors is acceptable for the reason that the system instability should be avoided; never the less, the proposed AVQDM predicts the point where the instability of the system waveform-value model occurs. In next chapter, starting from the AVQDM, the small-signal stability analysis with certain operating point will be performed and for the same cases, its predictions will be compared to those of the WLM.

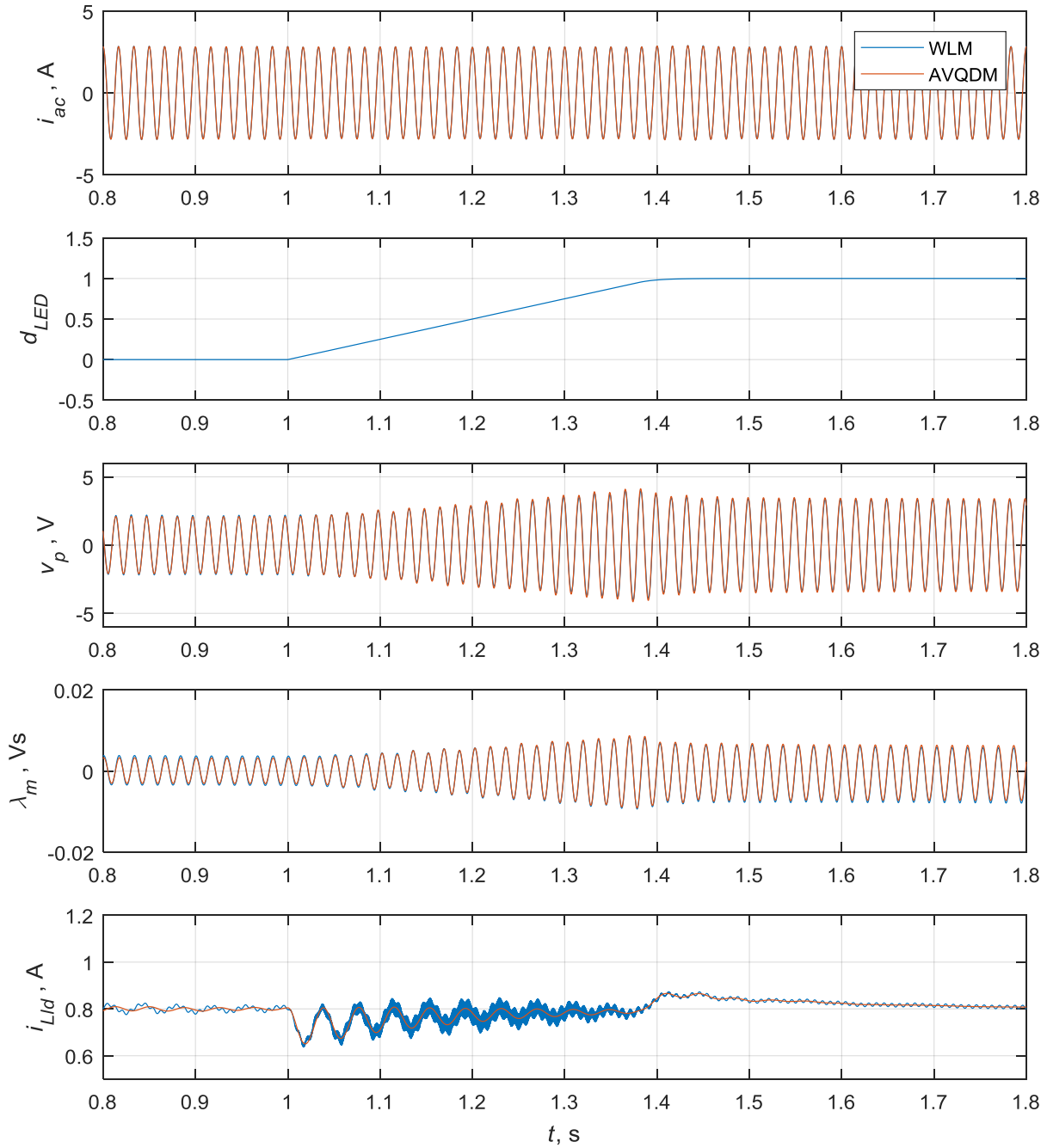


Figure 3.9 Case 1 System simulation result comparison

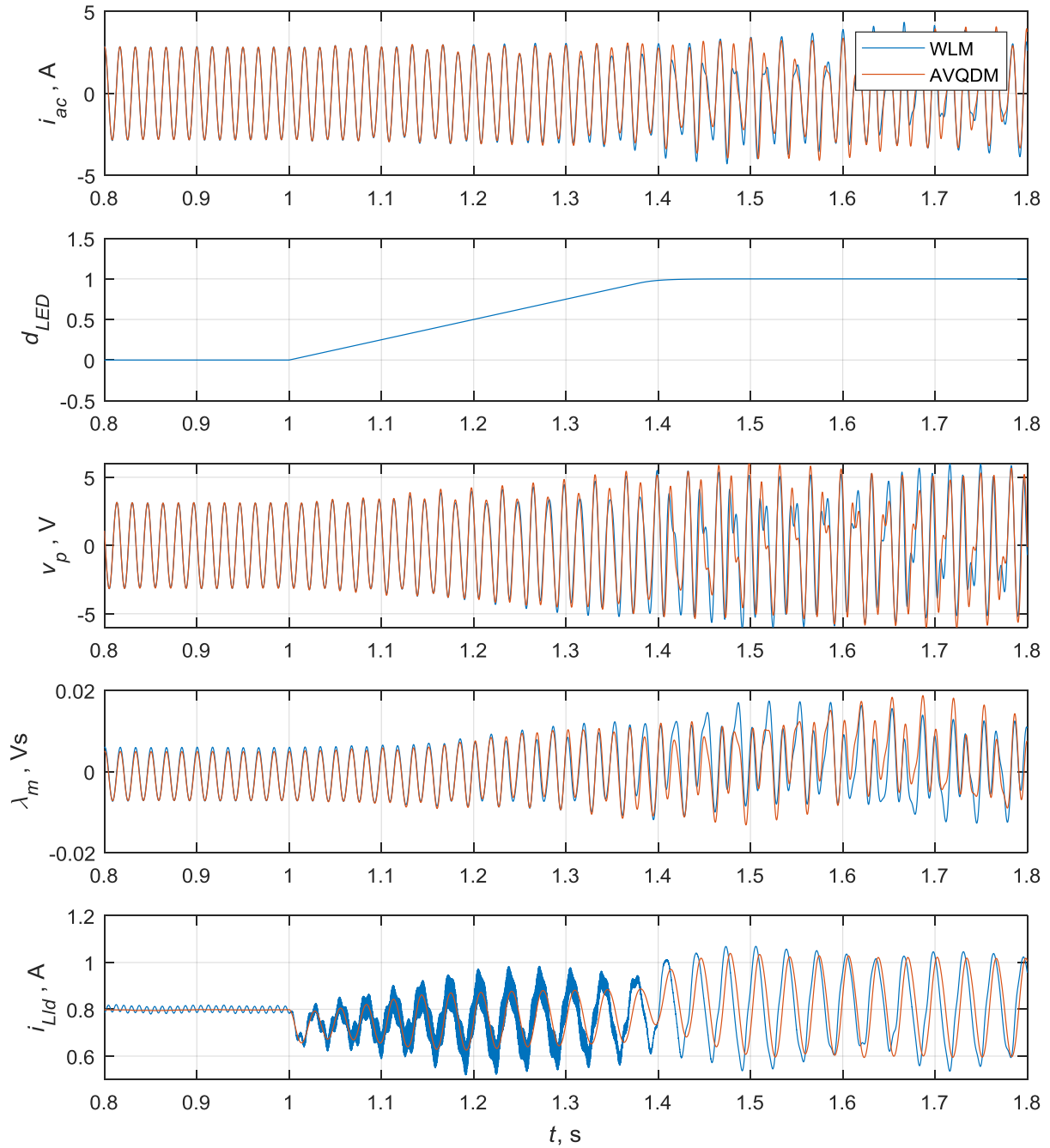


Figure 3.10 Case 2 System simulation result comparison

## 4. STABILITY ANALYSIS

The Nyquist stability criterion is a widely used technique for determining the stability of a dynamical system. This technique is also frequently used in power system studies including DC systems [54], three-phase AC systems [42, 55], grid-connected inverters [56] and many others. To address the small-signal analysis for the single-phase ac series system introduced in previous chapters, the generalized Nyquist stability criterion for MIMO (multiple-input multiple-output) systems can be utilized. To this end, first the state space models of system components (the source and the fixtures) are linearized to create a LTI (linear time-invariant) MIMO system models; then the models are converted to frequency-domain transfer functions, and accordingly a system transfer function can be obtained; finally, system stability can be decided using the generalized Nyquist criterion using the eigenvalues of the system transfer function.

In this chapter, first the stability analysis of a DC system is introduced as an example of a SISO (single-input single-output) system. In Section 4.2, a generalized Nyquist theorem for MIMO system is introduced, and its implementation to the single-phase AC system average-value *qd* model (AVQDM) is illustrated. In Section 4.3, the conversion from the time-domain AVQDM to a frequency-domain model is set forth. Finally, the Nyquist stability criterion is reviewed and utilized to predict stability of this single-phase ac series system for the two cases provided in Chapter 2 and 3.

### 4.1 Reference Frame Transformation

Consider the model of a dc system shown in Figure 4.1. The system consists a source with Thevenin supply voltage  $v_{sT}$  and small-signal (incremental) impedance  $Z_s$ , a load with nominal load current  $i_{IN}$  and small-signal admittance  $Y_l$ . The system output, the voltage across the load can be expressed by

$$v = \frac{v_{sT} - Z_s i_{IN}}{1 + Z_s Y_l} \quad (4.1)$$

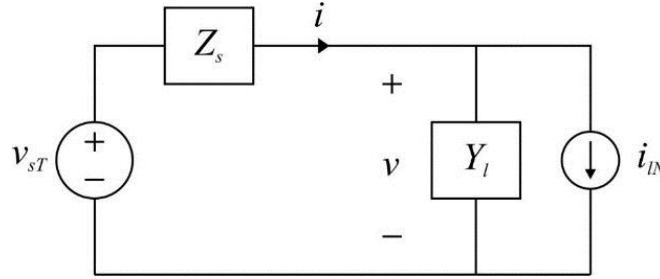


Figure 4.1 Equivalent circuit of dc system

This DC system can be regarded as a SISO LTI system with the input  $v_{sT} - Z_s i_{IN}$ , output  $v$ , and transfer function  $h(s) = (1 + Z_s Y_l)^{-1}$ .

If the system can be realized by the state model  $\{\mathbf{A}, \mathbf{B}, \mathbf{C}, \mathbf{D}\}$ , the transfer function can also be written as

$$h(s) = \mathbf{C}[s\mathbf{I} - \mathbf{A}]^{-1} \mathbf{B} \quad (4.2)$$

In order to provide a general framework for stability analysis for such systems, the definition of bounded-input bounded-output (BIBO) and bounded-input bounded-state (BIBS) stability are stated below [42].

**Definition:** A system is BIBO stable if, for each admissible bounded input  $\mathbf{u}(t)$  (i.e.  $\|\mathbf{u}(t)\|_\infty < \infty$ ) the response  $\mathbf{y}(t)$  is bounded. Here  $\mathbf{u}(t)$  is an  $n$ -by-one vector-valued function,  $\mathbf{y}(t)$  is an  $m$ -by-one vector-valued function,  $\|\mathbf{u}(t)\|_\infty = \max_i \|u_i(t)\|_\infty$ , and  $\|u_i(t)\|_\infty = \sup_i |u_i(t)|$ .

**Definition:** A system with state model  $\{\mathbf{A}, \mathbf{B}, \mathbf{C}, \mathbf{D}\}$  having arbitrary initial conditions is BIBS stable if for any bounded input  $\mathbf{u}(t)$ , the state response

$$\mathbf{x}(t) = e^{\mathbf{A}t} \mathbf{x}(0) + \int_0^t e^{\mathbf{A}(t-\tau)} \mathbf{B} \mathbf{u}(\tau) d\tau \quad (4.3)$$

is bounded.

These definitions are valid for MIMO systems as well as SISO systems. BIBS stability of a system is a sufficient but not necessary condition of BIBO stability. If a system is BIBO stable and all its states are controllable and observable, the system is BIBS stable.

Returning to the discussion of the dc system, for the system transfer function in (4.3), the system is BIBO stable if and only if all the poles of  $h(s)$  are in the Open Left Hand Plane (OLHP). Equivalently, the system is BIBO stable if all the zeros of the denominator  $1 + Z_s Y_l$  are in the OLHP. This can be verified by Nyquist stability criterion:  $1 + Z_s Y_l$  will have all zeros in the OLHP

if the number of counter-clockwise encirclements around  $(-1 + j0)$  of the Nyquist plot of  $Z_s Y_l$  is equal to the number of RHP poles of  $Z_s Y_l$ . The gain margin of the ‘stable’ case of the Nyquist contour represents the number of the identical load that could be connected in parallel to the source without causing instability.

The Nyquist stability criterion guarantees that the output of the system is stable. However, it does not ensure all states in the system to be stable. By the definition of BIBS stability, it can be shown that a system is BIBS stable if all the eigenvalues of the system matrix  $\mathbf{A}$  are in the LHP and, if there is an eigenvalue on the imaginary axis, it may not be repeated and it has to be uncontrollable [57]. It can also be shown that the eigenvalues of  $\mathbf{A}$  are the poles of  $h(s)$  from (4.4) if the system realization  $\{\mathbf{A}, \mathbf{B}, \mathbf{C}, \mathbf{D}\}$  is controllable and observable (i.e., minimal [58]); in this case, the Nyquist stability ensures that the system is BIBS stable.

## 4.2 Generalized Nyquist Criterion and Its Application

### 4.2.1 Introduction

In the 1970s, MacFarlane and Postlethwaite [59] extended the stability theory of Nyquist to a generalized Nyquist stability criterion which addresses matrix transfer functions for multiple-input multiple-output (MIMO) systems. The generalized Nyquist Theorem may be stated as follows with the illustration of Figure 4.2. The full mathematical proof of the generalized Nyquist criterion is given in [59] and a short derivation is provided in [42].

**Theorem**[59]: Let the MIMO system in Figure 4.2 have no open-loop uncontrollable or unobservable modes whose corresponding characteristic frequencies lie in the right-half plane. Then this system will be closed-loop stable if and only if the sum of counter-clockwise encirclements around the critical point  $(-1 + j0)$  by the set of characteristic contours of the return ratio  $\mathbf{L}(s) = \mathbf{G}(s)\mathbf{K}(s)$  is equal to the total number of right-half plane poles of  $\mathbf{G}(s)$  and  $\mathbf{K}(s)$ .

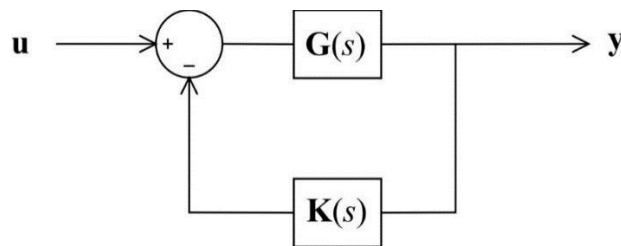


Figure 4.2 MIMO system

The characteristic contours are the Nyquist contour responses of the eigenvalues (which are also  $s$ -domain functions) of the return ratio  $\mathbf{L}(s)$ . The Nyquist contour starts from  $(0 + j0)$  on the complex plane, moves up to  $(0 + j\infty)$ , follows a semicircle in the clockwise direction to  $(0 - j\infty)$ , and finally moves up back to  $(0 + j0)$ . Substituting the complex number  $s$  for every point in this contour to the return ratio  $\mathbf{L}(s)$  yields  $n$  eigenvalues, where  $n$  is the size of output vector  $\mathbf{y}$ ; each eigenvalue following the Nyquist contour generates a characteristic contour, and there are  $n$  characteristic contours.

#### 4.2.2 Implementation of the generalized Nyquist criterion

In this research, for the single-phase series ac system, the entire circuit including the source, the fixtures and transmission line components can be considered as a lumped system similar to a DC system, but in terms of  $qd$  variables. Namely, the system consists of a current source nominal current  $\mathbf{i}_{qdsN}$ , a source admittance  $\mathbf{Y}_{qds}$ , a load with Thevenin voltage  $\mathbf{v}_{qdlT}$  and load impedance  $\mathbf{Z}_{qdl}$  as shown in Figure 4.3. Based on the average-value  $qd$  model developed in Chapter 3,  $\mathbf{i}_{qdsN}$  and  $\mathbf{v}_{qdlT}$  are vectors with  $q$ - and  $d$ - variables, and  $\mathbf{Y}_{qds}$  and  $\mathbf{Z}_{qdl}$  are two-by-two matrices of  $s$ -domain transfer functions. The source transfer function can be expressed as

$$\mathbf{i}_{qdac} = \mathbf{i}_{qdsN} - \mathbf{Y}_{qds} \mathbf{v}_{qdac} = \left[ \mathbf{C}_{qds} (s\mathbf{I} - \mathbf{A}_{qds})^{-1} \mathbf{B}_{qds} + \mathbf{D}_{qds} \right] \begin{bmatrix} \mathbf{v}_{qdac} \\ \mathbf{i}_{qd0} \end{bmatrix} \quad (4.4)$$

where  $\mathbf{A}_{qds}$ ,  $\mathbf{B}_{qds}$ , and  $\mathbf{C}_{qds}$  are the source state space realization which can be obtained from (3.49), (3.50) and (3.51), and  $\mathbf{D}_{qds} = \mathbf{0}$ . The constant  $\mathbf{i}_{qd0}$  is the desired ac current with  $\mathbf{i}_{qd0} = [i_{acq}^* \ i_{acd}^*]^T$ . The source admittance matrix  $\mathbf{Y}_{qds}$  is the left-most two-by-two submatrix of the negative source transfer function  $-\mathbf{C}_{qds}(s\mathbf{I} - \mathbf{A}_{qds})^{-1}\mathbf{B}_{qds}$ .

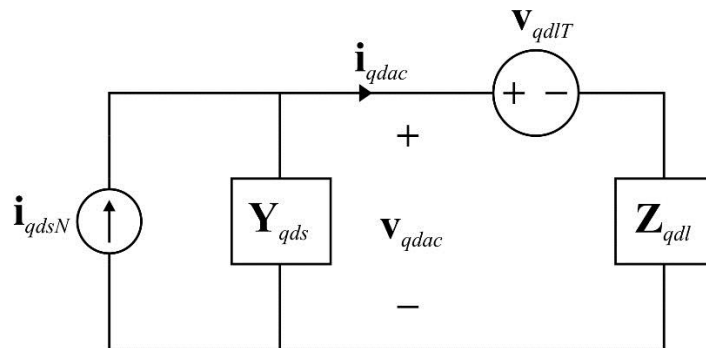


Figure 4.3 Lumped system circuit

Similarly, the fixture transfer function can be written as

$$\mathbf{v}_{qdac} = \mathbf{v}_{qdlT} + \mathbf{Z}_{qdl} \mathbf{i}_{qdac} = \left[ \mathbf{C}_{qdf} (s\mathbf{I} - \mathbf{A}_{qdf})^{-1} \mathbf{B}_{qdf} + \mathbf{D}_{qdf} \right] \begin{bmatrix} \mathbf{i}_{qdac} \\ \mathbf{v}_{qd0} \end{bmatrix} \quad (4.5)$$

where  $\mathbf{A}_{qdf}$ ,  $\mathbf{B}_{qdf}$ ,  $\mathbf{C}_{qdf}$ , and  $\mathbf{D}_{qdf}$  can be obtained by linearizing the state space transient functions (3.71-3.78), which will be discussed in next subsection. The operating point  $\mathbf{v}_{qd0}$  includes the nominal values of the DC part, and in particular  $\mathbf{v}_{qd0} = [i_{Lld}^* \ v_{Clld0} \ y_0 \ v_{ld0}]^T$ . The load impedance matrix  $\mathbf{Z}_{qdl}$  can be found as the left-most two-by-two submatrix of the fixture transfer function  $\mathbf{C}_{qdf}(s\mathbf{I} - \mathbf{A}_{qdf})^{-1}\mathbf{B}_{qdf} + \mathbf{D}_{qdf}$ .

Combining (4.4) and (4.5) yields the system transfer function similar to (4.1) as

$$\mathbf{i}_{qdac} = \left[ \mathbf{I} + \mathbf{Y}_{qds} \mathbf{Z}_{qdl} \right]^{-1} \left[ \mathbf{i}_{qdsN} - \mathbf{Y}_{qds} \mathbf{v}_{qdlT} \right] \quad (4.6)$$

Applying the generalized Nyquist criterion to the system, the following statement can be concluded:

Let the MIMO system in Figure 4.4 have no open-loop uncontrollable or unobservable modes whose corresponding characteristic frequencies lie in the right-half plane. Then this system will be closed-loop stable if and only if the sum of counter-clockwise encirclements around the critical point  $(-1 + j0)$  by the set of characteristic contours of the return ratio  $\mathbf{L}_{qd}(s) = -\mathbf{Y}_{qds}\mathbf{Z}_{qdl}$  is equal to the total number is right-half plane poles of  $\mathbf{Y}_{qds}$  and  $\mathbf{Z}_{qdl}$ .

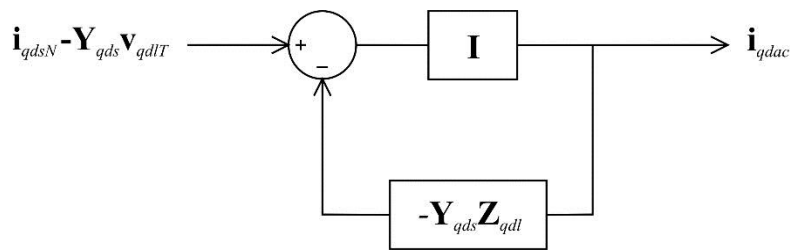


Figure 4.4 MIMO equivalent system of the single-phase ac system

From a practical prospective, both the source and the load fixtures are designed to be stable: the source is designed to output a constant amplitude sinusoidal current, when supplying a fixed sinusoidal voltage load; the fixture is designed to be BIBS stable when supplied by an ideal constant current source. Therefore, neither  $\mathbf{Y}_{qds}$  nor  $\mathbf{Z}_{qdl}$  introduces any RHP poles. The characteristic contours are the contours of the eigenvalues of  $\mathbf{L}_{qd}(s)$  for  $s$  along the Nyquist path. Therefore, the stability criterion of the single-phase AC system becomes:

The system shown in Figure 4.4 is closed-loop stable if and only if the contours of eigenvalues of  $\mathbf{L}_{qd}(s) = -\mathbf{Y}_{qds}\mathbf{Z}_{qdl}$  going through the Nyquist path do not encircle the critical point  $(-1 + j0)$ .

For the system consisted of one source and identical load fixtures with the load impedance  $\mathbf{Z}_{qdl}$ , the gain margin of the characteristic contours of  $\mathbf{L}_{qd}(s) = -\mathbf{Y}_{qds}\mathbf{Z}_{qdl}$  predicts the maximum  $N_f$  for maintaining system stability. In particular, the system with  $N_f$  identical load fixtures is stable if and only if the contours of eigenvalues of  $-N_f\mathbf{Y}_{qds}\mathbf{Z}_{qdl}$  going through the Nyquist path do not encircle the critical point  $(-1 + j0)$ .

### 4.3 Stability Analysis Using The Average-Value $Qd$ Models

Based on (4.4) and (4.5), in order to develop a system stability criteria for the single-phase series ac system, the source state space realization  $\{\mathbf{A}_{qds}, \mathbf{B}_{qds}, \mathbf{C}_{qds}, \mathbf{D}_{qds}\}$  and the linearized fixture realization  $\{\mathbf{A}_{qdf}, \mathbf{B}_{qdf}, \mathbf{C}_{qdf}, \mathbf{D}_{qdf}\}$  are needed. The system model is modified as shown in Figure 4.5. As can be seen the transmission line inductance and resistance have been added to the source and fictitious resistance  $r_i$  has been introduced across the primary winding of the fixture isolation transformer. Thus, the source model becomes voltage-in current-out and the fixture model becomes current-in voltage-out. As the resistance value of  $r_i$  is very large, these modifications have almost no impact on the system performance.

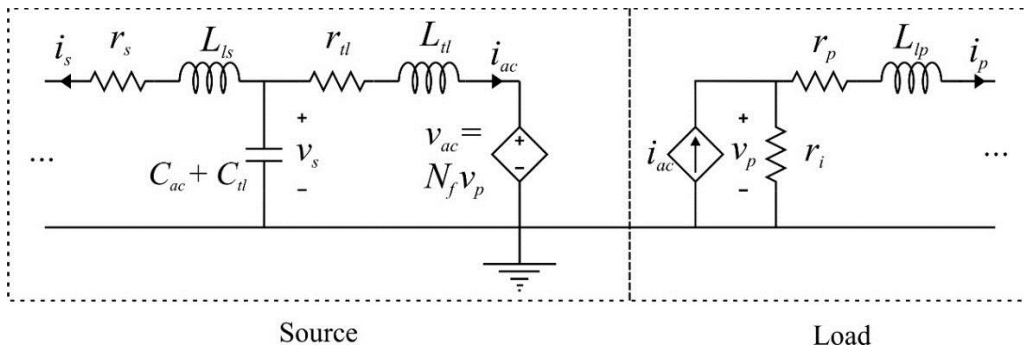


Figure 4.5 Modified system model for stability analysis

To use this new system structure to derive the system frequency-domain model, the average-value  $qd$  state space model of the source in (3.45), (3.46) and (3.49) should be modified. The new single-phase state vector (not  $qd$ ) is set to

$$\mathbf{x}_{ss} = [i_{ac} \quad v_s \quad i_s \quad x_{c1} \quad x_{c2} \quad x_{c3}]^T \quad (4.7)$$

and the input becomes  $\mathbf{u}_{ss} = [v_{ac} \quad i_{ac}^*]^T$ . Accordingly, the single-phase state space realization can be

shown as

$$\mathbf{A}_{ss} = \begin{bmatrix} -\frac{r_{tl}}{L_{tl}} & -\frac{1}{L_{tl}} & 0 & 0 & 0 & 0 \\ -\frac{1}{C_s} & 0 & -\frac{1}{C_s} & 0 & 0 & 0 \\ \frac{L'_m k_p \tau_p^{-1}}{L'_{ls} + L'_m} & \frac{1}{L'_{ls} + L'_m} & -\frac{r_s}{L'_{ls} + L'_m} & -\frac{L'_m}{L'_{ls} + L'_m} (k_i \omega_e^2 - k_p \tau_p^{-2}) & -\frac{L'_m}{L'_{ls} + L'_m} k_i \tau_p^{-1} \omega_e^2 & \frac{L'_m}{L'_{ls} + L'_m} k_p \tau_p^{-2} \omega_e^2 \\ -1 & 0 & 0 & -\tau_p^{-1} & -\omega_e^2 & -\omega_e^2 \tau_p^{-1} \\ 0 & 0 & 0 & 1 & 0 & 0 \\ 0 & 0 & 0 & 0 & 1 & 0 \end{bmatrix} \quad (4.8)$$

$$\mathbf{B}_{ss} = \begin{bmatrix} \frac{1}{L_{tl} + L_{tl}} & 0 \\ 0 & 0 \\ 0 & -\frac{L'_m k_p \tau_p^{-1}}{L'_{ls} + L'_m} \\ 0 & 1 \\ 0 & 0 \\ 0 & 0 \end{bmatrix} \quad (4.9)$$

Converting  $\mathbf{A}_{ss}$  and  $\mathbf{B}_{ss}$  to the average-value  $qd$  form and rearranging the order of inputs and outputs yields

$$\mathbf{A}_{qds} = \begin{bmatrix} \mathbf{A}_{ss} & -\omega_e \mathbf{I}_6 \\ \omega_e \mathbf{I}_6 & \mathbf{A}_{ss} \end{bmatrix} \quad (4.10)$$

$$\mathbf{B}_{qds} = \begin{bmatrix} \mathbf{B}_{ss} & 0 \\ 0 & \mathbf{B}_{ss} \end{bmatrix} \begin{bmatrix} 1 & 0 & 0 & 0 \\ 0 & 0 & 1 & 0 \\ 0 & 1 & 0 & 0 \\ 0 & 0 & 0 & 1 \end{bmatrix} \quad (4.11)$$

$$\mathbf{C}_{qds} = \begin{bmatrix} 1 & 0 & 0 & 0 & 0 & 0 & 0 & 0 & 0 & 0 & 0 & 0 \\ 0 & 0 & 0 & 0 & 0 & 0 & 1 & 0 & 0 & 0 & 0 & 0 \end{bmatrix} \quad (4.12)$$

$$\mathbf{D}_{qds} = \mathbf{0} \quad (4.13)$$

The source admittance  $\mathbf{Y}_{qds}$  can therefore be found as the left-most two-by-two submatrix of  $-\mathbf{C}_{qds} [s\mathbf{I} - \mathbf{A}_{qds}]^{-1} \mathbf{B}_{qds}$ .

Now consider the nonlinear fixture model as introduced in subsection 3.3. To linearize a nonlinear ODE in the average-value  $qd$  models, the first-order Taylor expansion

$$f(\mathbf{x}) \approx f(\mathbf{x}_0) + (\mathbf{x} - \mathbf{x}_0) \nabla f^T \Big|_{\mathbf{x}=\mathbf{x}_0} \quad (4.14)$$

can be used. The linearized ODE (3.65) can be expressed as

$$pv_{Cld} = \frac{1}{C_{ld}} \left\{ \frac{1}{i_{Ls,base}} \left[ y_0 i_{Lsq0} (i_{Lsq} - i_{Lsq0}) + y_0 i_{Lsd0} (i_{Lsd} - i_{Lsd0}) + \frac{1}{2} (i_{Lsq0}^2 + i_{Lsd0}^2) y \right] - i_{Lld} \right\} \quad (4.15)$$

where

$$y = k_i I + k_p (i_{Lld}^* - i_{Lld}) \quad (4.16)$$

In (4.15),  $y_0$ ,  $i_{Lsq0}$ , and  $i_{Lsd0}$  are operational points of  $y$ ,  $i_{Lsq}$  and  $i_{Lsd}$ , respectively. Similarly, the linearized LED voltage can be expressed be approximated by

$$v_{ld} = d_{LED} v_{LED} = d_{LED} \left[ v_{LED0} + r_{LED} (i_{Lld} - i_{Lld}^*) \right] = v_{ld0} + d_{LED} r_{LED} i_{Lld} - d_{LED} r_{LED} i_{Lld}^* \quad (4.17)$$

where  $v_{LED0}$  is the operating point of the LED voltage. The nominal load voltage is noted as  $v_{ld0}$  ( $= d_{LED} v_{LED0}$ ), which is regarded as an input variable. The incremental resistance  $r_{LED}$  can be found to be the slope of the V-I curve as shown in Figure 2.12 at this operating point. Therefore, (3.64) can be linearized as

$$pi_{Lld} = \frac{1}{L_{ld}} \left[ v_{Cld} - (r_{Lld} + d_{LED} r_{LED}) i_{Lld} - v_{LED0} + d_{LED} r_{LED} i_{Lld}^* \right] \quad (4.18)$$

Moreover, (3.77) and (3.78) can be linearized as

$$pi_{Lsq} = \frac{1}{L_s} \left[ v_{sq} - \left( \frac{y_0 v_{Cld0}}{i_{Ls,base}} + r_{Ls} \right) i_{Lsq} - \frac{i_{Lsq0} v_{Cld0}}{i_{Ls,base}} y - \frac{y_0 i_{Lsq0}}{i_{Ls,base}} v_{Cld} + y_0 i_{Lsq0} v_{Cld0} \right] - \omega_e i_{Lsd} \quad (4.19)$$

$$pi_{Lsd} = \frac{1}{L_s} \left[ v_{sq} - \left( \frac{y_0 v_{Cld0}}{i_{Ls,base}} + r_{Ls} \right) i_{Lsd} - \frac{i_{Lsd0} v_{Cld0}}{i_{Ls,base}} y - \frac{y_0 i_{Lsd0}}{i_{Ls,base}} v_{Cld} + y_0 i_{Lsd0} v_{Cld0} \right] + \omega_e i_{Lsq} \quad (4.20)$$

Considering the modified system model in Figure 4.5, the voltage across each fixture can be obtained by

$$v_p = r_i (i_{ac} - i_p) \quad (4.21)$$

Combining the above equations, the linearized state space model of the fixture becomes

$$\mathbf{x}_{qdf} = \left[ i_{pq} \quad i_{pd} \quad i'_{sq} \quad i'_{sd} \quad v_{sq} \quad v_{sd} \quad i_{Lsq} \quad i_{Lsd} \quad v_{Cld} \quad i_{Lld} \quad I \right]^T \quad (4.22)$$

$$\mathbf{u}_{qdf} = \left[ i_{acq} \quad i_{acd} \quad i_{Lld}^* \quad v_{Cld0} \quad y_0 \quad v_{ld0} \right]^T \quad (4.23)$$

$$\mathbf{A}_{qdf} = \begin{bmatrix}
-\frac{(L_m + L_s)(r_p + r_i)}{D} & -\omega_e & \frac{L_m r_s'}{D} & 0 & -\frac{L_m TR}{D} & 0 \\
\omega_e & -\frac{(L_m + L_s)(r_p + r_i)}{D} & 0 & \frac{L_m r_s'}{D} & 0 & -\frac{L_m TR}{D} \\
\frac{L_m(r_p + r_i)}{D} & 0 & -\frac{(L_m + L_p)r_s'}{D} & -\omega_e & \frac{(L_m + L_p)TR}{D} & 0 \\
0 & \frac{L_m(r_p + r_i)}{D} & \omega_e & -\frac{(L_m + L_p)r_s'}{D} & 0 & \frac{(L_m + L_p)TR}{D} \\
0 & 0 & -\frac{TR}{C_s} & 0 & 0 & -\omega_e \quad \dots \\
0 & 0 & 0 & -\frac{TR}{C_s} & \omega_e & 0 \\
0 & 0 & 0 & 0 & \frac{1}{L_s} & 0 \\
0 & 0 & 0 & 0 & 0 & \frac{1}{L_s} \\
\mathbf{0} & & & & & \\
\mathbf{0} & & & & & \\
-\frac{1}{C_s} & 0 & 0 & 0 & 0 & 0 \\
0 & -\frac{1}{C_s} & 0 & 0 & 0 & 0 \\
\dots - \frac{r_{Ls} + y_0 v_{Cld0}}{i_{Ls,base} L_s} & -\omega_e & -\frac{y_0 i_{Lsq0}}{i_{Ls,base} L_s} & \frac{v_{Cld0} i_{Lsq0} k_p}{i_{Ls,base} L_s} & -\frac{v_{Cld0} i_{Lsq0} k_i}{i_{Ls,base} L_s} \\
\omega_e & -\frac{r_{Ls} + y_0 v_{Cld0}}{i_{Ls,base} L_s} & -\frac{y_0 i_{Lsd0}}{i_{Ls,base} L_s} & \frac{v_{Cld0} i_{Lsd0} k_p}{i_{Ls,base} L_s} & -\frac{v_{Cld0} i_{Lsd0} k_i}{i_{Ls,base} L_s} \\
\frac{y_0 i_{Lsq0}}{i_{Ls,base} C_{ld}} & \frac{y_0 i_{Lsq0}}{i_{Ls,base} C_{ld}} & 0 & -\frac{y_0 k_p (i_{Lsq0}^2 + i_{Lsd0}^2)}{2i_{Ls,base} C_{ld}} - \frac{1}{C_{ld}} & \frac{y_0 k_i (i_{Lsq0}^2 + i_{Lsd0}^2)}{2i_{Ls,base} C_{ld}} \\
0 & 0 & \frac{1}{L_{ld}} & -\frac{d_{led} r_{led} + r_{Lld}}{L_{ld}} & 0 \\
0 & 0 & 0 & -1 & 0
\end{bmatrix}$$

(4.24)

$$\mathbf{B}_{qdf} = \begin{bmatrix} \frac{r_i(L'_{ls} + L_m)}{D} & 0 & 0 & 0 & 0 & 0 \\ 0 & \frac{r_i(L'_{ls} + L_m)}{D} & 0 & 0 & 0 & 0 \\ -\frac{r_i L_m}{D} & 0 & 0 & 0 & 0 & 0 \\ 0 & -\frac{r_i L_m}{D} & 0 & 0 & 0 & 0 \\ 0 & 0 & 0 & 0 & 0 & 0 \\ 0 & 0 & 0 & 0 & 0 & 0 \\ 0 & 0 & -\frac{v_{Cld0} i_{Lsq0} k_p}{L_s} & \frac{y_0 i_{Lsq0}}{L_s} & 0 & 0 \\ 0 & 0 & -\frac{v_{Cld0} i_{Lsd0} k_p}{L_s} & \frac{y_0 i_{Lsd0}}{L_s} & 0 & 0 \\ 0 & 0 & \frac{(i_{Lsq0}^2 + i_{Lsd0}^2) k_p}{2i_{Ls,base} C_{ld}} & 0 & -\frac{(i_{Lsq0}^2 + i_{Lsd0}^2)}{2i_{Ls,base} C_{ld}} & 0 \\ 0 & 0 & \frac{d_{led} r_{led}}{L_{ld}} & 0 & 0 & -\frac{1}{L_{ld}} \\ 0 & 0 & 1 & 0 & 0 & 0 \end{bmatrix} \quad (4.25)$$

$$\mathbf{C}_{qdf} = \begin{bmatrix} -r_i & 0 & 0 & 0 & 0 & 0 & 0 & 0 & 0 & 0 & 0 \\ 0 & -r_i & 0 & 0 & 0 & 0 & 0 & 0 & 0 & 0 & 0 \end{bmatrix} \quad (4.26)$$

$$\mathbf{D}_{qdf} = \begin{bmatrix} r_i & 0 & 0 & 0 & 0 & 0 \\ 0 & r_i & 0 & 0 & 0 & 0 \end{bmatrix} \quad (4.27)$$

where  $D = (L_m + L_{lp})(L_m + L'_{ls}) - Lm^2$ . The load small-signal impedance matrix can be found as the left-most two-by-two sub matrix of  $\mathbf{C}_{qdf}[s\mathbf{I} - \mathbf{A}_{qdf}]^{-1}\mathbf{B}_{qdf} + \mathbf{D}_{qdf}$ .

At this point the work necessary to carry out stability analysis is complete. To verify the prediction of system stability using this technique, the two sets of system parameters in Table 2.3 and 2.4 are implemented (the number of fixtures  $N_f = 50$  is also incorporated). There are two contours of eigenvalues as labeled. The Nyquist plots of two LED duty cycles (0 and 100%) in Case 1 are shown in Figure 4.6. The Nyquist plots of two LED duty cycles (0 and 50%) in Case 2 are shown in Figure 4.7. It can be shown that all the transfer functions of the source and the fixture models used in these case studies have no ORHP poles, so that the encirclements of the critical point should be zero. It can be seen that this method predicts a system instability in Case 2 for 50% LED duty cycle, due to an encirclement of the critical point. To further verify if the prediction of

this method agrees with the time-domain simulation, two more situations in Case 2 conditions are tested around the boundary that a contour crosses the critical point. It is expected to see that a contour that barely encircles the critical point corresponds to a barely unstable case, and a contour that barely not encircles the critical point corresponds to a barely stable case.

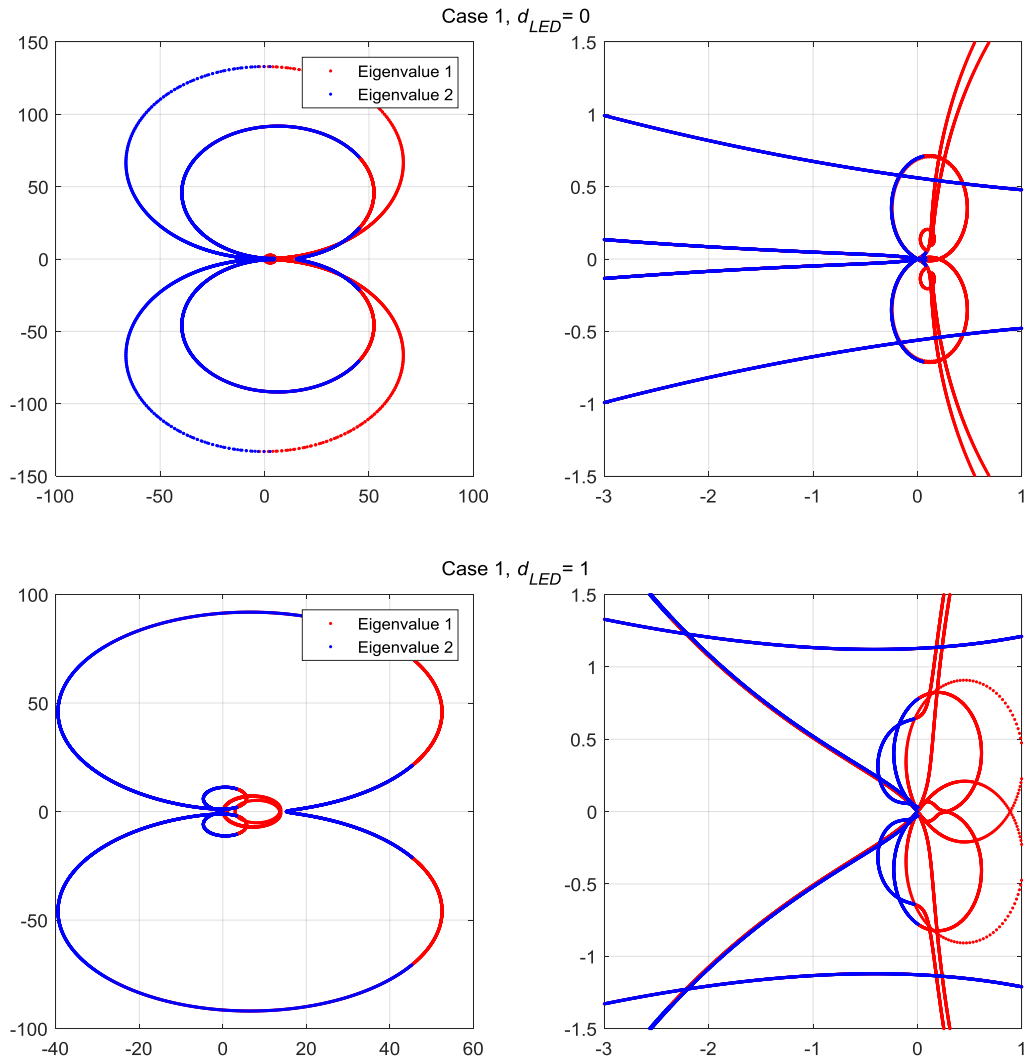


Figure 4.6 Nyquist plots of Case 1

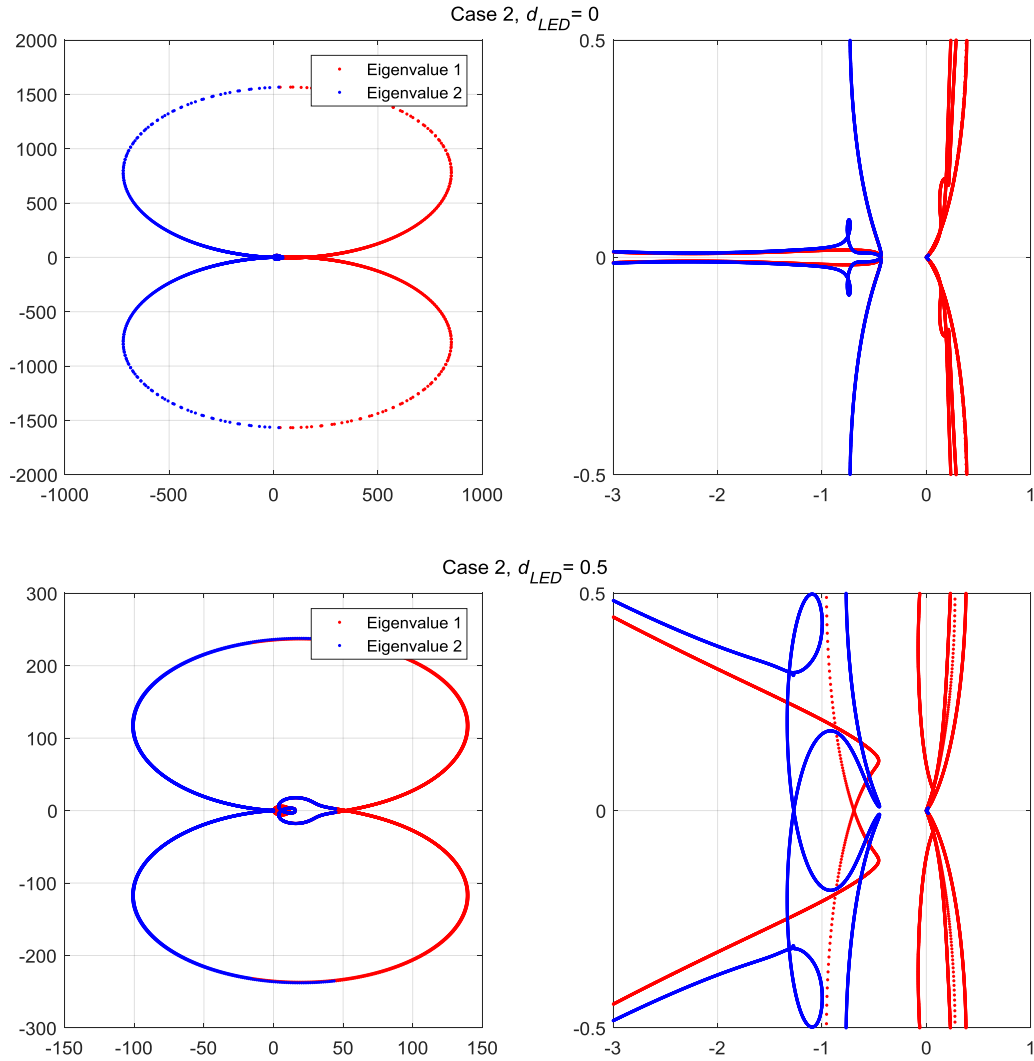


Figure 4.7 Nyquist plots of Case 2

Figure 4.8 shows a barely unstable situation for 13.5% LED duty cycle, from which an increasing oscillation can be seen in the WLM  $i_{LLd}$  waveform in time-domain. This oscillating component can also be seen in waveforms of other variables. Meanwhile, Figure 4.9 shows a barely stable case for 12% LED duty cycle for both the Nyquist plot and the WLM simulation. From these studies around the stability boundary, it can be concluded that the stability prediction made by Nyquist method agrees with the time-domain simulation for this case study.

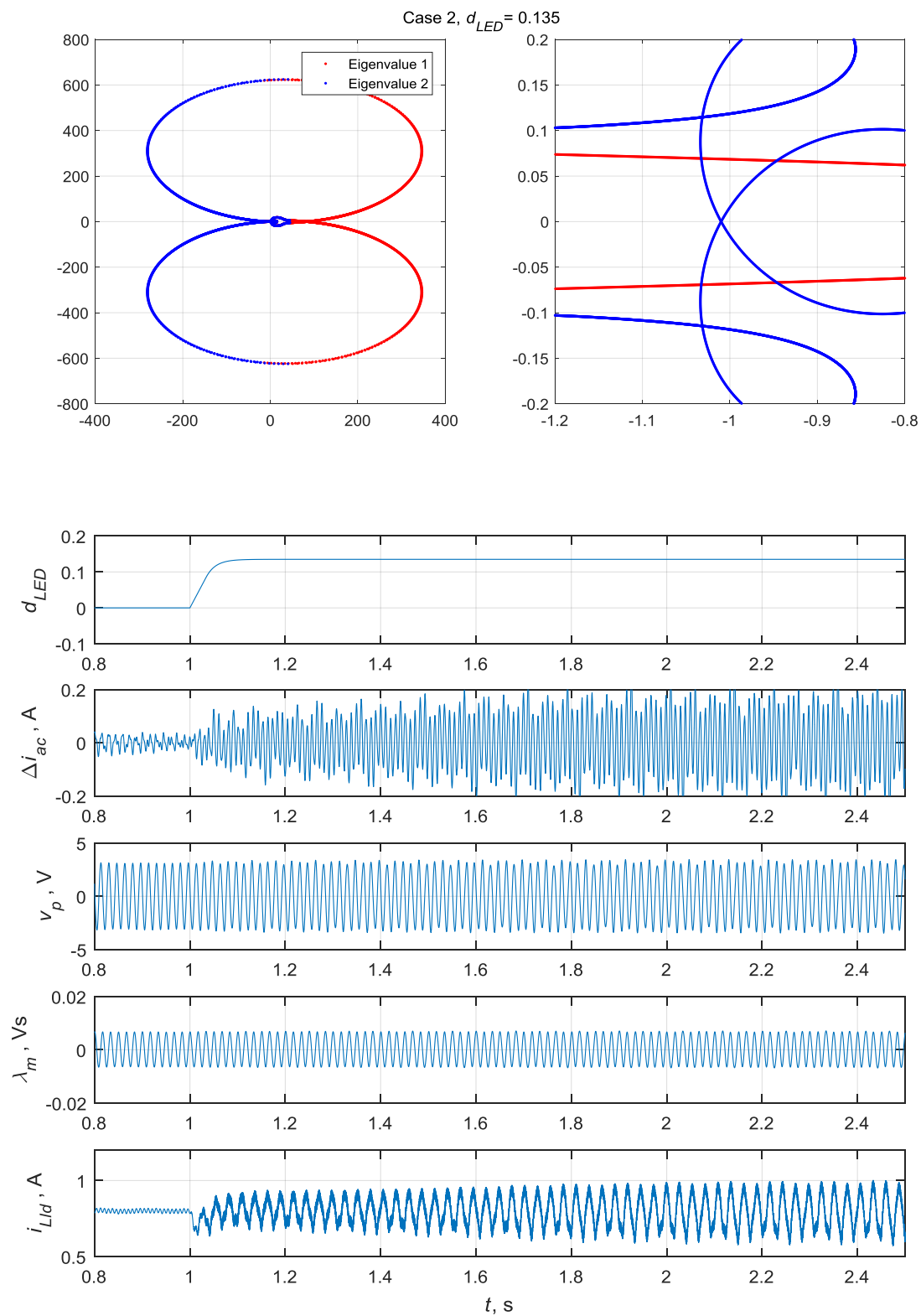


Figure 4.8 Barely unstable situation

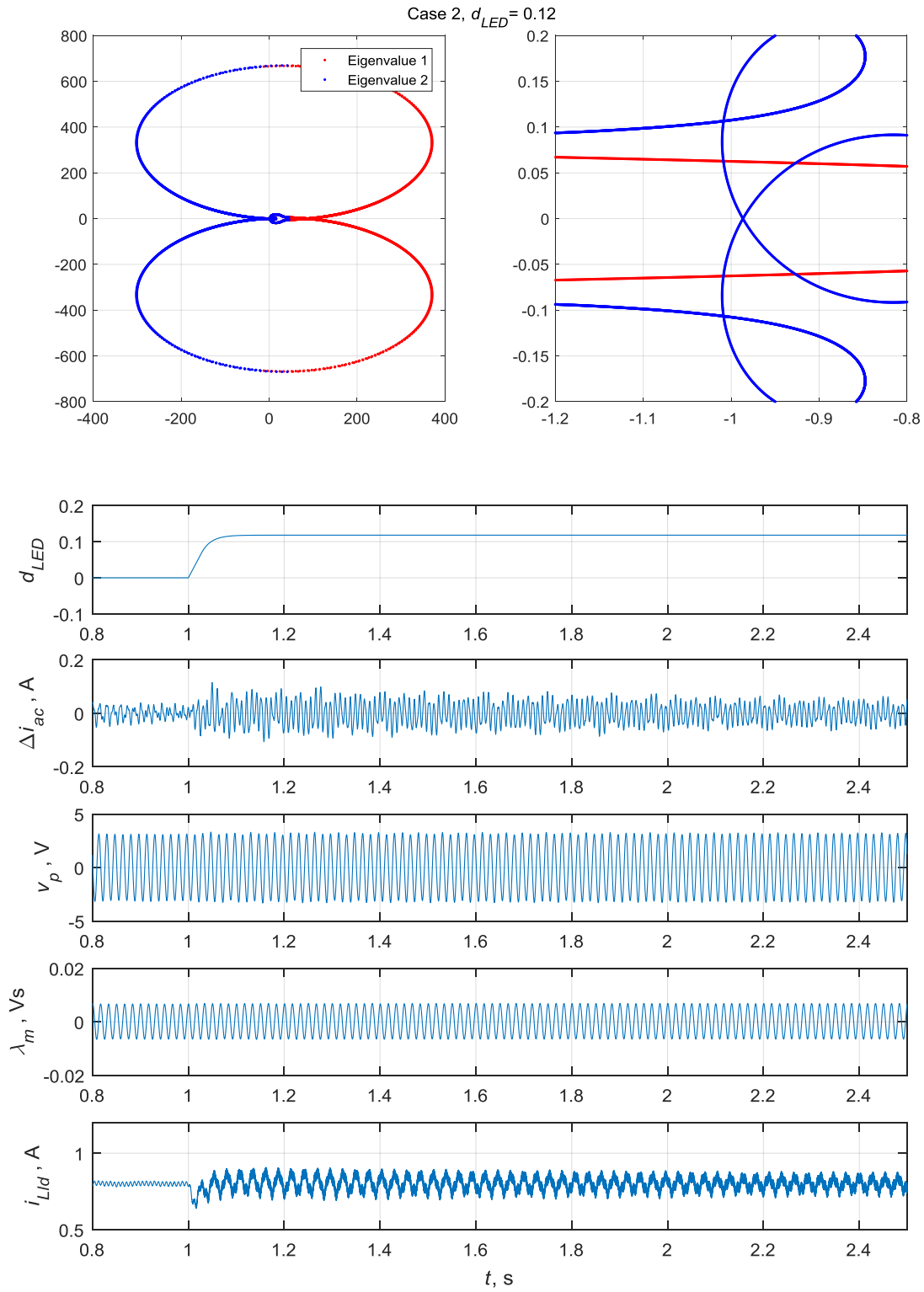


Figure 4.9 Barely stable situation

The gain margin of the Nyquist plot of a system with one load fixture can be utilized to predict the maximum number of fixtures to be safely driven. To show this, the parameter of Case 2 is used and the Nyquist plot with  $N_f = 1$  is shown in Figure 4.10. The final LED duty cycle is 40%. As can be observed from the enlarged plot closer to the crossover between the contours and  $x$ -axis, the gain margin of the single-load system is around 39.3, so that the maximum number of load fixtures is 39. Figure 4.11 shows the time-domain waveforms of 38, 39, 40, and 41 load numbers by simulating WLM. It can be seen that the system goes through the border between stability and instability as the load number increase from 38 to 41.

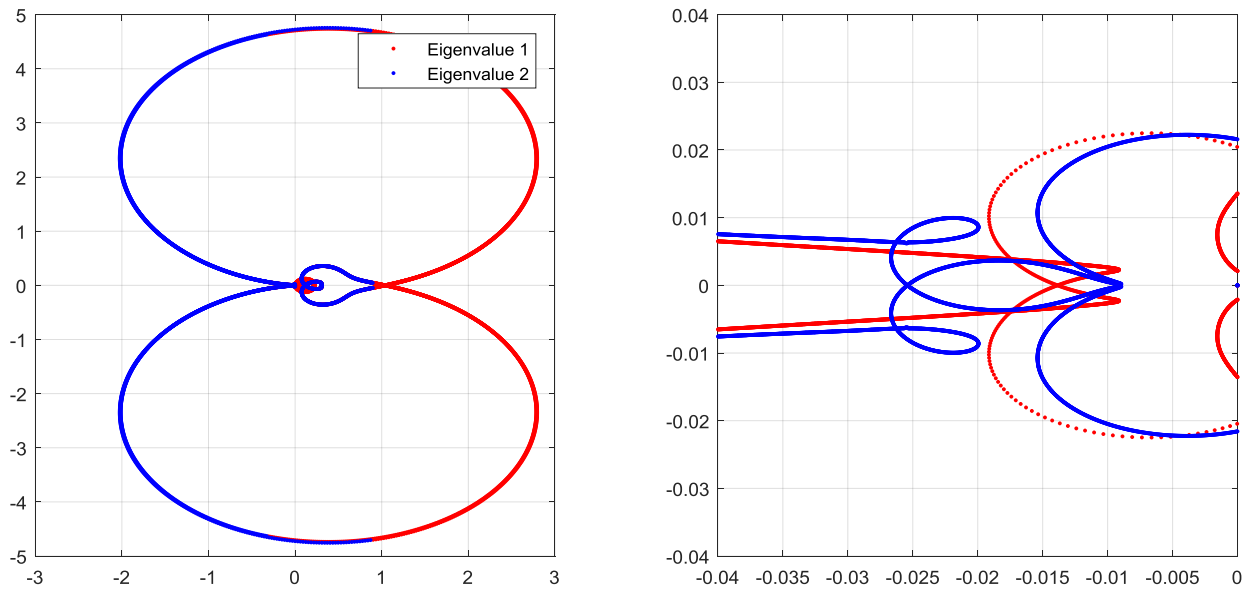


Figure 4.10 Nyquist plot of Case 2,  $N_f = 1$

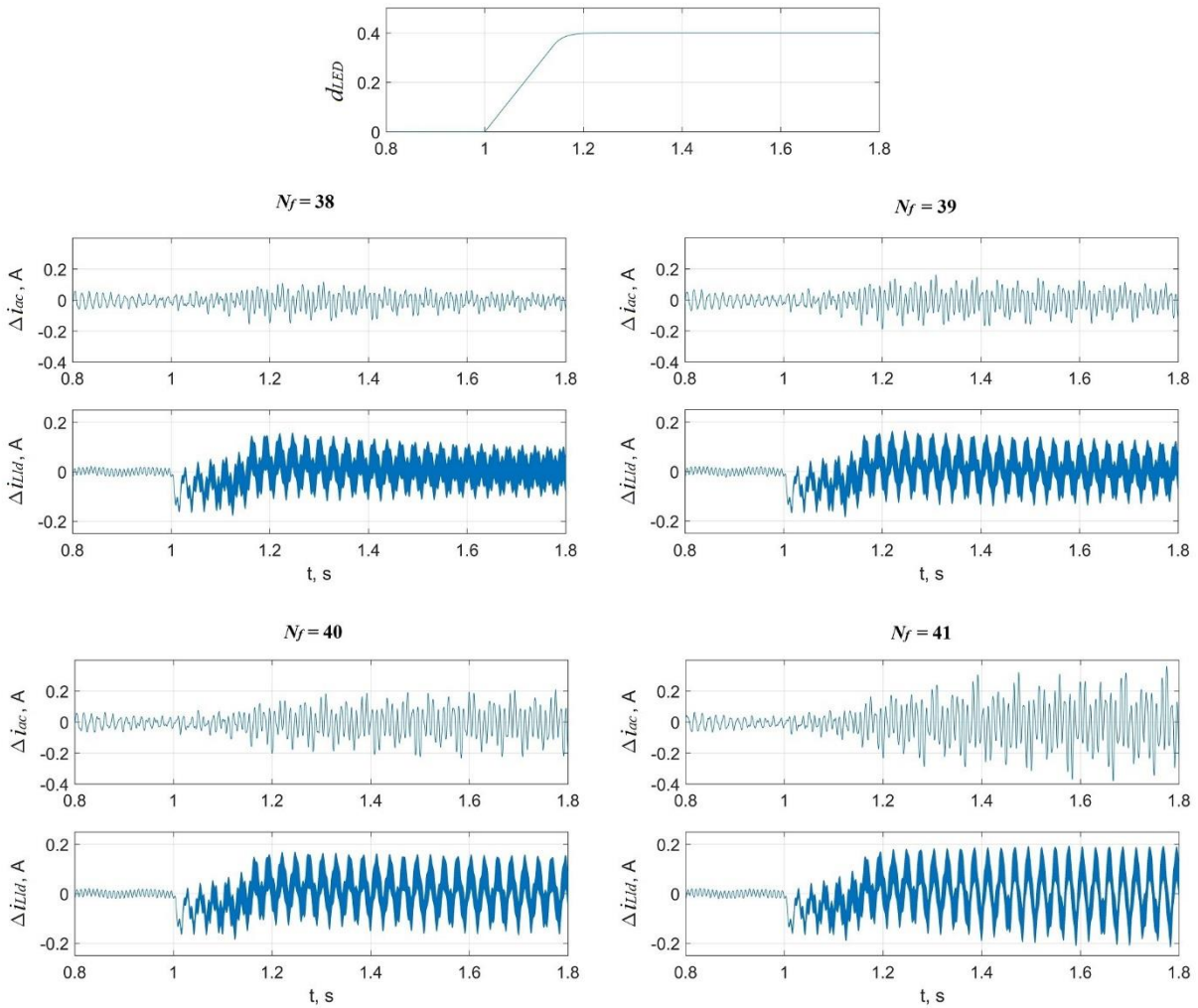


Figure 4.11 Time-domain waveforms for 38, 39, 40, and 41 load numbers

## 5. IMPEDANCE MEASUREMENT

As stated in Section 4.2, a property of the frequency-domain stability analysis is that the gain margin predicts the maximum number of load fixtures that can be stably driven. However, the method developed in Chapter 4 is based on the average-value  $qd$  model of the system, which requires detailed knowledge of the system components. An advantage of the Nyquist stability analysis is that the impedance of a system component can be physically measured, so there would be no need for the detailed knowledge of what is inside of the load or source “black box.” To show this, the theoretic basis of small-signal  $q-q$ ,  $q-d$ ,  $d-q$ ,  $d-d$  impedance characterization of a system component (either load fixture or source) based on measurement is introduced in this chapter.

Previously, [54] and [60] developed impedance measurement methods in DC and three-phase AC systems, respectively; [61] proposed a single-phase impedance measurement method, which utilizes the Hilbert transformation to produce an artificial  $b$ -phase system for  $qd$  transformations. It employs the FFT (fast Fourier transformation) to extract phasor information from the transformed  $qd$  signals. Based on these previous works, a simplified small-signal  $qd$  impedance measurement approach with direct phasor extraction is developed herein. In particular, Section 5.1 introduces the methodologies of small-signal injection, phasor extraction of a certain frequency component, and impedance (or admittance) calculation. Section 5.2 presents simulations of the  $qd$  impedance and admittance measurement on the load fixture and the current source, respectively, using the waveform-level models developed in Chapter 2. Although, the simulation results are not in perfect agreement with the analytic results from AVQDM (average-value  $qd$  model), the gain margins estimates agree. Section 5.3 demonstrates the hardware validation of the proposed method using an experimented load fixture.

### 5.1 Principles of Impedance/Admittance Measurement

#### 5.1.1 Definition of small-signal injection and response

From previous chapters, all  $qd$  currents, voltages, and flux linkages should be constant in the steady-state. Therefore, the  $qd$  current can be expressed as the sum of the DC component and a small-signal variation as

$$\mathbf{i}_{qd}(t) = \mathbf{i}_{qd0} + \Delta \mathbf{i}_{qd}(t) \quad (5.1)$$

where  $\mathbf{i}_{qd0}$  is the DC operating point of the  $qd$  current, and  $\Delta\mathbf{i}_{qd}$  is the small-signal variation. Similarly, the  $qd$  voltage can be expressed as

$$\mathbf{v}_{qd}(t) = \mathbf{v}_{qd0} + \Delta\mathbf{v}_{qd}(t) \quad (5.2)$$

where  $\mathbf{v}_{qd0}$  is the DC operating point of the  $qd$  voltage corresponding to  $\mathbf{i}_{qd0}$ , and  $\Delta\mathbf{v}_{qd}$  is the voltage variation due to  $\Delta\mathbf{i}_{qd}$ . For the load fixture, the relationship between the voltage and current variations can be described by the incremental (or small-signal) impedance matrix as

$$\Delta\mathbf{v}_{qd} = \mathbf{Z}_{qdl}\Delta\tilde{\mathbf{i}}_{qd} = \begin{bmatrix} Z_{qq} & Z_{qd} \\ Z_{dq} & Z_{dd} \end{bmatrix} \Delta\tilde{\mathbf{i}}_{qd} \quad (5.3)$$

Similarly, for the source, the relationship between the current and voltage variations can be described by the incremental admittance matrix as

$$\Delta\tilde{\mathbf{i}}_{qd} = \mathbf{Y}_{qds}\Delta\mathbf{v}_{qd} = \begin{bmatrix} Y_{qq} & Y_{qd} \\ Y_{dq} & Y_{dd} \end{bmatrix} \Delta\mathbf{v}_{qd} \quad (5.4)$$

Both (5.3) and (5.4) contains four  $s$ -domain transfer functions corresponding to the small-signal  $q$ - $q$ ,  $q$ - $d$ ,  $d$ - $q$ , and  $d$ - $d$  dependences. In Chapter 4, these components were derived through average-value modeling. The outcome of impedance/admittance measurement is a set of frequency-domain evaluations of system component characteristics, which can be used for small-signal stability analysis. In particular, it was shown in Subsection 4.2.2 that the system return loop response with  $N_f$  number of load fixtures is

$$\mathbf{L}(s) = -N_f \mathbf{Y}_{qds} \mathbf{Z}_{qdl} \quad (5.5)$$

Therefore, the incremental impedance characterization using small-signal injection produces a means to perform stability assessment without detailed circuit knowledge.

To acquire the impedance matrix in (5.3) or the admittance matrix in (5.4) at a certain frequency, sinusoidal currents or voltages with small amplitudes can be used as “probes” to be injected to an operating load or source. For certain frequency  $\omega_i$ , if two different sets of current injections (phasors of  $\Delta\mathbf{i}_{qd1}$  and  $\Delta\mathbf{i}_{qd2}$ ) are made, while two sets of voltage responses (phasors of  $\Delta\mathbf{v}_{qd1}$  and  $\Delta\mathbf{v}_{qd2}$ ) are measured, the four unknowns,  $Z_{qq}$ ,  $Z_{qd}$ ,  $Z_{dq}$ , and  $Z_{dd}$  of  $\mathbf{Z}_{qdl}$  in (5.5) can be solved using

$$\begin{bmatrix} \Delta \tilde{v}_{q1} |_{\omega_i} \\ \Delta \tilde{v}_{d1} |_{\omega_i} \\ \Delta \tilde{v}_{q2} |_{\omega_i} \\ \Delta \tilde{v}_{d2} |_{\omega_i} \end{bmatrix} = \begin{bmatrix} \Delta \tilde{i}_{q1} |_{\omega_i} & \Delta \tilde{i}_{d1} |_{\omega_i} & 0 & 0 \\ 0 & 0 & \Delta \tilde{i}_{q1} |_{\omega_i} & \Delta \tilde{i}_{d1} |_{\omega_i} \\ \Delta \tilde{i}_{q2} |_{\omega_i} & \Delta \tilde{i}_{d2} |_{\omega_i} & 0 & 0 \\ 0 & 0 & \Delta \tilde{i}_{q2} |_{\omega_i} & \Delta \tilde{i}_{d2} |_{\omega_i} \end{bmatrix} \begin{bmatrix} Z_{qq}(\omega_i) \\ Z_{qd}(\omega_i) \\ Z_{dq}(\omega_i) \\ Z_{dd}(\omega_i) \end{bmatrix} \quad (5.6)$$

Here, the phasor representation of any variable  $f$  at frequency  $\omega_i$  is denoted  $f|_{\omega_i}$ .

In order to solve (5.6), all the phasors associate with the two injections and responses are needed. To this end, first the  $qd$ -phase injections are chosen and used to determine the corresponding values on  $a$ -phase for either a simulation or an experiment. Note that the two sets of injections should be linearly independent, otherwise the current matrix in (5.6) becomes singular. The choice of injection is discussed in Subsection 5.1.2. Second, an algorithm is needed to extract the phasor information from a measured time-domain waveform; this is introduced in Subsection 5.1.3. Third, the expectations of measured waveforms are discussed to gather all components that contribute to  $qd$  phasors. Finally, in Subsection 5.1.5, a method to directly extract the desired information from the measured  $a$ -phase waveform to calculate  $qd$  phasors is illustrated.

Since positive and negative frequency components must be treated differently, this chapter assumes that, without loss of generality, only positive frequency components are present.

### 5.1.2 Injection assignment

To begin, a set of  $qd$  current injections can be expressed as

$$\Delta \mathbf{i}_{qd}(t) = \begin{bmatrix} \Delta i_q(t) \\ \Delta i_d(t) \end{bmatrix} = \begin{bmatrix} I_q \cos(\omega_i t + \phi_q) \\ I_d \cos(\omega_i t + \phi_d) \end{bmatrix} \quad (5.7)$$

Similarly, the  $qd$  voltage response can be expressed as

$$\Delta \mathbf{v}_{qd}(t) = \begin{bmatrix} \Delta v_q(t) \\ \Delta v_d(t) \end{bmatrix} = \begin{bmatrix} V_q \cos(\omega_i t + \theta_q) \\ V_d \cos(\omega_i t + \theta_d) \end{bmatrix} \quad (5.8)$$

The phasor forms of these variables with respect to  $\omega_i$  as fundamental frequency, are

$$\Delta \tilde{\mathbf{i}}_{qd} = \begin{bmatrix} \Delta \tilde{i}_q \\ \Delta \tilde{i}_d \end{bmatrix} = \begin{bmatrix} I_q \angle \phi_q \\ I_d \angle \phi_d \end{bmatrix} \quad (5.9)$$

$$\Delta \tilde{\mathbf{v}}_{qd} = \begin{bmatrix} \Delta \tilde{v}_q \\ \Delta \tilde{v}_d \end{bmatrix} = \begin{bmatrix} V_q \angle \theta_q \\ V_d \angle \theta_d \end{bmatrix} \quad (5.10)$$

where  $I_q$ ,  $I_d$ ,  $V_q$ , and  $V_d$  are magnitudes; and  $\phi_q$ ,  $\phi_d$ ,  $\theta_q$ , and  $\theta_d$  are phases, respectively.

Recall from previous chapters that the  $qd$  variables in time domain can be obtained by applying  $qd$  transformation

$$\mathbf{f}_{qd}(t) = \mathbf{K}(t) \mathbf{f}_{ab}(t) \quad (5.11)$$

where

$$\mathbf{K}(t) = \mathbf{K}^{-1}(t) = \begin{bmatrix} \cos(\omega_e t) & \sin(\omega_e t) \\ \sin(\omega_e t) & -\cos(\omega_e t) \end{bmatrix} \quad (5.12)$$

Consequently, the  $a$  and  $b$  phase variables corresponding to (5.7) or (5.8) become

$$\Delta \mathbf{f}_{ab} = \begin{bmatrix} f_q \cos(\omega_i t + \phi_q) \cos(\omega_e t) + f_d \cos(\omega_i t + \phi_d) \sin(\omega_e t) \\ f_q \cos(\omega_i t + \phi_q) \sin(\omega_e t) - f_d \cos(\omega_i t + \phi_d) \cos(\omega_e t) \end{bmatrix} \quad (5.13)$$

where variable  $f$  can be either current or voltage.

For the first injection set, assign  $f_q = f_d = f_1$ ,  $\phi_q = \phi_d + \pi/2 = \phi_1$  within (5.13), which yields

$$\Delta \mathbf{f}_{ab1} = f_1 \begin{bmatrix} \cos((\omega_e - \omega_i)t - \phi_1) \\ \sin((\omega_e - \omega_i)t - \phi_1) \end{bmatrix} \quad (5.14)$$

with the phasor form

$$\Delta \tilde{\mathbf{f}}_{ab1} \Big|_{\omega_e - \omega_i} = f_1 \begin{bmatrix} 1 \angle -\phi_1 \\ -j1 \angle -\phi_1 \end{bmatrix} \quad (5.15)$$

If  $\omega_e < \omega_i$ , a negative frequency appears in (5.14). To avoid this, (5.14) can be rewritten as

$$\Delta \mathbf{f}_{ab1} = f_1 \begin{bmatrix} \cos((\omega_i - \omega_e)t + \phi_1) \\ -\sin((\omega_i - \omega_e)t + \phi_1) \end{bmatrix} \quad (5.16)$$

for  $\omega_e < \omega_i$  so that all frequencies become positive. Note that consequently, its phasor form has also been changed. On the other hand, if  $\omega_e = \omega_i$ , there is no phasor definition for (5.14) or (5.16).

Therefore, this special case should be avoided. Hence, equation (5.15) can be reformed as

$$\Delta \tilde{\mathbf{f}}_{ab1} \Big|_{|\omega_e - \omega_i|} = \begin{cases} f_1 \begin{bmatrix} 1 \angle -\phi_1 \\ -j1 \angle -\phi_1 \end{bmatrix}, \omega_i < \omega_e \\ \text{Undefined}, \omega_i = \omega_e \\ f_1 \begin{bmatrix} 1 \angle \phi_1 \\ j1 \angle \phi_1 \end{bmatrix}, \omega_i > \omega_e \end{cases} \quad (5.17)$$

For the second injection, set  $f_q = f_d = f_2$ ,  $\phi_q = \phi_d - \pi/2 = \phi_2$  yielding

$$\Delta \mathbf{f}_{ab2} = f_2 \begin{bmatrix} \cos((\omega_e + \omega_i)t + \phi_2) \\ \sin((\omega_e + \omega_i)t + \phi_2) \end{bmatrix} \quad (5.18)$$

with phasor form

$$\Delta \tilde{\mathbf{f}}_{ab2} \Big|_{\omega_e + \omega_i} = f_2 \begin{bmatrix} 1 \angle \phi_2 \\ -j1 \angle \phi_2 \end{bmatrix} \quad (5.19)$$

Note that the  $qd$  forms of the above two set of injections are

$$\Delta \mathbf{f}_{qd1} = f_1 \begin{bmatrix} \cos(\omega_i t + \phi_1) \\ \sin(\omega_i t + \phi_1) \end{bmatrix}, \Delta \tilde{\mathbf{f}}_{qd1} \Big|_{\omega_i} = f_1 \begin{bmatrix} 1 \angle \phi_1 \\ -j1 \angle \phi_1 \end{bmatrix} \quad (5.20)$$

$$\Delta \mathbf{f}_{qd2} = f_2 \begin{bmatrix} \cos(\omega_i t + \phi_2) \\ -\sin(\omega_i t + \phi_2) \end{bmatrix}, \Delta \tilde{\mathbf{f}}_{qd2} \Big|_{\omega_i} = f_2 \begin{bmatrix} 1 \angle \phi_2 \\ j1 \angle \phi_2 \end{bmatrix} \quad (5.21)$$

Aside from ensuring the linear independence, the advantage of the above two injection sets are that they correspond to simple  $a$ -phase and  $b$ -phase waveforms, and the  $b$ -phase waveform is (either positive or negative) 90 degrees apart from the  $a$ -phase one. Therefore, only simulation or experiment of  $a$ -phase is needed, which fills the demand of characterization of a single-phase ac system.

### 5.1.3 Phasor extraction from time-domain waveform

Because of the noise present in both physical circuits and measurements, a phasor extraction algorithm is needed to convert a measured time-domain signal to its phasor form. This algorithm is expected to remove any frequency component except the desired one at  $\omega_i$ . In [61], this is accomplished with FFT (fast Fourier transform). With increasing numbers of sampling points of a waveform and sampling frequencies, the computing complexity of FFT increases. To avoid this, we may extract the phasor based on only one frequency, thus the FFT (or DFT) becomes a single Fourier series. The derivation below provides a simple illustration of the phasor extraction

using Fourier series in a continuous-time perspective.

Recall that every periodic time-domain signal can be expressed by a sum of sinusoidal signals as

$$x(t) = \sum_{n=1}^{\infty} a_n \cos(\omega_n t + \phi_n) + a_0 \quad (5.22)$$

By definition, the  $\omega_n$  component of this signal has a phasor form  $a_n \angle \phi_n$ . It can be shown that

$$\frac{4}{kT} \int_t^{t+kT/2} \cos(\omega_n t) \cos(\omega_n t + \phi_n) dt = \cos \phi_n \quad (5.23)$$

$$\frac{4}{kT} \int_t^{t+kT/2} \sin(\omega_n t) \cos(\omega_n t + \phi_n) dt = -\sin \phi_n \quad (5.24)$$

where  $T = 2\pi/\omega_n$ , and  $k$  is an integer larger than 1. Therefore, the phasor at frequency  $\omega_n$  of a given periodic signal  $x(t)$  can be extracted using

$$\text{Re}\{\tilde{x}\} = \frac{4}{kT} \int_t^{t+kT/2} \cos(\omega_n t) x(t) dt \quad (5.25)$$

$$\text{Im}\{\tilde{x}\} = -\frac{4}{kT} \int_t^{t+kT/2} \sin(\omega_n t) x(t) dt \quad (5.26)$$

where  $T = 2\pi/\omega_n$ . To ensure accuracy, it is desired that  $k$  is a large integer to reduce errors from those disturbances whose frequency is not a multiple of  $T$ .

In practice, it is important that (5.25) and (5.26) are carried out with respect to the same time reference for the injected current and the voltage response within one set. From (5.6), the time references between the two sets are irrelevant, i.e., the two sets of current injections and voltage responses do not have to be measured or processed with the same time reference.

#### 5.1.4 Time-domain considerations

Recall the topology of the load fixture as shown in Figure 5.1. Herein, to measure the load impedance, small signal current is injected to  $i_p$  and the voltage responses in  $v_p$  is measured. The load voltage on the H-bridge rectifier can be expressed as

$$\hat{v}_r = d_H \hat{v}_{CId} \quad (5.27)$$

The AC duty cycle  $d_H$  is a sinusoidal signal controlled by the inductor current  $i_{Ls}$  with

$$d_H = \frac{y}{i_{L_s,base}} \hat{i}_{L_s} \quad (5.28)$$

where  $y$  is the DC control output, and  $i_{L,base}$  is a constant. Therefore, ideally  $v_r$  (switching averaged) is a sinusoidal voltage.

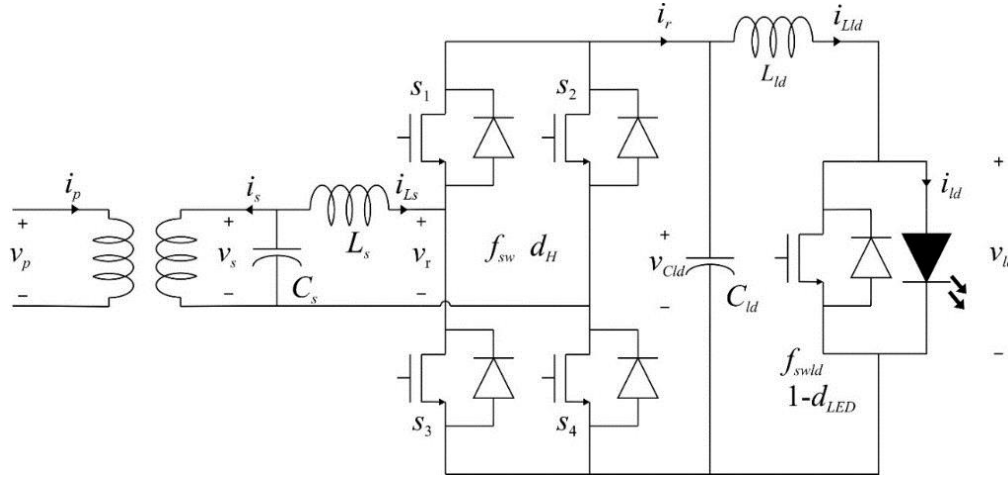


Figure 5.1 Load Fixture topology

Next, the rectified current can be expressed by

$$\hat{i}_r = d_H \hat{i}_{L_s} = \frac{y}{i_{L_s,base}} \hat{i}_{L_s}^2 \quad (5.29)$$

where  $\hat{i}_{L_s}$  retains both the fundamental frequency component (at  $\omega_e$ ) and the small-signal injection component (at  $|\omega_e - \omega_i|$  or  $\omega_e + \omega_i$ ).

Suppose that the first injection (5.14) is carried out in  $i_p$ . This component will then be passed to  $i_{L_s}$ . Because of the square of  $i_{L_s}$  in (5.29), the rectified current will then incorporate all frequency components at the linear combinations of  $\omega_e - \omega_i$  and  $\omega_e$ . These frequencies includes  $\omega_i$ . Thus, an  $\omega_i$  component will appear in  $v_{Cid}$ . Then, from (5.27) and (5.28),  $v_r$  will incorporate all frequency components at the linear combinations of  $\omega_i$  and  $\omega_e$ , and others. Therefore, an  $\omega_e + \omega_i$  components will appear in  $v_r$ , and then passed back to  $v_p$ . Figure 5.2 illustrate these time-domain waveforms and the corresponding spectrum amplitude (extracted using FFT), where  $\omega_i = 2\pi \cdot 40$  Hz and  $\omega_e - \omega_i = 2\pi \cdot 20$  Hz perturbation is injected to  $a$ -phase. As can be seen in the spectrums, a small  $\omega_e + \omega_i = 2\pi \cdot 100$  Hz component appears in  $v_r$  and  $v_p$ .

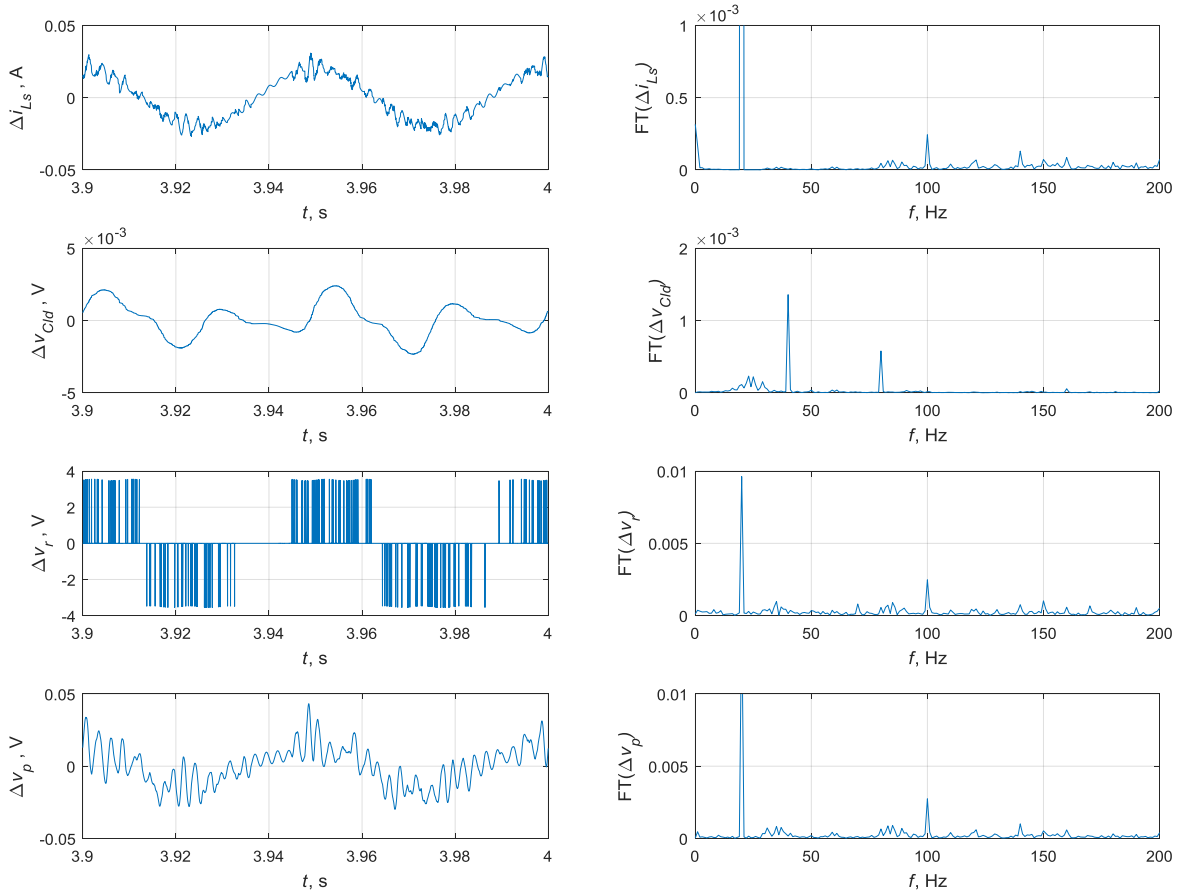


Figure 5.2 Load waveforms with  $\omega_i = 2\pi \cdot 40$  Hz, first set (5.14).

On the other hand, suppose that the second injection (5.18) is carried out. This component will then be passed to  $i_{Ls}$ . Because of the square of  $i_{Ls}$  in (5.29), the rectified current will then incorporate all frequency components at the linear combinations of  $\omega_i + \omega_e$  and  $\omega_e$ . These include many frequencies including  $\omega_i$ . Thus, an  $\omega_i$  component will appear in  $v_{Cld}$ . Then, from (5.27) and (5.28),  $v_r$  will incorporate all frequency components at the linear combinations of  $\omega_i$  and  $\omega_e$ , and others. Therefore, an  $|\omega_e - \omega_i|$  components will appear in the voltage responses in  $v_r$ , and then passed back to  $v_p$ . Figure 5.3 illustrate this situation where  $\omega_i = 2\pi \cdot 40$  Hz and  $\omega_e + \omega_i = 2\pi \cdot 100$  Hz perturbation is injected to the  $a$ -phase. As can be seen from the spectrums, a small  $\omega_e - \omega_i = 2\pi \cdot 20$  Hz component appears in  $v_r$  and  $v_p$ .

In summary, it is expected in a nonlinear system, both the  $|\omega_i - \omega_e|$  and  $\omega_e + \omega_i$  components exist, no matter which frequency of the two is injected to the current. Meanwhile, (5.20) and (5.21)

shows that these two components both contribute to the  $qd$  phasors. Therefore, both the two components must be considered for both injections.

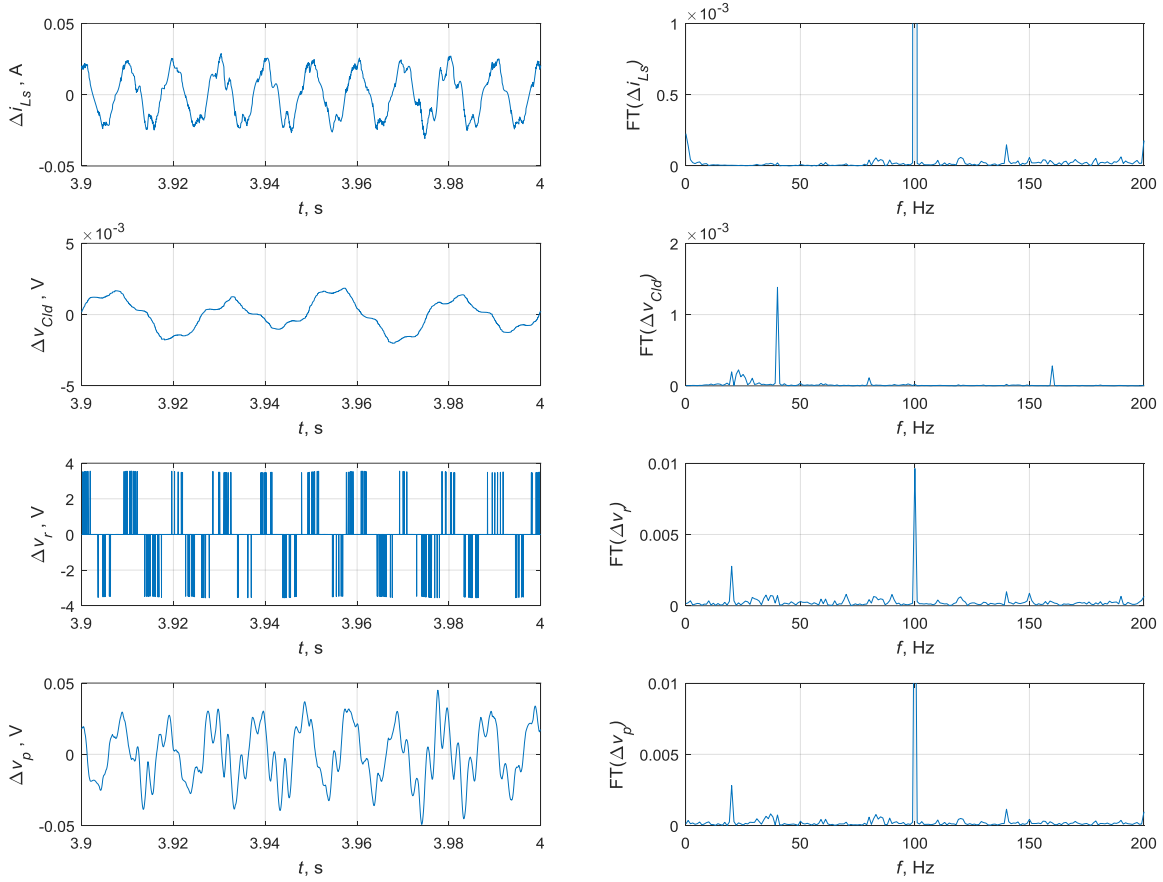


Figure 5.3 Load waveforms with  $\omega_i = 2\pi \cdot 40$  Hz, second set (5.18).

### 5.1.5 Single-phase $qd$ impedance measurement algorithm

Consider any set of  $qd$  current injections in the form (5.7). Its phasor form (5.9) can be regarded as arbitrary linear combination of the two linearly independent injections (5.20) and (5.21). From (5.13) and use trigonometric identities,

$$\begin{aligned} 2\Delta f_a &= f_q \cos((\omega_e - \omega_i)t - \phi_q) + f_q \cos((\omega_e + \omega_i)t + \phi_q) \\ &+ f_d \sin((\omega_e - \omega_i)t - \phi_d) + f_d \sin((\omega_e + \omega_i)t + \phi_d) \end{aligned} \quad (5.30)$$

From the phasor perspective, assuming  $\omega_e > \omega_i$ , suppose from measurement we have

$$\Delta \tilde{f}_a \Big|_{\omega_e - \omega_i} = \frac{1}{2} (f_q \angle -\phi_q - j f_d \angle -\phi_d) = a_m + j b_m \quad (5.31)$$

$$\Delta \tilde{f}_a \Big|_{\omega_e + \omega_i} = \frac{1}{2} (f_q \angle \phi_q - j f_d \angle \phi_d) = c_m + j d_m \quad (5.32)$$

We may also assume

$$\Delta \tilde{f}_q \Big|_{\omega_i} = f_q \angle \phi_q = a + j b \quad (5.33)$$

$$\Delta \tilde{f}_d \Big|_{\omega_i} = f_d \angle \phi_d = c + j d \quad (5.34)$$

Substituting (5.33) and (5.34) into (5.31) yields

$$\frac{1}{2} (a - j b - j c - d) = a_m + j b_m \quad (5.35)$$

Substituting (5.33) and (5.34) into (5.32) yields

$$\frac{1}{2} (a + j b - j c + d) = c_m + j d_m \quad (5.36)$$

Combining (5.35) and (5.36), and after some algebra,

$$\begin{bmatrix} a \\ b \\ c \\ d \end{bmatrix} = \begin{bmatrix} 1 & 0 & 1 & 0 \\ 0 & -1 & 0 & 1 \\ 0 & -1 & 0 & -1 \\ -1 & 0 & 1 & 0 \end{bmatrix} \begin{bmatrix} a_m \\ b_m \\ c_m \\ d_m \end{bmatrix} \quad (5.37)$$

Substituting (5.37) back into (5.33) and (5.34) yields

$$\Delta \tilde{f}_q \Big|_{\omega_i} = a_m - j b_m + c_m + j d_m = -j \tilde{f}_a^* \Big|_{\omega_e - \omega_i} + \tilde{f}_a \Big|_{\omega_e + \omega_i} \quad (5.38)$$

$$\Delta \tilde{f}_d \Big|_{\omega_i} = -j a_m - b_m + j c_m - d_m = -j \tilde{f}_a^* \Big|_{\omega_e - \omega_i} + j \tilde{f}_a \Big|_{\omega_e + \omega_i} \quad (5.39)$$

Similarly, when  $\omega_e < \omega_i$ , (5.30) can be rewrite as

$$\begin{aligned} 2\Delta f_a &= f_q \cos((\omega_i - \omega_e)t + \phi_q) + f_q \cos((\omega_e + \omega_i)t + \phi_q) \\ &- f_d \sin((\omega_i - \omega_e)t + \phi_d) + f_d \sin((\omega_e + \omega_i)t + \phi_d) \end{aligned} \quad (5.40)$$

In this case, suppose from measurement we have

$$\Delta \tilde{f}_a \Big|_{\omega_i - \omega_e} = \frac{1}{2} (f_q \angle \phi_q + j f_d \angle \phi_d) = a_m + j b_m \quad (5.41)$$

$$\Delta \tilde{f}_a \Big|_{\omega_e + \omega_i} = \frac{1}{2} (f_q \angle \phi_q - j f_d \angle \phi_d) = c_m + j d_m \quad (5.42)$$

Substituting (5.41) and (5.42) into (5.33) yields

$$\frac{1}{2}(a + jb + jc - d) = a_m + jb_m \quad (5.43)$$

Substituting (5.41) and (5.42) into (5.34) yields

$$\frac{1}{2}(a + jb - jc + d) = c_m + jd_m \quad (5.44)$$

Combining (5.43) and (5.44) and manipulating

$$\begin{bmatrix} a \\ b \\ c \\ d \end{bmatrix} = \begin{bmatrix} 1 & 0 & 1 & 0 \\ 0 & 1 & 0 & 1 \\ 0 & 1 & 0 & -1 \\ -1 & 0 & 1 & 0 \end{bmatrix} \begin{bmatrix} a_m \\ b_m \\ c_m \\ d_m \end{bmatrix} \quad (5.45)$$

Substituting (5.45) back into (5.33) and (5.34) yields

$$\Delta \tilde{f}_q \Big|_{\omega_i} = a_m + jb_m + c_m + jd_m = \tilde{f}_a \Big|_{\omega_i - \omega_e} + \tilde{f}_a \Big|_{\omega_e + \omega_i} \quad (5.46)$$

$$\Delta \tilde{f}_d \Big|_{\omega_i} = -ja_m + b_m + jc_m - d_m = -j\tilde{f}_a \Big|_{\omega_i - \omega_e} + j\tilde{f}_a \Big|_{\omega_e + \omega_i} \quad (5.47)$$

By observation of the phasor relationship between (5.17) and (5.20), the  $qd$  phasor of the first injection set can be directly obtained from its  $a$ -phase phasor using

$$\Delta \tilde{\mathbf{f}}_{qd1} \Big|_{\omega_i} = \begin{cases} \begin{bmatrix} \Delta f_{a1}^* \Big|_{|\omega_i - \omega_e|} \\ -j\Delta f_{a1}^* \Big|_{|\omega_i - \omega_e|} \end{bmatrix}, \omega_i < \omega_e \\ \text{Undefined}, \omega_i = \omega_e \\ \begin{bmatrix} \Delta f_{a1} \Big|_{|\omega_i - \omega_e|} \\ -j\Delta f_{a1} \Big|_{|\omega_i - \omega_e|} \end{bmatrix}, \omega_i > \omega_e \end{cases} \quad (5.48)$$

where the star sign represents complex conjugate. Similarly, by observing the relationship between (5.19) and (5.21),

$$\Delta \tilde{\mathbf{f}}_{qd2} \Big|_{\omega_i} = \begin{bmatrix} \Delta f_{a2} \Big|_{\omega_e + \omega_i} \\ j\Delta f_{a2} \Big|_{\omega_e + \omega_i} \end{bmatrix} \quad (5.49)$$

Since not only the components at the injected frequency  $|\omega_e - \omega_i|$  ( $\omega_e + \omega_i$ ) contributes to the  $qd$  phasors, but also another one with different frequency  $\omega_e + \omega_i$  ( $|\omega_e - \omega_i|$ ), (5.48) and (5.49) should

be added together for both the first and the second set of injections. The word ‘add’ here means the numeric sum of complex numbers, while the phasors are extracted independently based on different frequencies. Hence,

$$\Delta \tilde{\mathbf{f}}_{qd1} \Big|_{\omega_i} = \begin{cases} \begin{bmatrix} \Delta f_{a1}^* \Big|_{|\omega_e - \omega_i|} + \Delta f_{a1} \Big|_{\omega_e + \omega_i} \\ -j\Delta f_{a1}^* \Big|_{|\omega_e - \omega_i|} + j\Delta f_{a1} \Big|_{\omega_e + \omega_i} \end{bmatrix}, \omega_i < \omega_e \\ \text{Undefined}, \omega_i = \omega_e \\ \begin{bmatrix} \Delta f_{a1} \Big|_{|\omega_e - \omega_i|} + \Delta f_{a1} \Big|_{\omega_e + \omega_i} \\ -j\Delta f_{a1} \Big|_{|\omega_e - \omega_i|} + j\Delta f_{a1} \Big|_{\omega_e + \omega_i} \end{bmatrix}, \omega_i > \omega_e \end{cases} \quad (5.50)$$

$$\Delta \tilde{\mathbf{f}}_{qd2} \Big|_{\omega_i} = \begin{cases} \begin{bmatrix} \Delta f_{a2}^* \Big|_{|\omega_e - \omega_i|} + \Delta f_{a2} \Big|_{\omega_e + \omega_i} \\ -j\Delta f_{a2}^* \Big|_{|\omega_e - \omega_i|} + j\Delta f_{a2} \Big|_{\omega_e + \omega_i} \end{bmatrix}, \omega_i < \omega_e \\ \text{Undefined}, \omega_i = \omega_e \\ \begin{bmatrix} \Delta f_{a2} \Big|_{|\omega_e - \omega_i|} + \Delta f_{a2} \Big|_{\omega_e + \omega_i} \\ -j\Delta f_{a2} \Big|_{|\omega_e - \omega_i|} + j\Delta f_{a2} \Big|_{\omega_e + \omega_i} \end{bmatrix}, \omega_i > \omega_e \end{cases} \quad (5.51)$$

Which is identical to the results (5.38), (5.39), (5.46), and (5.47). Therefore, for the introduced two injection phasors (5.20) and (5.21) can be regarded as a set of basis vectors, and any two linearly independent vectors within the space based on this basis set can be utilized for injections.

In summary, the  $qd$  transformation and Hilbert transformation used in [61] can be eliminated from the overall process, so that the computational expense is greatly reduced. Also, the measurement for operating point waveform (at 60 Hz) in [61] is no longer needed. The process of this simplified single-phase  $qd$  impedance measurement can be summarized in Table 5.1.

Table 5.1  $Qd$  impedance measurement procedure

Step	Operation
1	Inject current variations $\Delta i_{a1}$ at $ \omega_e - \omega_i $
2	Measure $i_{a1}(t)$ and $v_{a1}(t)$
3	Extract phasors of $i_{a1}(t)$ and $v_{a1}(t)$ at $ \omega_e - \omega_i $ and $\omega_e + \omega_i$
4	Calculate the phasors of $\Delta \mathbf{i}_{qd1}$ and $\Delta \mathbf{v}_{qd1}$ using (5.50)
5	Repeat Step 1 to 4 for $\Delta i_{a2}$ at $\omega_e + \omega_i$
6	Use (5.6) to solve impedance values $Z_{qq}, Z_{qd}, Z_{dq}, Z_{dd}$ at $\omega_i$ .
7	Repeat Step 1 to 6 for next $\omega_i$

## 5.2 Numerical Validation Study

To test the single-phase impedance/admittance measurement method introduced in Section 5.1, a simulation is presented in this section. The waveform-level model of the single-phase load fixture is used to mimic the real equipment. The input operating points are obtained from the simulation results from previous chapters. The overall input current is assumed to be a sum of the operational point values and the small-signal variation injections. The current variation amplitude of the load fixture is 0.05 A, and the voltage variation amplitude of the source is 0.5 V. The output level (duty cycle of LED) is 50%. Parameters in Table 2.1 (for source) and Table 2.2 (for load fixture) are utilized for both  $qd$  average-value modeling and measurement simulations. The simulation uses the ode4 (Runge-Kutta) solver and the simulation time step is 1  $\mu$ s, which is relatively large (compared to the 0.5  $\mu$ s time step used in Chapter 2) but increases speed. In the following studies for both the load fixture and the source, 50 integer frequencies are tested. The phasor extraction uses the time interval from 3s to 4s after the simulation starts.

Figure 5.4 represents the comparison between the fixture impedance measurement simulation and the modeled impedance from the linearized fixture model in Subsection 4.2.2. It can be seen that the two set of results are very close except for around 120 Hz (754 rad/s). This is caused by the approximation taken in the  $qd$  average-value modeling in Chapter 3, where the

voltage across  $C_{ld}$  is assumed to be constant state variable in steady state, so that the rectifier input voltage  $v_r$  is ideally sinusoidal; however, as discussed in Subsection 5.1.3,  $v_r$  can include multiple frequency components that influence  $qd$  variables. This verifies the effectiveness of the simplified measurement procedure proposed in Subsection 5.1.4.

Figure 5.5 provides a verification of the source admittance measurement, which is carried out with identical procedures with impedance measurement except for the interchange of voltages and currents. It can be seen that the simulation of the measurement results agree with the average-value model results very well.

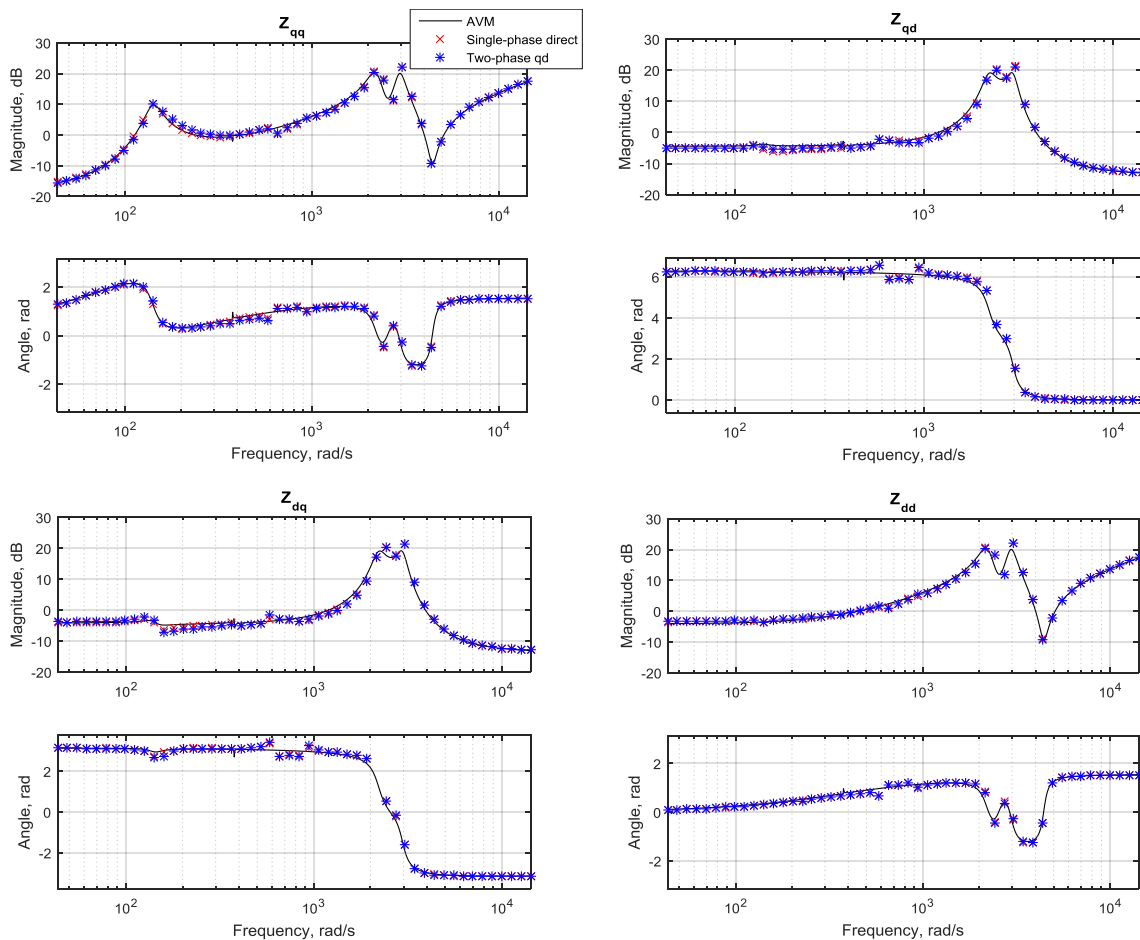


Figure 5.4 Comparison between impedance measurement and modeling

To verify the Nyquist stability analysis based on the measurement,  $\mathbf{Z}_{qdl}$  and  $\mathbf{Y}_{qds}$ , Figure 5.6 provides the comparison between the plots of the eigenvalues of  $\mathbf{Y}_{qds}\mathbf{Z}_{qdl}$  from 30 to 180 Hz, using the system parameters from Table 2.3 and Table 2.4, and the output duty cycle is 50%. These

contours are a part of the Nyquist plot shown in Figure 4.7 ( $d_{LED} = 0.5$  case). There is a symmetric contour of the plotted one which represents the eigenvalues of  $\mathbf{Y}_{qds}\mathbf{Z}_{qdl}$  from -30 to -180 Hz, which is not shown here. Also, from Figure 4.7, this part incorporate the critical point where left-most crossover of the x-axis, and it is used to found gain margin. As can be seen from the enlarged contours in the right part of Figure 5.6, the eigenvalue contours are different but the gain margins are close. The gain margin obtained analytically from AVQDM is around 39.3, while from simulated impedance/admittance measurement it is around 40. Therefore, their predictions on the maximum number of load fixtures to be stably driven are close.

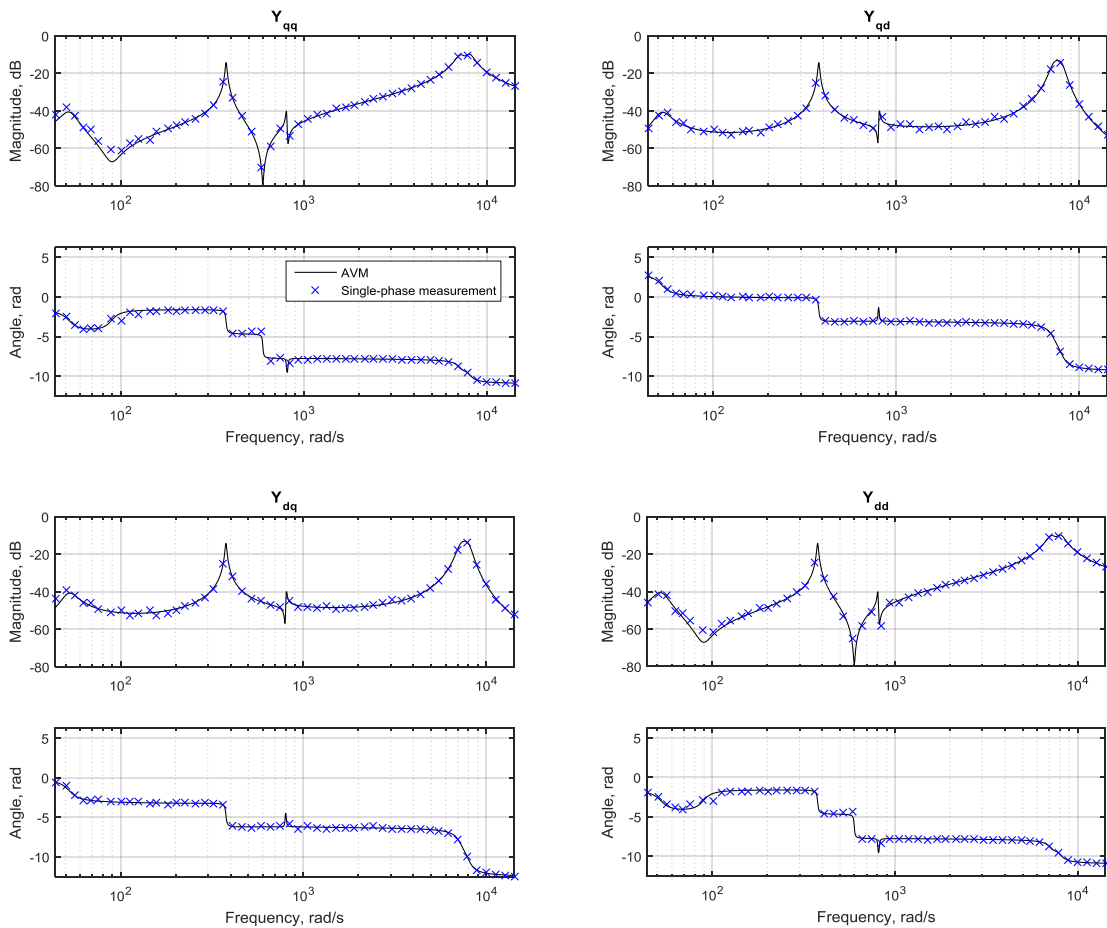


Figure 5.5 Comparison between admittance measurement and modeling

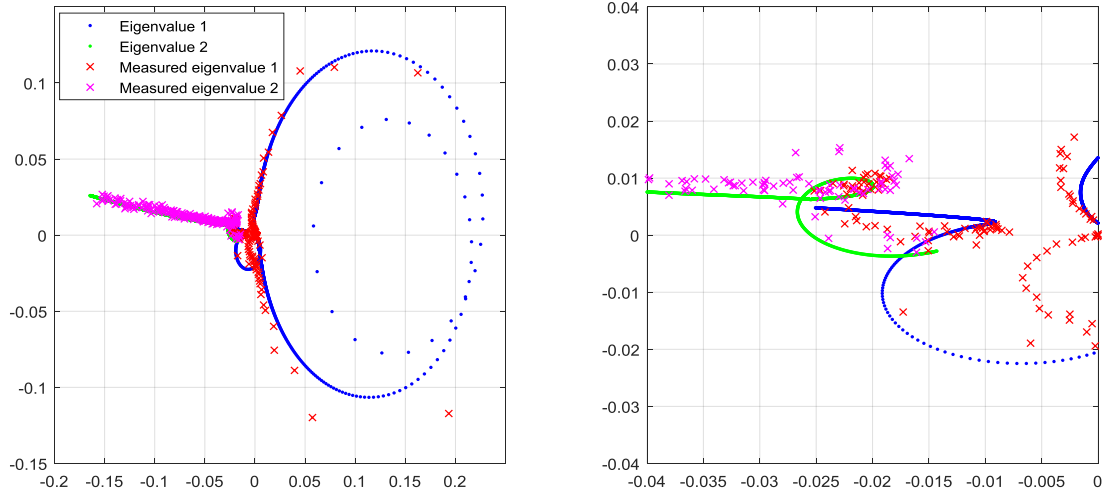


Figure 5.6 Nyquist plot comparison

In conclusion, the simulation validates the proposed procedure for the single-phase small-signal impedance/admittance measurement. Compared to the waveform-level and average-value modeling method for stability analysis, which is design-oriented, the impedance measurement approach is more useful in stability analysis incorporating an existing hardware. In next Section, an experiment to demonstrate the  $qd$  impedance measurement is introduced.

## 5.3 Hardware Validation

### 5.3.1 Model modification

The implementation of the considered topology is driven by functionality, cost, size, efficiency, heat dissipation, etc. Amplitude-shift or frequency-shift keying technologies may be utilized to control every load fixture. Multiple DC regulators are required to power different circuit aspects. These cause the actual design of lighting fixture to be complex.

To realize the proposed fixture shown Figure 5.1 with limited cost, the modified circuit and control diagram shown in Figure 5.7 and 5.8, respectively, are used. In this design, only the basic functionality is realized. The details of the circuit design and realization of control with operational amplifiers are discussed in Appendix I. The characterization of the isolation transformer and the inductors are presented in Appendix II. It can be seen from Figure 5.7 that compared to the topology of Figure 5.1, the parallel switch of the load LED is removed for control simplicity, and two Zener diodes are added for LED overload protection.

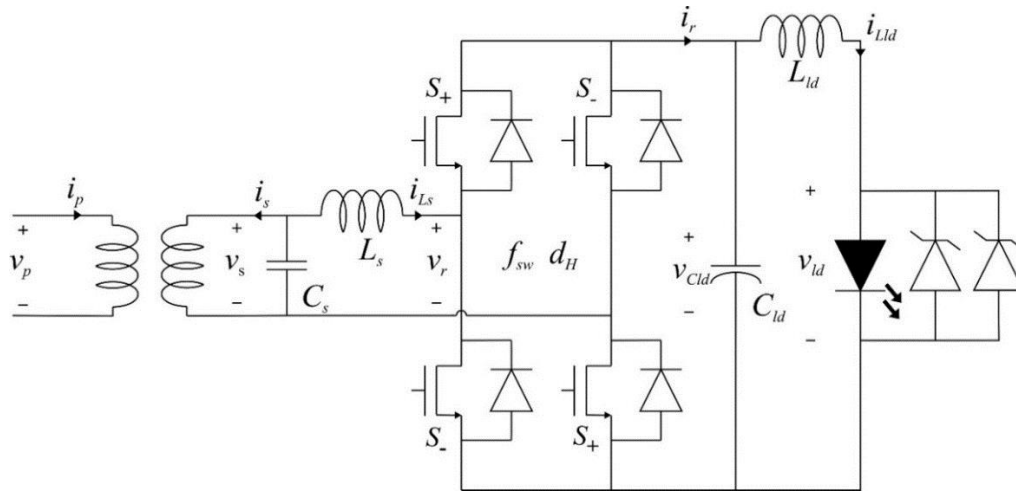


Figure 5.7 Modified fixture topology

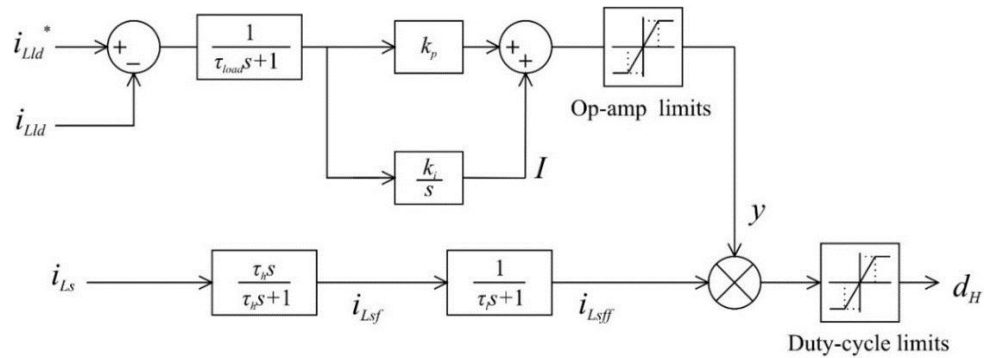


Figure 5.8 Modified control diagram

Additional filters are added to this control diagram. To filter the low-frequency ripple (especially the 120 Hz ripple due to rectifier) from  $i_{Lld}$  going into the control, a load current filter is added with cut-off frequency  $\tau_{load}$  (in radians per second). For the load current filter, a simple state variable assignment is to include both proportional and integrational paths of the PI control with

$$y(s) = \frac{1}{\tau_{load}s+1} \left[ k_i I + k_p (i_{Lld}^* - i_{Lld}) \right] (s) \quad (5.52)$$

where  $y$  is the output of the filtered PI control as shown in Figure 5.8, and  $I$  is the integrator value. Transforming (5.38) to time-domain yields

$$py = \frac{k_i}{\tau_{load}} I + \frac{k_p}{\tau_{load}} (i_{Lld}^* - i_{Lld}) - \frac{1}{\tau_{load}} y \quad (5.53)$$

The purpose of this low-pass filter is to reduce low-frequency noises (especially the 120 Hz noise caused by the rectifier).

For the lower part of Figure 5.8, a high-pass filter (with critical frequency  $1/\tau_h$  in radians per second) is added, so it forms a band-pass filter with the original low-pass filter (with critical frequency  $1/\tau_l$  in radians per second). The pass band of this filter is then from  $1/\tau_h$  to  $1/\tau_l$ , and should be around the synchronous frequency, so that ripple and noise in the sensed  $i_{Ls}$  will be attenuated in the control. From these transfer functions

$$i_{Lsf}(s) = \frac{\tau_h s}{\tau_h s + 1} i_{Ls}(s) \quad (5.54)$$

$$i_{Lsff}(s) = \frac{1}{\tau_l s + 1} i_{Lsf}(s) \quad (5.55)$$

two state variables ( $i_{Lsf}$  and  $i_{Lsff}$ ) are needed to demonstrate the time-domain behavior of this band-pass filter with

$$p i_{Lsf} = p i_{Ls} - \frac{1}{\tau_h} i_{Lsf} \quad (5.56)$$

$$p i_{Lsff} = \frac{1}{\tau_h} i_{Lsf} - \frac{1}{\tau_l} i_{Lsff} \quad (5.57)$$

Since (5.42) and (5.43) are linear ODEs, their corresponding  $qd$  variable dynamics are similar to (3.75) and (3.76) and are governed by

$$p i_{Lsfq} = p i_{Lsq} + \omega_e i_{Lsd} - \frac{1}{\tau_h} i_{Lsfq} - \omega_e i_{Lsfd} \quad (5.58)$$

$$p i_{Lsfd} = p i_{Lsd} - \omega_e i_{Lsd} - \frac{1}{\tau_h} i_{Lsfd} + \omega_e i_{Lsfq} \quad (5.59)$$

$$p i_{Lsffq} = \frac{1}{\tau_h} i_{Lsfq} - \frac{1}{\tau_h} i_{Lsffq} - \omega_e i_{Lsffd} \quad (5.60)$$

$$p i_{Lsffd} = \frac{1}{\tau_h} i_{Lsfd} - \frac{1}{\tau_h} i_{Lsffd} + \omega_e i_{Lsffq} \quad (5.61)$$

Therefore, instead of (4.22), the state vector of the fixture becomes

$$\mathbf{x} = \begin{bmatrix} i_{pq} & i_{pd} & i'_{sq} & i'_{sd} & v_{sq} & v_{sd} & i_{Lsq} & i_{Lsd} & i_{Lsfq} & i_{Lsfd} & i_{Lsffq} & i_{Lsffd} & v_{Cld} & i_{Lld} & y & I \end{bmatrix}^T \quad (5.62)$$

The corresponding state transient matrix, instead of (4.24), can be modified as

$$\mathbf{A} = \begin{bmatrix}
 \frac{-(L_m + L'_s)(r_p + r_i)}{D} & -\omega_e & \frac{L'_m r'_s}{D} & 0 & -\frac{L_m TR}{D} & 0 \\
 \omega_e & \frac{-(L_m + L'_s)(r_p + r_i)}{D} & 0 & \frac{L'_m r'_s}{D} & 0 & -\frac{L_m TR}{D} \\
 \frac{L_m(r_p + r_i)}{D} & 0 & -\frac{(L_m + L_p)r'_s}{D} & -\omega_e & \frac{(L_m + L_p)TR}{D} & 0 \\
 0 & \frac{L_m(r_p + r_i)}{D} & \omega_e & -\frac{(L_m + L_p)r'_s}{D} & 0 & \frac{(L_m + L_p)TR}{D} \\
 0 & 0 & -\frac{TR}{C_s} & 0 & 0 & -\omega_e & \dots \\
 0 & 0 & 0 & -\frac{TR}{C_s} & \omega_e & 0 \\
 0 & 0 & 0 & 0 & \frac{1}{L_s} & 0 \\
 0 & 0 & 0 & 0 & 0 & \frac{1}{L_s}
 \end{bmatrix} \quad \mathbf{0}(10 \times 6)$$

$$\mathbf{0}(4 \times 10)$$

$$\begin{bmatrix}
 -\frac{1}{C_s} & 0 & 0 & 0 & 0 & 0 & 0 & 0 & 0 & 0 \\
 0 & -\frac{1}{C_s} & 0 & 0 & 0 & 0 & 0 & 0 & 0 & 0 \\
 -\frac{r_{Ls}}{i_{Ls,base} L_s} & -\omega_e & 0 & 0 & -\frac{y_0 V_{Cld0}}{i_{Ls,base} L_s} & 0 & -\frac{y_0 i_{Lsq0}}{i_{Ls,base} L_s} & 0 & -\frac{V_{Cld0} i_{Lsq0}}{i_{Ls,base} L_s} & 0 \\
 \omega_e & -\frac{r_{Ls}}{i_{Ls,base} L_s} & 0 & 0 & 0 & -\frac{y_0 V_{Cld0}}{i_{Ls,base} L_s} & 0 & -\frac{y_0 i_{Lsd0}}{i_{Ls,base} L_s} & -\frac{V_{Cld0} i_{Lsd0}}{i_{Ls,base} L_s} & 0 \\
 -\frac{r_{Ls}}{i_{Ls,base} L_s} & 0 & -\frac{1}{\tau_h} & -\omega_e & -\frac{y_0 V_{Cld0}}{i_{Ls,base} L_s} & 0 & -\frac{y_0 i_{Lsq0}}{i_{Ls,base} L_s} & 0 & -\frac{V_{Cld0} i_{Lsq0}}{i_{Ls,base} L_s} & 0 \\
 \dots & 0 & -\frac{r_{Ls}}{i_{Ls,base} L_s} & \omega_e & -\frac{1}{\tau_h} & 0 & -\frac{y_0 V_{Cld0}}{i_{Ls,base} L_s} & 0 & -\frac{y_0 i_{Lsd0}}{i_{Ls,base} L_s} & -\frac{V_{Cld0} i_{Lsd0}}{i_{Ls,base} L_s} \\
 0 & 0 & \frac{1}{\tau_l} & 0 & -\frac{1}{\tau_l} & -\omega_e & 0 & 0 & 0 & 0 \\
 0 & 0 & 0 & \frac{1}{\tau_l} & \omega_e & -\frac{1}{\tau_l} & 0 & 0 & 0 & 0 \\
 0 & 0 & 0 & 0 & -\frac{y_0 i_{Lsq0}}{i_{Ls,base} C_{ld}} & -\frac{y_0 i_{Lsd0}}{i_{Ls,base} C_{ld}} & 0 & -\frac{1}{C_{ld}} & \frac{i_{Lsq0}^2 + i_{Lsd0}^2}{2i_{Ls,base} C_{ld}} & 0 \\
 0 & 0 & 0 & 0 & 0 & 0 & \frac{1}{L_{ld}} & -\frac{r_{ld} + r_{led}}{L_{ld}} & 0 & 0 \\
 0 & 0 & 0 & 0 & 0 & 0 & 0 & -\frac{k_p}{\tau_{load}} & -\frac{1}{\tau_{load}} & \frac{k_i}{\tau_{load}} \\
 0 & 0 & 0 & 0 & 0 & 0 & 0 & -1 & 0 & 0
 \end{bmatrix} \quad (5.63)$$

The modification of **B**, **C**, and **D** matrices of this fixture are only adjusting dimensions with zeros. This modified *qd* average-value mode is used in next Subsection for hardware validation.

### 5.3.2 Experiment results

Figure 5.9 shows the lab setup for the impedance measurement. The LED fixture board is powered by a programmable current source, California Instruments 4500CS. The measurement on both current and voltage is taken at the primary winding of the transformer, and is shown and recorded using an oscilloscope. For validation, 20 frequencies from 180 Hz to 1320 Hz, which are multiples of 60 Hz, are selected for injection frequency  $\omega_i$ . In this way, all sets of data except 180 Hz and 1320 Hz ones can be used twice, since it can be equal to  $\omega_i - \omega_e$  when carrying the first set as (5.21), or  $\omega_e + \omega_i$  for second set (5.23). In data acquisition, every set of measured voltage and current are stored as a vector with 100100 elements representing waveforms over 0.1 s. The parameters utilized in both the experiment and the simulation are shown in Table 5.2.

The measurement results and their comparison with the *qd* average-value modeling and the simulation of waveform-level model are shown in Figure 5.10 and Table 5.3. It can be seen that the overall error between the three methods are small. The error factors include capacitor ESRs (Equivalent series resistance), semiconductor loss, transformer hysteresis loss, noise, and probe errors. Also, the closer to the synchronous frequency (60 Hz), the more systematic error will occur in data processing as the number of periods used in computation goes down.

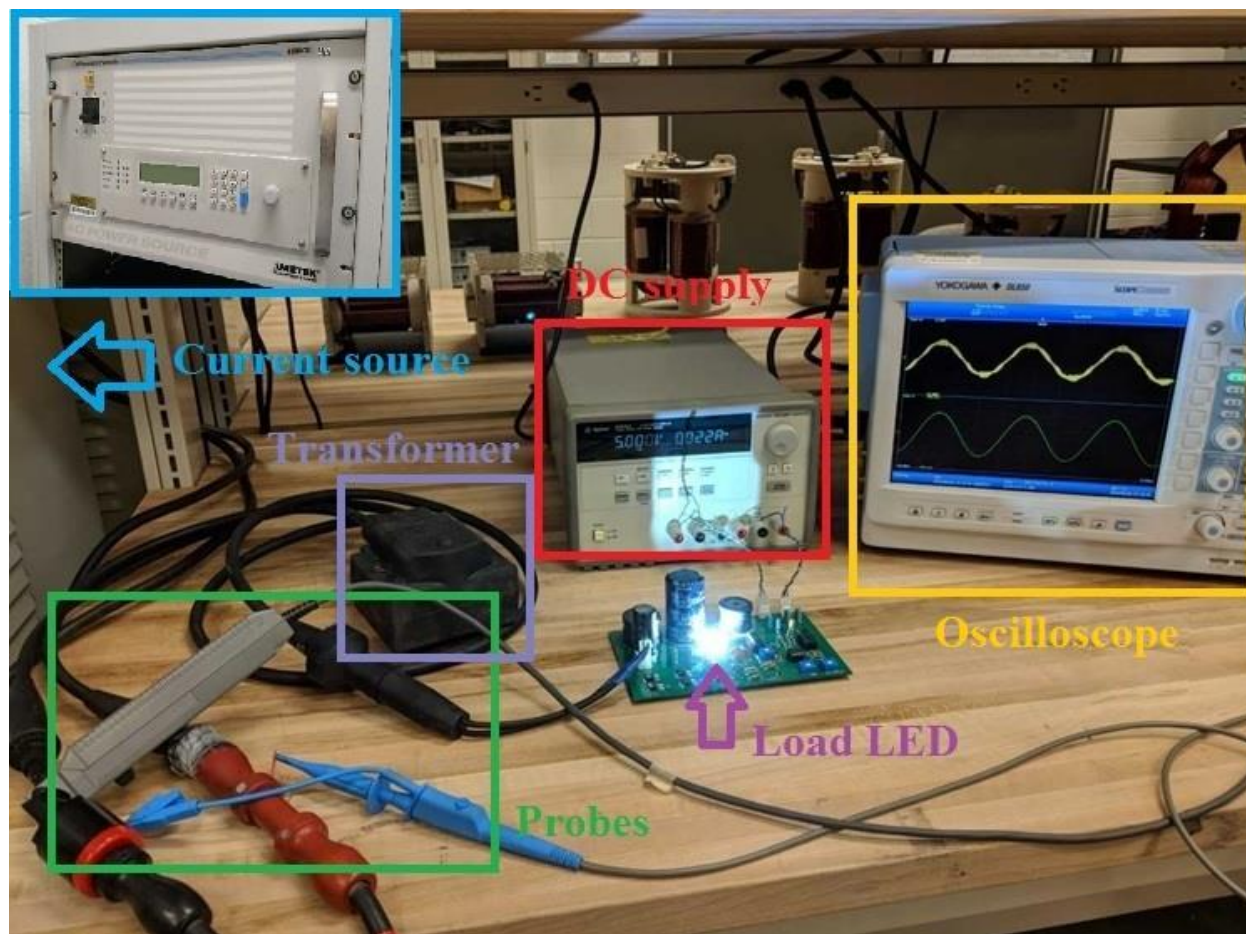


Figure 5.9 Experiment environment

Table 5.2 Fixture parameters

Component	Value
Turns ratio ( $N_p/N_s$ )	1.02
Primary winding resistance ( $r_p$ )	0.108 $\Omega$
Secondary winding resistance ( $r_s$ )	0.107 $\Omega$
Transformer coefficient $\alpha$	0.252
Transformer coefficient $\beta$	3.9087
Transformer coefficient $L_0$	1.5 mH
Primary leakage inductance ( $L_{lp}$ )	0.156 mH
Secondary leakage inductance ( $L_{ls}$ )	0.15 mH
Input filter capacitance ( $C_s$ )	206 $\mu$ F
Input filter inductance ( $L_s$ )	1.058 mH
Input filter inductor resistance ( $r_{Ls}$ )	0.255 $\Omega$
Output filter capacitance ( $C_{ld}$ )	47 mF
Output filter inductance ( $L_{ld}$ )	1.5 mH
Output filter inductor resistance ( $r_{Lld}$ )	0.49 $\Omega$
Proportional gain ( $k_p$ )	0.19
Integrational gain ( $k_i$ )	0.763
Low-pass filter time constant ( $\tau_l$ )	3.3 ms
High-pass filter time constant ( $\tau_h$ )	22 ms
Load current filter ( $\tau_{load}$ )	0.275 s
Desired load current ( $i_{Lld}^*$ )	0.8 A
LED parameter ( $i_0$ )	4.6E-20 A
LED parameter ( $v_0$ )	15.25 V
H-bridge switching frequency ( $f_{sw}$ )	30 kHz

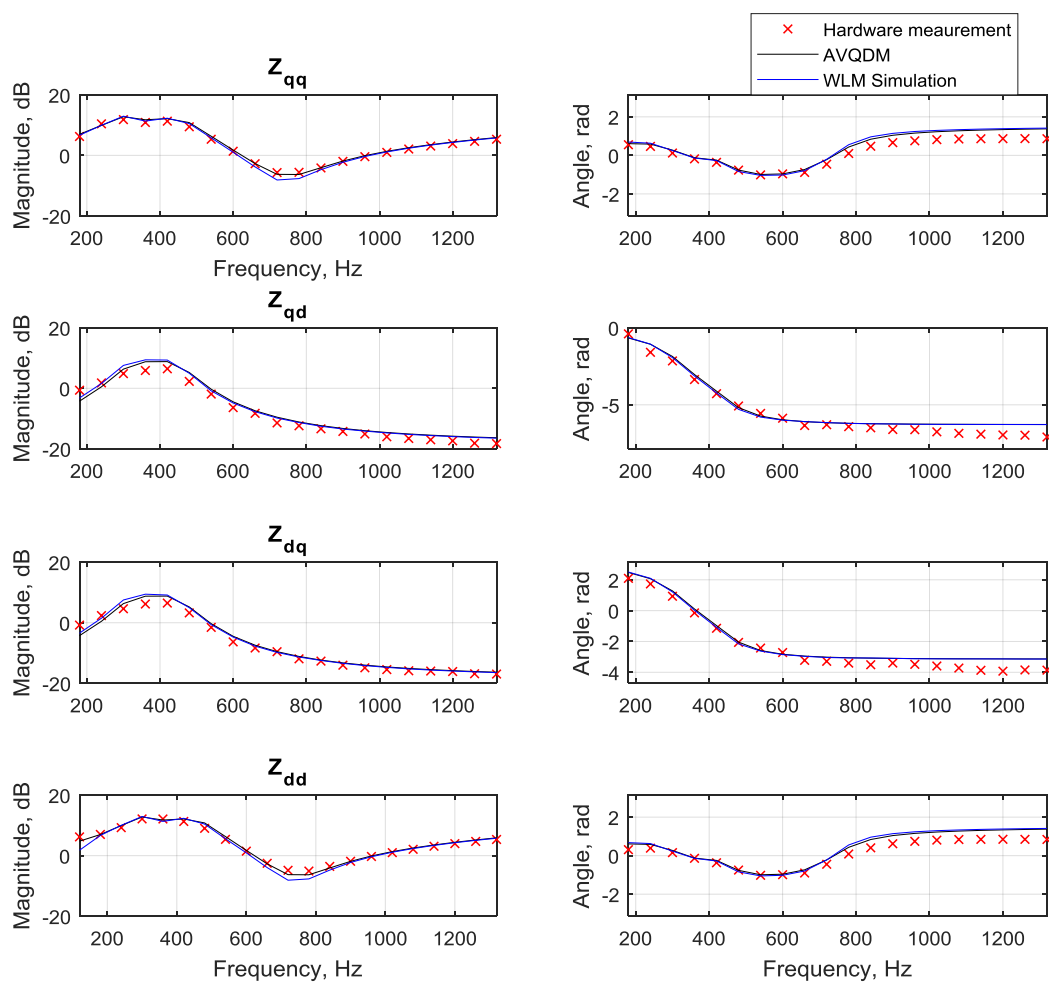


Figure 5.10 Hardware experimental result

Table 5.3 Impedance value by three methods

$\Omega$ Hz	$Z_{qq}$			$Z_{qd}$			$Z_{dq}$			$Z_{dd}$		
	A*	S*	M*	A	S	M	A	S	M	A	S	M
180	1.52 - j0.845	0.765 + j0.910	1.44 - j0.531	0.371 + j0.170	0.353 - j0.711	0.056+ j0.0951	-0.371 - j0.171	-0.338+ j0.745	-0.710 - j0.316	1.51 - j0.854	0.802 + j0.933	1.65 - j1.200
240	1.83 - j1.27	1.66 + j1.37	1.75 - j1.074	0.483 + j0.377	0.556 - j0.412	0.858 + j0.359	-0.482 - j0.377	-0.542+ j0.402	-0.458 - j0.791	1.83 - j1.28	1.68 + j1.35	2.13 - j0.687
300	2.61 - j1.73	2.54 + j1.85	2.97 - j1.487	0.508 + j0.928	0.584 - j1.05	-0.0279 + j1.23	-0.507 - j0.928	-0.597 + j1.03	-0.212 - j1.30	2.62 - j1.73	2.56 + j1.86	2.68 - j1.10
360	4.19 - j1.17	4.30 + j1.11	3.87 - j0.470	-0.597+ j1.980	-0.851 - j2.23	-0.960 + j1.46	0.597 - j1.98	0.825 + j2.23	1.01 - j1.37	4.20 - j1.17	4.32 + j1.04	4.00 - j0.635
420	3.84 + j0.479	3.65 - j0.5130	3.44 + j0.631	-2.73 + j0.291	-2.95 - j0.0399	-1.92 - j0.424	2.73 - j0.291	2.96 + j0.079	2.02 + j0.30	3.84 + j0.490	3.65 - j0.504	4.00 + j0.554
480	3.92 + j0.988	3.96 - j1.10	3.43 + j1.304	-1.56 - j2.280	-1.36 + j2.59	-0.885 - j1.90	1.56 + j2.28	1.35 - j2.53	0.872 + j1.92	3.92 + j0.992	3.98 - j1.14	3.43 + j1.32
540	2.51 + j2.40	2.24 - j2.49	2.14 + j2.055	0.829 - j1.620	0.976 + j1.48	0.463 - j1.22	-0.829 + j1.62	-0.983 - j1.48	-0.685 + j1.28	2.51 + j2.40	2.22 - j2.48	2.08 + j1.92
600	1.13 + j1.73	0.988 - j1.68	0.977+ j1.567	0.821 - j0.505	0.801 + j0.425	0.600 - j0.533	-0.821+ j0.505	-0.808 - j0.46	-0.634+ j0.548	1.13 + j1.73	0.945 - j1.65	0.974 + j1.58
660	0.699 + j1.00	0.587 - j0.96	0.67 + j0.960	0.568 - j0.183	0.548 + j0.163	0.438 - j0.193	-0.568+ j0.183	-0.555 - j0.165	-0.440+ j0.198	0.699 + j1.00	0.583 - j0.948	0.653 + j0.991
720	0.543 + j0.491	0.452 - j0.46	0.46 + j0.563	0.417 - j0.0808	0.403 + j0.0794	0.385 + j0.0228	-0.417+ j0.0808	-0.405 - j0.0727	-0.381 - j0.0318	0.543 + j0.491	0.444 - j0.454	0.465 + j0.587
780	0.474 + j0.106	0.384 - j0.0784	0.466 + j0.230	0.330 - j0.0411	0.319 + j0.0422	0.268 + j0.0022	-0.330+ j0.0411	-0.321 - j0.0327	-0.329 + j0.0485	0.474 + j0.106	0.383 - j0.086	0.517 + j0.247
840	0.438- j0.203	0.352 + j0.217	0.523 - j0.051	0.276 - j0.0232	0.271 + j0.0213	0.238 + j0.0320	-0.276+ j0.0232	-0.271 - j0.0199	-0.245 - j0.0661	0.438 - j0.203	0.351 + j0.218	0.555 - j0.047
900	0.418 - j0.465	0.332 + j0.476	0.551 - j0.282	0.241 - j0.0141	0.235 + j0.0130	0.209 + j0.0441	-0.241+ j0.0141	-0.237 - j0.0166	-0.217- j0.0836	0.418 - j0.465	0.331 + j0.473	0.610 - j0.263
960	0.406 - j0.696	0.320 + j0.700	0.629 - j0.488	0.217 - j0.0092	0.212 + j0.0088	0.184 + j0.0606	-0.217+ j0.0092	-0.213 - j0.0106	-0.192 - j0.0508	0.406 - j0.696	0.322 + j0.702	0.658 - j0.469
1020	0.398 - j0.905	0.312 + j0.906	0.693 - j0.652	0.199 - j0.0062	0.196 + j0.0042	0.166 + j0.0571	-0.199+ j0.0062	-0.196 - j0.0040	-0.170 - j0.0605	0.398 - j0.905	0.313 + j0.907	0.714 - j0.655
1080	0.392 - j1.10	0.309 + j1.10	0.767 - j0.816	0.186 - j0.0044	0.183 + j0.0026	0.141 + j0.0715	-0.186+ j0.0044	-0.183 - j0.0025	-0.152 - j0.0733	0.392 - j1.10	0.308 + j1.10	0.776 - j0.810
1140	0.388 - j1.28	0.307 + j1.28	0.841 - j0.955	0.176 - j0.0032	0.173 + j0.0024	0.125 + j0.0796	-0.176+ j0.0032	-0.173 - j0.0016	-0.134 - j0.0885	0.388 - j1.28	0.306 + j1.27	0.851 - j0.947
1200	0.385 - j1.45	0.305 + j1.45	0.927 - j1.081	0.168 - j0.0024	0.165 + j0.0014	0.115 + j0.0819	-0.168+ j0.0024	-0.165 - j0.0018	-0.119 - j0.1060	0.385 - j1.45	0.304 + j1.44	0.949 - j1.07
1260	0.383 - j1.62	0.304 + j1.61	1.01 - j1.191	0.162 - j0.0019	0.159 + j0.0011	0.106 + j0.0844	-0.162+ j0.0019	-0.159 - j0.0012	-0.110 - j0.111	0.383 - j1.62	0.303 + j1.61	1.04 - j1.19
1320	0.381 - j1.78	0.303 + j1.76	1.10 - j1.303	0.157 - j0.0015	0.154 + j0.0006	0.095+ j0.0786	-0.157+ j0.0015	-0.154 - j0.0001	-0.109 - j0.0932	0.381 - j1.78	0.302 + j1.76	1.14 - j1.29

\*Notes: A = Analytic method with average-value  $qd$  model, S = simulation with waveform-level model, M = Measurement

## 6. SUMMARY AND FUTURE WORK

In summary, this dissertation establishes a modeling and stability analysis methodology for single-phase series AC power systems. Three approaches of modeling or characterization are proposed: the waveform-level modeling (WLM), the average-value  $qd$  modeling (AVQDM), and the impedance (or admittance) measurement. All these three approaches can be utilized in stability analysis, and their results have been demonstrated to be consistent.

The three approaches have their own advantages and drawbacks. The WLM modeling is accurate but computationally intensive. It is the most reliable for design validation. However, the WLM does not directly yield the load impedance and the source admittance for frequency-domain stability analysis. The AVQDM, compared to WLM, is computationally less demanding. Another advantage of the AVQDM is that it gives an analytic expression for load impedance or source admittance, which is convenient for frequency-domain stability analysis. Both the WLM and AVQDM is based on a known detailed design of load fixture and source. The impedance measurement methodology, however, is more useful with field applications when the detailed design is unknown.

There are a few topics that are related to or need further development based on the work presented in this dissertation. First, due to equipment limitations, the low-frequency part of the impedance measurement is difficult, and so improving the low-frequency accuracy is of interest. Second, the admittance measurement of the current source should be tested. Since the admittance magnitude is small in most frequency ranges (as shown in Figure 5.5), it might be a better solution to measure its impedance instead and calculate the inverse. Third, the transmission line model may have a better representation rather than lumped elements, especially when it is extremely long (with a significant portion of the wavelength for 60 Hz). Fourth, parameter variations can be considered to form a 3D load impedance space (in frequency, magnitude and phase) and be compared to the forbidden region generated by the source admittance. This will be different and more complex compared to the DC system case in [5], since here the impedance and admittance are two-by-two matrices instead of variables.

## APPENDIX A. LED FIXTURE DESIGN EXAMPLE

This appendix is a supplement to Section 5.3. To implement the proposed notional topology, numerous factors must be considered, including functionality, cost, size, efficiency, heat dissipation, etc. Amplitude-shift or frequency-shift keying technologies may be utilized in practice, and additional demodulation function are needed for the control circuits subsequently. In addition, multiple DC regulators are required to power on different circuit aspects. These cause the actual design to be complex and expensive.

The proposed design aims to achieve the basic functionality with limited cost. An overview of the circuit is shown in Figure A.1. There are two parts of this design: the power stage and the control stage. The power part is similar to the proposed topology in Chapter 2, but the parallel switch of the load LED for duty cycle control is removed. The control part, with modification presented in Chapter 5, is achieved by an analog circuit with amplifiers, a multiplier and PWM generator. Section A.1 and A.2 describe the power stage and the control stage respectively. The parameters of the circuit elements are also shown in Figure A1, and they correspond to the synthesize parameters in Table 5.2.

### A.1 Power stage

To reduce complexity, the modulation of the LED duty cycle is removed, therefore the LED duty cycle is always 100%. For better robustness and protection, two Zener diodes (D3 and D5) are added in parallel to the LED. The reverse conducting voltage of the Zener diodes should be an appropriate value higher than the operating voltage of the LED. If the reverse conducting voltage is too small, the Zener diodes will draw more current from the LED; if it is too large, the protection functionality is lost. The Zener diodes also shorts the LED when the load current direction is accidentally reversed.

The LED used in this design is an XLamp® XP-E2 Torch LED. During normal operation, the current flow through the Zener diodes is very small. When the load current, i.e. sum of LED and Zener diode currents, exceeds the current limit of the LED, the percentage of Zener diode current increases faster so that the LED current increment is reduced. In the given circuit diagram, the tolerance of load current is increased from 1.5 A to around 2 A.

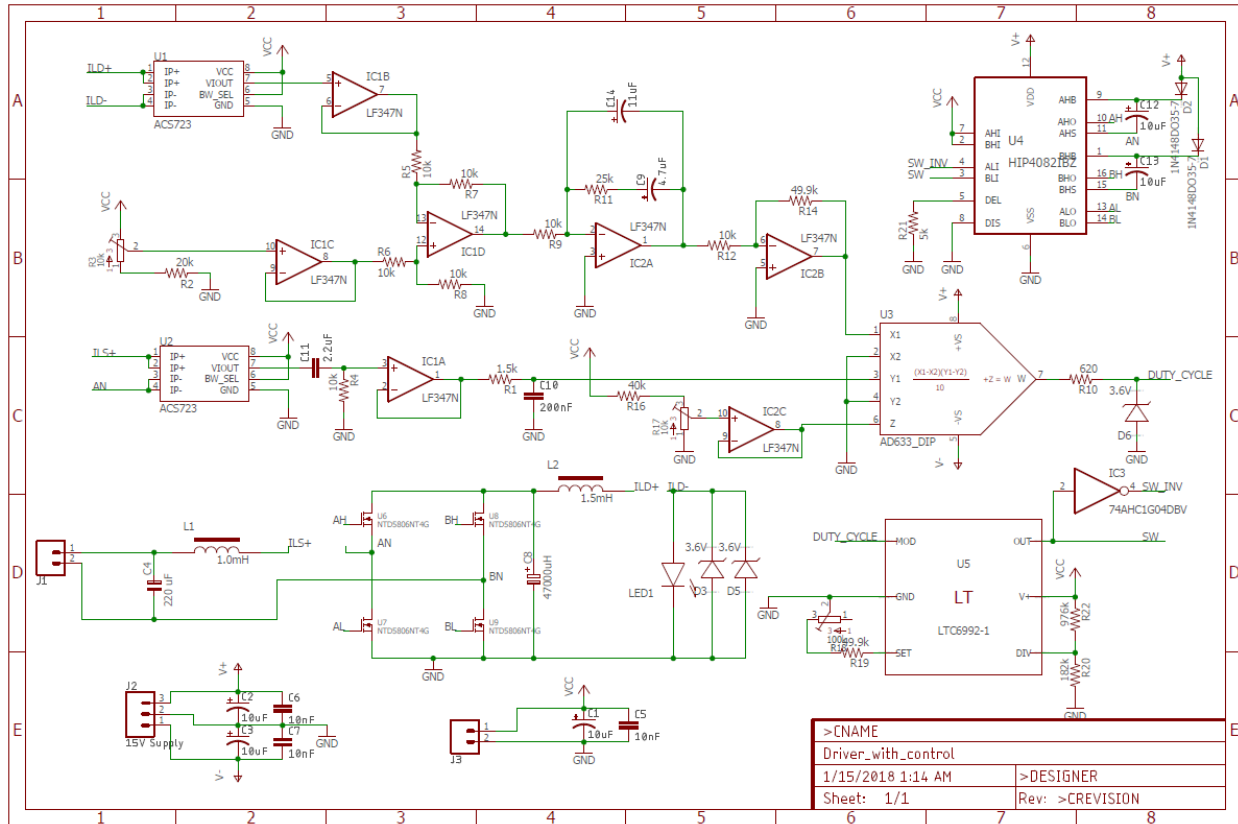


Figure A.1 Circuit overview

## A.2 Analog control circuit

From analog circuit theory, a PI control can be realized by operational amplifier (op-amp) circuits. The circuit in Figure A2 implements a PI control with a low-pass filter. Since the voltage on the negative input of the op-amp can be approximated as zero, the current coming into the op-amp is zero, using KCL, the relationship between input and output voltages of this circuit can be expressed by

$$\frac{v_1}{r_1} + v_2 \left( sC_1 + \frac{1}{r_2 + \frac{1}{sC_2}} \right) = 0 \quad (\text{A.1})$$

After some algebra, the transfer function corresponding to this circuit can be derived as

$$\frac{v_2}{v_1} = -\frac{1}{r_2 C_1 s + 1} \left( \frac{r_2}{r_1} + \frac{1}{r_1 C_2 s} \right) \quad (\text{A.2})$$

Therefore, this circuit realizes a PI control with a low-pass filter. The proportional gain of this control is  $r_2/r_1$ , and the integrational gain is  $1/(r_1C_2)$ . The cut-off frequency of the load low-pass filter (with  $\tau_{load}$  as shown in Figure 6.12) is  $1/(2\pi r_2C_1)$ .

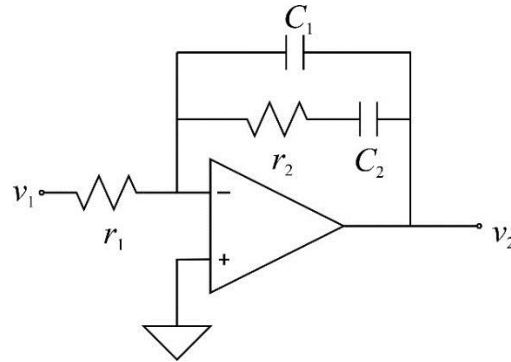


Figure A.2 Op-amp based PI control (with filter)

An analog multiplier is utilized to them to generate a duty cycle signal from the sinusoidal waveform and the PI control output. To convert the sinusoidal input to the duty cycle signal ranging from 0 to 1 V, a 0.5 V dc offset is applied through the ‘Z’ input of the multiplier. This offset value can also be adjusted by a variable resistor (R17). The overall ac gain applied to  $d_H$  through these procedures should be multiplied to the control gain  $k_p$  and  $k_i$  for small-signal analysis.

The duty cycle signal is then passed to the PWM generator (U5). The input of this device is protected by a voltage divider consisted with a resistor (R10) and a Zener diode (D6). The PWM signal then passes the control signal to a bridge driver (U4). The major purpose of the bridge driver is to utilize a bootstrap circuit (with D1, D2, C12 and C13) to increase the gate voltage of the upper two MOSFETs (U6 and U8) so that they are higher than the voltages on their source pins.

## APPENDIX B. INDUCTOR AND TRANSFORMER CHARACTERIZATION

This appendix is a supplement to both Chapter 2 and Section 5.3. The objective of the characterization of the electromagnetic components is to correlate measurement with lumped models. In particular, Section B.1 describes the inductor characterization and Section B.2 documents the transformer characterization.

### B.1 Inductor characterization

The inductor is one of the most basic elements. It is widely used in power electronics applications such as DC-DC converters to reduce current ripple. Meanwhile, inductance commonly exists in all conductors, and becomes increasingly apparent for high frequency signals. In the application discussed in this thesis, the maximum frequency induced in the single-phase power system is the switching frequency of H-bridge MOSTFETs or IGBTs. In a load fixture active rectifier, the switching frequency is small enough so that the wire inductance on PCB can be ignored. Consequently, all small-signal models of inductors (except the transformer mutual inductance) in a load fixture can be regarded as series RL circuits. However, for large-signal analysis, the saturation of inductors and transformers must be considered. Herein, the voltage equations of a magnetically coupled circuit can be expressed as

$$\mathbf{v} = \mathbf{r}\mathbf{i} + \frac{d}{dt}\boldsymbol{\lambda} \quad (\text{B.1})$$

where the vectors  $\mathbf{v}$ ,  $\mathbf{r}$ ,  $\mathbf{I}$ , and  $\boldsymbol{\lambda}$  has only one element for a inductor, and two or more elements for a transformer (with two or more windings). The objective of the following two subsection are to find the vector  $\mathbf{r}$  and the function  $\boldsymbol{\lambda}(\mathbf{i})$  of a given inductor or transformer through measurement.

The winding resistance of an inductor is dependent on its length, cross-section area, and its material (usually copper), and it is usually very small. A two-wire measurement utilizing DMM (Digital multi-meter) will not be accurate since the wire and probe resistances are not negligible. Meanwhile, due to skin effect [66, 67] and proximity effect [68-70], the AC resistance is dependent of frequency and should be larger than the DC resistance. This is not obvious in low-frequency situations and is not investigated here. An appropriate method to measure winding resistance is to

use four-wire measurement as shown in Figure B1. Since the impedance of the voltage meter is very large, its current is negligible, so that the measured voltage and current are both accurate. The source in Figure B1 should be a DC voltage supply with current limitations in order to protect the DUT (device under test).

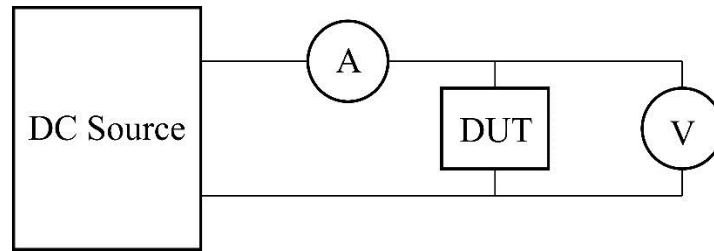


Figure B.1 Four-wire measurement for DC resistance

According to (B.1), if the wire resistance of an inductor is known, the flux linkage  $\lambda$  at certain time  $t_1$  can be found as

$$\lambda(t_1) = \int_{t_0}^{t_1} (v - ri) dt + C \quad (\text{B.2})$$

where  $C$  is a constant to eliminate DC offset. Equation (B.2) shows that the function  $\lambda(i)$  can be evaluated by measuring current and voltage simultaneously. This can be realized by the setup shown in Figure B2. The data acquired in this test can be processed through a script to calculate the impedance. Note that the recorded waveform from oscilloscope should include at least one complete period of the injected AC waveform, in order to produce a closed  $\lambda - i$  curve. To increase accuracy, multiple cycles can be recorded.

Figure B3 presents the experiment result with a rated 1.0 mH inductor (Murata 1400 Series) utilizing the above data processing method. The parameters of this inductance ( $L_s, r_{L_s}$ ) is shown in Table 5.2. As can be seen from this figure, the  $\lambda - i$  curve is very close to the linear curve with 1.0582 mH inductance.

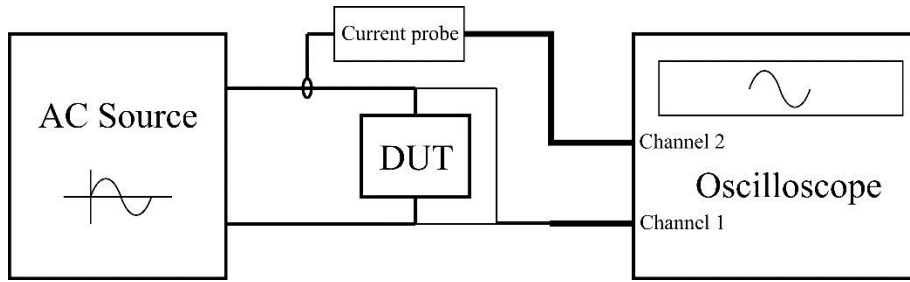
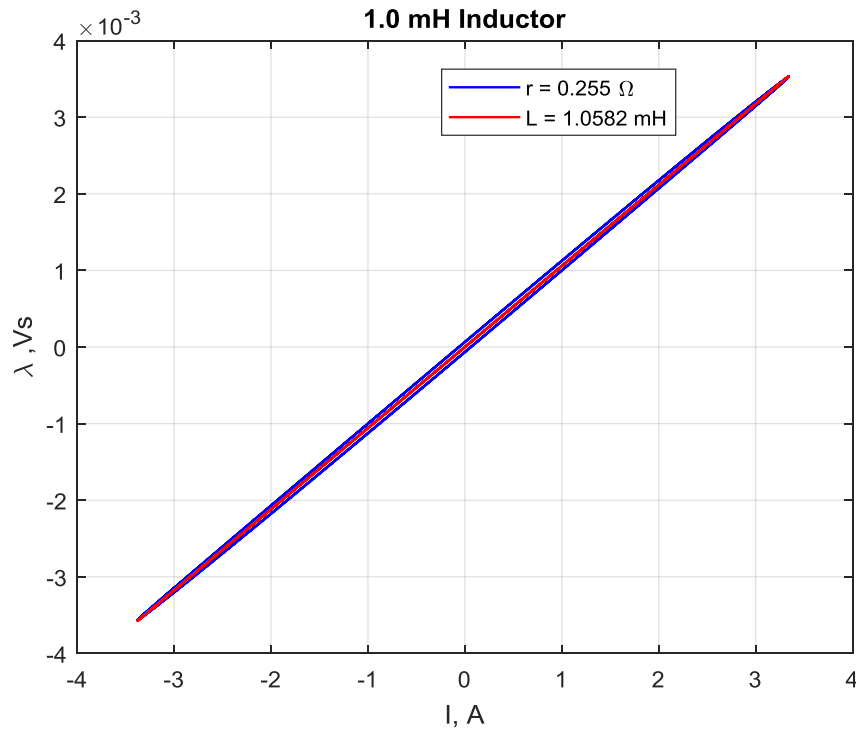


Figure B.2 AC measurement for flux linkage

Figure B.3  $\lambda - i$  curves of 1.0 mH inductor

## B.2 Transformer characterization

The isolation transformer plays an important role to improve system robustness to open-circuit errors. In Chapter 3, six parameters are needed for small-signal analysis: primary winding resistance  $r_p$ , secondary winding resistance  $r_s$ , turns ratio  $TR$ , magnetizing inductance  $L_m$ , primary leakage  $L_{lp}$ , and secondary leakage  $L_{ls}$ . The winding resistances can be easily estimated through DC measurements. To utilize the transformer model described in Chapter 2, it is necessary to incorporate the core saturation in large signal analysis and simulations. Herein, three other

parameters are necessary to represent the saturation: mutual leakage inductance  $L_0$  and nonlinear coefficient  $\alpha$  and  $\beta$ . It is desired to extract all above parameters from data obtained by a limited number of experiments on a given transformer.

As in the case of the inductor characterization, the  $\lambda - i$  curve plays a key role in the transformer characterization. According to the T-equivalent circuit discussed in Chapter 2, the value of turn's ratio is required to refer secondary coil variables to the first. In order to find the turns ratio accurately, the experiment on Figure B4 can be carried out for both the primary and secondary coils. Since the secondary winding can be regarded as open, the voltage measured from Channel 2 is equal to the magnetizing voltage referred to the primary winding.

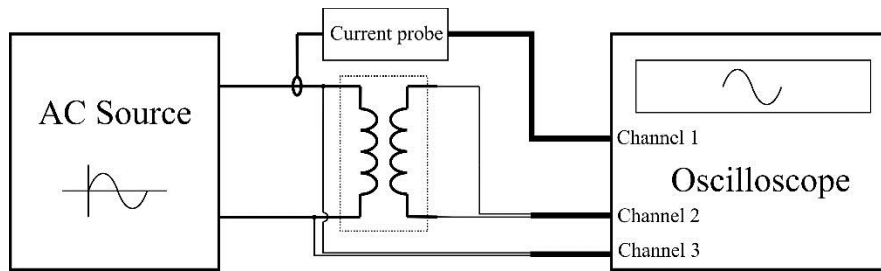


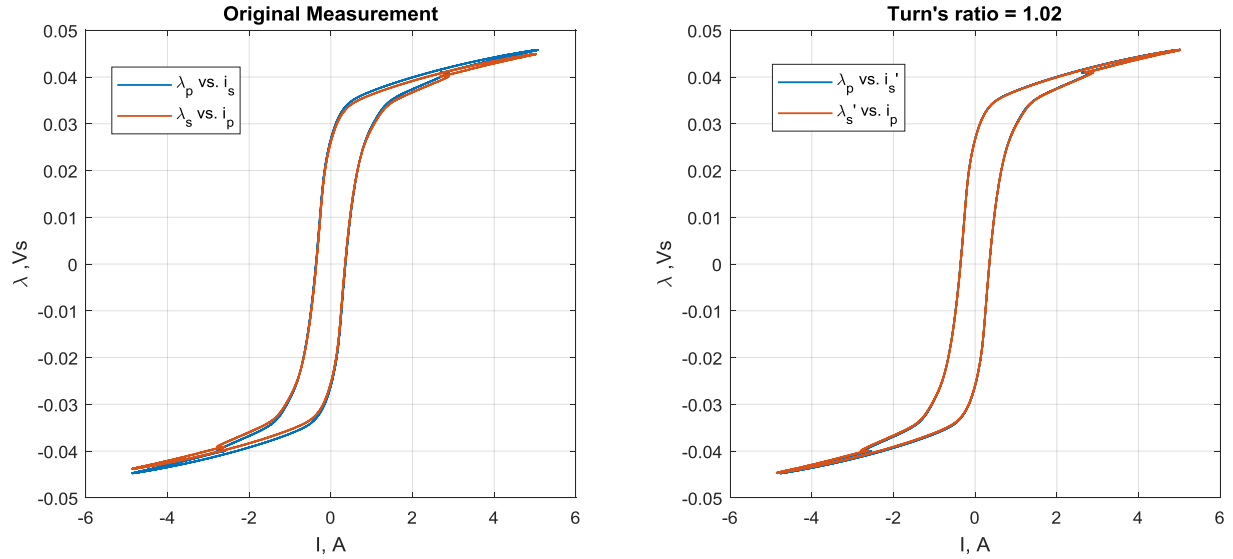
Figure B.4 Transformer characterization

Taking measurement and using (B.2) to calculate flux linkages yield two set of data:  $\lambda_s$  vs.  $i_p$  and  $\lambda_p$  vs.  $i_s$ . By referring  $\lambda_s$  and  $i_s$  to the primary side, i.e.,

$$\lambda_s' = \frac{N_p}{N_s} \lambda_s = TR \cdot \lambda_s \quad (\text{B.3})$$

$$i_s' = \frac{N_s}{N_p} i_s = \frac{1}{TR} i_s \quad (\text{B.4})$$

the two  $\lambda - i$  curves should be identical, if the turn's ratio is correct. Therefore, the turns ratio of a transformer can be found by choosing TR such that the two  $\lambda - i$  curves coincide. Figure B5 depicts an example of a 30/45 W, 60 Hz, 6.6 A (maximum) transformer. The resistances of winding used here are obtained from DC resistance measurement.

Figure B.5  $\lambda - i$  curves of transformer

Since the measured voltage referred to primary winding is equal to magnetizing voltage, and the measured current is the current flowing through the mutual inductor, the  $\lambda - i$  characteristic on the right side of Figure B5 presents an accurate  $\lambda - i$  curve for the mutual inductance. Therefore,  $L_m$ ,  $L_0$ ,  $\alpha$ , and  $\beta$  can be obtained from this figure. From Subsection 2.2.3, the anhysteretic  $\lambda - i$  curve can be expressed as

$$\lambda(i_m) = \alpha \cdot \arctan(\beta i_m) + L_0 i_m \quad (\text{B.5})$$

Moreover, the following relationship can be found:

$$\lim_{i_m \rightarrow \infty} \frac{\partial \lambda(i_m)}{\partial i_m} = L_0 \quad (\text{B.6})$$

$$\left. \frac{\partial \lambda(i_m)}{\partial i_m} \right|_{i_m=0} = L_m = \alpha \beta + L_0 \quad (\text{B.7})$$

From the measured  $\lambda - i$  curve,  $L_m$  and  $L_0$  can be firstly estimated as slopes when  $i_m$  is zero and very large, respectively. After that, the two nonlinear parameters  $\alpha$  and  $\beta$  can be obtained together by curving fitting (B.5) to match the measured  $\lambda - i$  curve, with the relationship  $\alpha \beta = L_m - L_0$ . The curve of (B.5) corresponding to the given transformer as in Figure B5 is shown in Figure B6.

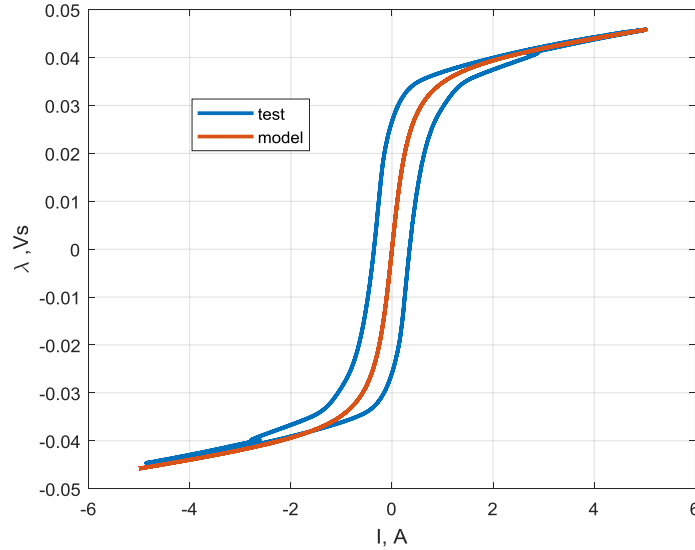


Figure B.6 Transformer  $\lambda - i$  curves modeling

A convenient approach to estimate the linkage inductances is to measure the short-circuit waveforms, as shown in Figure B7. When the secondary winding is shorted, it can be regarded that the excitation current flows through the primary and the referred secondary circuits, since the magnetizing inductance is extremely large compared to the leakage inductances. Therefore, the sum of the two leakage inductances,  $L_{lp}$  and the referred  $L_{ls}$  can be shown as

$$L_{lp} + TR^2 L_{ls} = L \quad (\text{B.8})$$

where  $L$  is the apparent inductance viewed from the primary side, as shown in Figure B8. In (B.8), the turns ratio is already known from the magnetizing inductance characterization. Also, in approximation, the leakage inductances are proportional to the square of turns ratios, with which (B.8) can be solved. The advantage of this method is that the noises in voltage and current waveforms due to a large mutual inductance can be avoided.

The parameters of this transformer ( $r_p$ ,  $r_s$ ,  $TR$ ,  $L_{lp}$ ,  $L_{ls}$ ,  $L_0$ ,  $\alpha$ , and  $\beta$ ) are listed in Table 5.2 and used in Subsection 5.2.

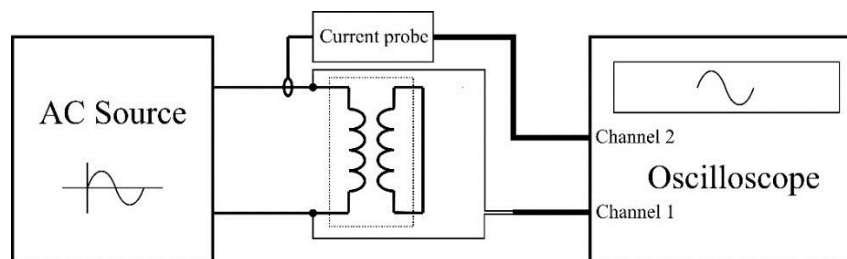


Figure B.7 Leakage inductance measurement

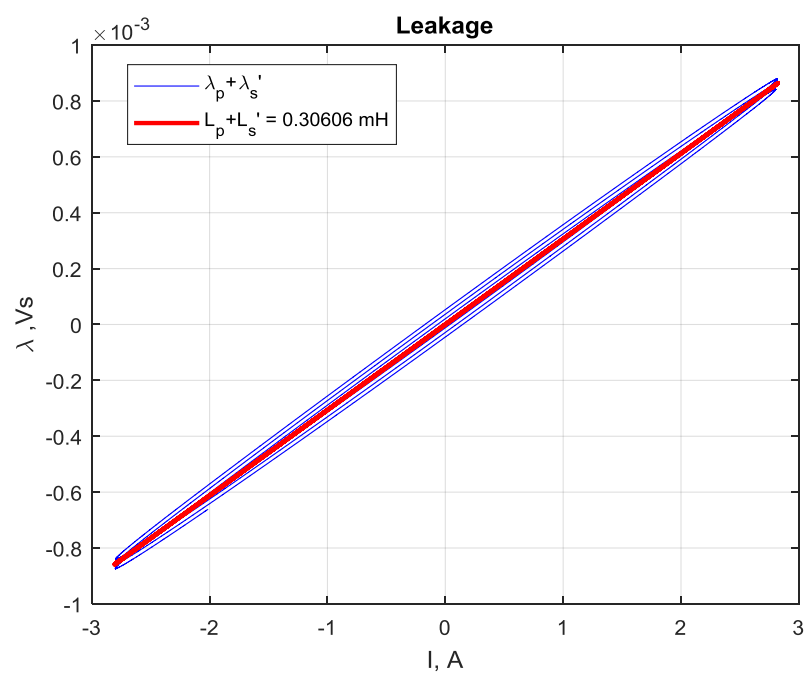


Figure B.8 Leakage characterization

## REFERENCES

- [1] J. D. Bullough, Z. Yuan, and M. S. Rea, "Perceived brightness of incandescent and LED aviation signal lights." *Aviation, space, and environmental medicine*, vol. 78, no. 9, pp 893-900, 2007.
- [2] D. Giardini and J. H. Galloway, "A single phase matrix down-converter for airport lighting regulation." *Industry Applications Conference, Thirty-Fourth IAS Annual Meeting IEEE*, vol. 2, 2005.
- [3] J. Granado, J. Chavez, A. Torralba, and A. C. Oria, "Modeling Airfield Ground Lighting Systems for Narrowband Power-Line Communications." *IEEE Transactions on Power Delivery*, vol. 25, no. 4, pp 2399-2405, 2010.
- [4] ADB Airfield Solutions, *Runway End Identifier Lights programming and Configuration*, 2014.
- [5] S. D. Sudhoff, S.F. Glover, P. T. Lamm, D. H. Schmucker, and D. E. Delisle, "Admittance space stability analysis of power electronic systems." *IEEE Transactions on Aerospace and Electronic Systems*, vol. 36, no. 3, pp. 965-973, 2000.
- [6] V. Grigore, J. Hatonen, J. Kyyra, and T. Suntio, "Dynamics of a buck converter with a constant power load." *Power Electronics Specialists Conference (PESC) 98, 29th Annual IEEE*, vol. 1, pp. 72-78, 1998.
- [7] P. Liutanakul, A. B. Awan, S. Pierfederici, B. Nahid-Mobarakeh, and F. Meibody-Tabar, "Linear stabilization of a DC bus supplying a constant power load: A general design approach." *IEEE Transactions on Power Electronics*, vol. 25, no. 2, pp.475-488, 2010.
- [8] W. Du, J. Zhang, Y. Zhang, and Z. Qian, "Stability criterion for cascaded system with constant power load." *IEEE Transactions on Power Electronics*, vol. 28, no. 4, pp. 1843-1851, 2013.
- [9] I. Kondratiev, E. Santi, R. Dougal, and G. Veselov, "Synergetic control for DC-DC buck converters with constant power load." *Power Electronics Specialists Conference (PESC) 04, IEEE 35th Annual*, vol. 5, pp. 3758-3764, 2004.
- [10] P. Magne, D. Marx, B. Nahid-Mobarakeh, and S. Pierfederici, "Large-signal stabilization of a dc-link supplying a constant power load using a virtual capacitor: Impact on the domain of attraction." *IEEE Transactions on Industry Applications*, vol. 48, no. 3, pp. 878-887, 2012.
- [11] H. Matsuo, W. Lin, F. Kurokawa, T. Shigemizu, and N. Watanabe, "Characteristics of the multiple-input DC-DC converter." *IEEE Transactions on Industrial Electronics*, vol. 51, no. 3, pp. 625-631, 2003.
- [12] O. Dranga, B. Buti, and I. Nagy, "Stability analysis of a feedback-controlled resonant DC-DC converter." *IEEE Transactions on Industrial Electronics*, vol. 50, no. 1, pp. 141-152, 2003.

- [13] W. Chen, X. Ruan, H. Yan, and K. T. Chi, "DC/DC conversion systems consisting of multiple converter modules: stability, control, and experimental verifications." *IEEE Transactions on Power Electronics*, vol. 24, no. 6, pp. 1463-1474, 2009.
- [14] J. Alvarez-Ramirez, I. Cervantes, G. Espinosa-Perez, P. Maya, and A. Morales, "A stable design of PI control for DC-DC converters with an RHS zero." *IEEE Transactions on Circuits and Systems I: Fundamental Theory and Applications*, vol. 48, no. 1, pp. 103-106, 2001.
- [15] P. Mattavelli, L. Rossetto, and G. Spiazzi, "Small-signal analysis of DC-DC converters with sliding mode control." *IEEE transactions on Power Electronics*, vol. 12, no. 1, pp. 96-102, 1997.
- [16] J. Roh, "High-performance error amplifier for fast transient DC-DC converters." *IEEE Transactions on Circuits and Systems II: Express Briefs*, vol. 52, no. 9, pp. 591-595, 2005.
- [17] S. G. Johansson, G. Asplund, E. Jansson, and R. Rudervall, "Power system stability benefits with VSC DC-transmission systems." *CIGRE session*, pp. B4-204. 2004.
- [18] C. W. Taylor, D. C. Erickson, K. E. Martin, R. E. Wilson, and V. Venkatasubramanian, "WACS-wide-area stability and voltage control system: R&D and online demonstration." *Proceedings of the IEEE*, vol. 93, no. 5, pp. 892-906, 2005.
- [19] M. Tabari and A. Yazdani, "Stability of a DC distribution system for power system integration of plug-in hybrid electric vehicles." *IEEE Transactions on Smart Grid*, vol. 5, no. 5, pp. 2564-2573, 2014.
- [20] H. Komurcugil and O. Kukrer, "Lyapunov-based control for three-phase PWM AC/DC voltage-source converters." *IEEE Transactions on Power Electronics*, vol. 13, no. 5, pp. 801-813, 1998.
- [21] E. A. A. Coelho, P. C. Cortizo, and P. F. D. Garcia, "Small-signal stability for parallel-connected inverters in stand-alone AC supply systems." *IEEE Transactions on Industry Applications*, vol. 38, no. 2, pp. 533-542, 2002.
- [22] N. Martins, "Efficient eigenvalue and frequency response methods applied to power system small-signal stability studies." *IEEE Transactions on Power Systems*, vol. 1, no. 1, pp. 217-224, 1986.
- [23] L. Wang and A. Semlyen, "Application of sparse eigenvalue techniques to the small signal stability analysis of large power systems." *Power Industry Computer Application Conference, PICA'89, IEEE*, 1989.
- [24] Y. Yan, D Shi, D Bian, B Huang, Z. Yi, and Z. Wang, "Small-signal Stability Analysis and Performance Evaluation of Microgrids under Distributed Control." *IEEE Transactions on Smart Grid*, in press, 2018.

- [25] H. Jia, X. Yu, Y. Yu, and C. Wang, "Power system small signal stability region with time delay." *International Journal of Electrical Power & Energy Systems*, vol. 30 no. 1, pp. 16-22, 2008.
- [26] A. R. Bergen and D. J. Hill. "A structure preserving model for power system stability analysis." *IEEE Transactions on Power Apparatus and Systems*, vol. 1, pp. 25-35, 1981.
- [27] H. Chiang, F. F. Wu, and P. P. Varaiya, "A BCU method for direct analysis of power system transient stability." *IEEE Transactions on Power Systems*, vol. 9, no. 3, pp. 1194-1208, 1994.
- [28] H. Chiang, F. F. Wu, and P. P. Varaiya, "Foundations of direct methods for power system transient stability analysis." *IEEE Transactions on Circuits and systems*, vol. 34. no. 2, pp. 160-173, 1987.
- [29] N. Tsolas, A. Arapostathis, and P. Varaiya, "A structure preserving energy function for power system transient stability analysis." *IEEE Transactions on Circuits and Systems*, vol. 32, no.10, pp. 1041-1049, 1985.
- [30] P. C. Krause, O. Wasynczuk, S. Sudhoff, and S. Pekarek, *Analysis of electric machinery and drive systems*, John Wiley & Sons, 2013.
- [31] ADB Airfield Solutions, *Instruction Manual of L-861T Elevated Taxiway Edge LED (ETES) Light*.
- [32] F. Wang, "Sine-triangle versus space-vector modulation for three-level PWM voltage-source inverters." *IEEE transactions on industry applications*, vol. 38, no. 2, pp. 500-506, 2002.
- [33] K. Rothenhagen and F. W. Fuchs, "Performance of diagnosis methods for IGBT open circuit faults in voltage source active rectifiers." *Power Electronics Specialists Conference PESC 04. IEEE 35th Annual*. vol. 6. *IEEE*, 2004.
- [34] M. Liserre, A. Dell'Aquila, and F. Blaabjerg, "An overview of three-phase voltage source active rectifiers interfacing the utility." *Power Tech Conference Proceedings*, vol. 3. *IEEE*, 2003.
- [35] P. Zanchetta, D. B. Gerry, V. G. Monopoli, J. C. Clare, and P. W. Wheeler, "Predictive current control for multilevel active rectifiers with reduced switching frequency." *IEEE Transactions on Industrial Electronics*, vol. 55, no. 1, pp. 163-172, 2008.
- [36] A. Siebert, A. Troedson, and S. Ebner, "AC to DC power conversion now and in the future." *IEEE Transactions on Industry Applications*, vol. 38, no. 4, pp. 934-940, 2002.
- [37] J. Huang, K. Corzine, and M. Belkhat, "Single-phase ac impedance modeling for stability of integrated power systems." *Electric Ship Technologies Symposium, IEEE*, 2007.
- [38] C. Sun, G. Wei, and Z. Bi, "Detection for reactive and harmonics currents of unbalanced three-phase systems based on synchronous reference frame transformation." *Proceedings of the Csee*, vol. 12, no. 8, 2003.

- [39] F. Blaabjerg, R. Teodorescu, M. Liserre, and A. V. Timbus, "Overview of control and grid synchronization for distributed power generation systems." *IEEE Transactions on industrial electronics*, vol. 53, no. 5, pp. 1398-1409, 2006.
- [40] P. Rodríguez, J. Pou, J. Bergas, J. I. Candela, R. P. Burgos, and D. Boroyevich, "Decoupled double synchronous reference frame PLL for power converters control." *IEEE Transactions on Power Electronics*, vol. 22, no. 2, 584-592, 2007.
- [41] C. Schauder and H. Mehta, "Vector analysis and control of advanced static VAR compensators." *IET Proceedings C-Generation, Transmission and Distribution*. vol. 140. no. 4. 1993.
- [42] M. Belkhaty, *Stability Criteria for Ac Power Systems with Regulated Loads*, Ph.D. thesis, Department of Electrical Engineering, Purdue University, 1997.
- [43] J. Jatskevich, S. D. Pekarek, and A. Davoudi, "Parametric average-value model of synchronous machine-rectifier systems." *IEEE transactions on energy conversion*, vol. 21, no. 1, pp. 9-18, 2006.
- [44] S. D. Sudhoff and O. Wasynczuk, "Analysis and average-value modeling of line-commutated converter-synchronous machine systems." *IEEE transactions on energy conversion*, vol. 8, no. 1, pp. 92-99, 1993.
- [45] S. D. Sudhoff, "Analysis and average-value modeling of dual line-commutated converter-6-phase synchronous machine systems." *IEEE transactions on energy conversion*, vol. 8, no. 3, pp. 411-417, 1993.
- [46] H. Atighechi, *Dynamic average-value model of high power ac-dc converters and HVDC systems*, Dissertation, University of British Columbia, 2013.
- [47] A. A. Fardoun, E. F. Fuchs, and H. Huang, "Modeling and simulation of an electronically commutated permanent-magnet machine drive system using SPICE." *IEEE transactions on industry applications*, vol. 30, no. 4, 927-937, 1994.
- [48] Q. Han, N. Samoylenko, and J. Jatskevich, "Average-value modeling of brushless DC motors with 120 voltage source inverter." *IEEE Transactions on Energy Conversion*, vol. 23, no. 2, pp. 423-432, 2008.
- [49] J. Jatskevich, S. D. Pekarek, and A. Davoudi, "Parametric average-value model of synchronous machine-rectifier systems." *IEEE Transactions on energy conversion*, vol. 21, no. 1, pp. 9-18, 2006.
- [50] A. Davoudi, J. Jatskevich, and T. D. Rybel, "Numerical state-space average-value modeling of PWM DC-DC converters operating in DCM and CCM." *IEEE Transactions on power electronics*, vol. 21, no. 4, pp. 1003-1012, 2006.
- [51] B. Lehman and R. M. Bass, "Switching frequency dependent averaged models for PWM DC-DC converters." *IEEE Transactions on Power Electronics*, vol. 11, no. 1, pp. 89-98, 1996.

- [52] A. Davoudi, and J. Jatskevich, "Parasitics realization in state-space average-value modeling of PWM dc-dc converters using an equal area method." *IEEE Transactions on Circuits and Systems I: Regular Papers*, vol. 54, no. 9, pp. 1960-1967, 2007.
- [53] V. A. Caliskan, O. C. Verghese, and A. M. Stankovic, "Multifrequency averaging of DC/DC converters." *IEEE Transactions on Power Electronics*, vol. 14, no. 1, pp. 124-133, 1999.
- [54] X. Feng, J. Liu, J. and F. C. Lee, "Impedance specifications for stable DC distributed power systems." *IEEE Transactions on Power Electronics*, vol. 17, no. 2, pp. 157-162, 2002.
- [55] B. Wen, D. Boroyevich, P. Mattavelli, Z. Shen, and R. Burgos, "Experimental verification of the Generalized Nyquist stability criterion for balanced three-phase ac systems in the presence of constant power loads." *Energy Conversion Congress and Exposition (ECCE), IEEE*, pp. 3926-3933, 2012.
- [56] J. Sun, "Impedance-based stability criterion for grid-connected inverters." *IEEE Transactions on Power Electronics*, vol. 26, no. 11 pp. 3075-3078, 2011.
- [57] A. G. J. MacFarlane, *Complex variable methods for linear multivariable feedback systems*. Taylor & Francis, Inc., 1980.
- [58] T. Kailath, *Linear Systems*, Prentice Hall, 1980.
- [59] A. G. J. MacFarlane and I. Postlethwaite, "The generalized Nyquist stability criterion and multivariable root loci." *International Journal of Control*, vol. 25, no. 1, pp. 81-127, 1977.
- [60] J. Huang, K. A. Corzine, and M. Belkhat, "Small-signal impedance measurement of power-electronics-based AC power systems using line-to-line current injection." *IEEE Transactions on Power Electronics*, vol. 24, no. 2, pp. 445-455, 2009.
- [61] J. Huang, K. A. Corzine, and M. Belkhat, "Single-phase ac impedance modeling for stability of integrated power systems." *Electric Ship Technologies Symposium, IEEE*, 2007.

## VITA

Yimajian Yan joined Zhejiang University in 2009 and (SUNY) Stony Brook University in 2010. He received the B.E. degree in 2013. He joined the School of Electrical and Computer Engineering at Purdue University for the direct Ph.D. program in 2013. He will join Google after receiving his doctorate in 2018.